Topology of normal fault damage zones in carbonate rocks, Malta – implications for the development of connectivity in evolving fault networks

Kari Nærland

Master thesis in Petroleum Geoscience

Department of Earth Science

University of Bergen

November 2016

Abstract

Fault damage zones are known to be more complex in linkage zones, relays and at fault tips. From a reservoir perspective, these damage complexities may act as conduits or barriers for fluid flow, hence they need to be understood and quantified. This study quantifies the fracture network properties of three different damage zone types: damage occurring around stage 2 to 4 relay ramps, splay faults and fault tips. Specifically, the connectivity is quantified by the use of topology. Topology uses fracture intersections and endpoints to quantify the relationships between fractures within a fracture network, by the use of nodes and branches. A topological approach is used on 18 damage zones in the study area, Ras ir Raheb, on the west coast of Malta. This area shows excellent outcrops of small-scale (throw < 1m) normal faults formed in carbonate rocks.

Analysis of the topology and geometry of the studied damage zones show that: the connectivity is lower in stage 2 relay damage zones and fault tips compared to stage 3 relay damage zones and splay fault damage zones. The greatest connectivity is documented in stage 4 relay damage zones, which indicates that connectivity develops with maturity. Circular sub-samples, fracture intensity- and connecting node frequency maps are used to analyse spatial variability within the damage zones. Results show that the higher values are localised in areas of bifurcation and linkage. The topological characteristics of studied damage zones may be used as proxies for different stages of fault and damage zone evolution, with fault tips representing an early stage, and hard-linked relays and splays representing further progressed stages of growth and linkage. Using this as a basis, a model for the development of connectivity in evolving extensional fault networks is presented: 1) fault initiation stage; multiple isolated faults are active, resulting in numerous fault tip damage zones. The fault network is immature at this stage, hence a low connectivity. 2) Interaction and linkage stage; faults start to interact and link, ergo the fault network becomes more connected and show a medium connectivity. 3) Through-going fault zones; deformation continues and becomes localised along a few through-going faults, consequently the fault network shows the highest degree of connectivity. The use of topology increases our understanding of network properties of damage zones and allow us to explore the evolution of connectivity, both spatially and temporally in damage zones and other fracture networks.

Acknowledgments

First and foremost, I want to express my deepest gratitude to my supervisor Prof. Atle Rotevatn and my co-supervisor Casey Nixon for your guidance, inspiration and great discussions throughout this thesis. Thanks for your patience and knowledge sharing both in Malta and at the University of Bergen. Atle is specially thanked for valuable inputs and for giving me the opportunity to present my data at the TSG conference in London. Casey Nixon is thanked for being a topology expert and for your support both in ArcGIS and Excel. I want to thank Thomas Berg Kristensen for support in Adobe Illustrator CC and for help during preparations for TSG. I also thank Atle Rotevatn, David Peacock, Casey Nixon and fellow students Stine, Marte and Maria for comments and proofreading different chapters of this thesis.

The department of Earth Science at the University of Bergen and BKK is thanked for funding my fieldwork.

I owe a special thank to Atle Rotevatn, Thomas Berg Kristensen, Casey Nixon, David Peacock, Ulrike Freitag, Arild Andresen and fellow student Vilde Dimmen for their assistance, inspirational discussions and a lot of fun during the two field seasons in Malta. Additionally, I owe my gratitude to Anna and Charles at the Maple Farm Bed and Breakfast for your kindness, hospitality and for fun nights both at restaurants with your family and at the vineyard during our stay.

I also thank fellow geology students for all the unforgettable memories we sheared at field trips, at the university and other social gatherings during last five years. Especially, I thank the incredible people at "midtrommet" for many laughs and support. Additionally, I thank fellow student and roomie Karina for always staying positive both at the university and at home. At last, I want to thank my incredible family for their encouragement, motivation and for always believing in me.

Kari Nærland

Kari Nærland

Bergen, 19th of November 2016

Table of content

1 Introduction 1
1.1 Rationale 1
1.2 Aims and objectives 2
1.3 Study area 2
2 Theoretical background 4
2.1 Fractures 4
2.1.1 Fracture types 5
2.2 Fault zones 6
2.2.1 Architecture and geometry of fault zones 7
2.3 Fault damage zones 11
2.3.1 Fault tip damage zones 11
2.3.2 Relay damage zones 12
2.3.3 Splay fault damage zones 14
2.4 Fracture networks 15
2.4.1 Fracture geometry and properties 15
2.4.2 Network properties 16
2.4.3 Topology 17
3 Geological setting 19
3.1 Regional tectonic setting 19
3.1.1 Tectonic evolution of the Central Mediterranean 19
3.1.2 The Pelagian Platform 20
3.1.3 The Pantelleria Rift system 21
3.1.4 The Maltese Graben system 22
3.2 Regional stratigraphic framework 24
3.2.1 Pre-rift phase 25
3.2.2 Early syn-rift phase 26
3.2.3 Late syn-rift phase 28
3.2.4 Post-rift phase 29
4 Methods 30
4.1 Topology 30
4.1.1 Connectivity 31
4.1.2 Euler's theorem – number of faces 33
4.1.3 Fracture intersection abundances 34
4.2 Field methods 34
4.2.1 Fault damage zone description 34
4.2.2 Topology of fault damage zones 35
4.3 Data processing 35
4.3.1 Topology in ArcGIS 35
4.3.2 Density maps in ArcGIS 36
4.3.3 Circle samples in ArcGIS 36

4.3.4 Statistical analysis 37
4.4 Sources of error 38
4.4.1 Sources of errors in the field 38
4.4.2 Sources of errors during data processing 38
5 Results 40
5.1 Structures and stratigraphy of the field area 40
5.1.1 Structural framework of the study area 40
5.1.2 Stratigraphy of the study area 42
5.2 Geometry and topology of the studied damage zones 45
5.2.1 Fracture intensities 46
5.2.2 Connecting node frequencies 47
5.3 Geometry and topology of fault tip damage zones 47
5.4 Geometry and topology of splay fault damage zones 51
5.5 Geometry and topology of relay damage zones 54
5.6 Spatial variability within damage zones 58
5.6.1 Fault tip damage zone variability – K5 58
5.6.2 Relay damage zone variability – K7 61
5.6.3 Splay fault damage zone variability – K3 64
6 Discussion 68
6.1 Topological similarities and differences between fault damage zone types 68
6.2 Spatial variability within fault damage zones 70
6.3 Evolution of the topology of fracture networks during fault growth 70
6.3.1 Topology of fracture networks during development of a fault tip 71
6.3.2 Topology of fracture networks during development of a splay zone 72
6.3.3 Topology of facture networks during the development of a relay zone 73
6.4 Evolution of fault networks and their topology 75
6.5 Implications and limitations 79
6.5.1 Structural controls and fluid flow in fault and fracture networks 79
6.5.2 Limitations using topology on seismic resolution datasets 81
6.5.3 Implications for topology and connectivity 81
7 Conclusions and further work 83
7.1 Conclusions 83
7.2 Further work 84
8 References 86
Appendix I – Workflow in ArcGIS 10.3.1 and Excel 95
Appendix II – Localities and maps 101

1 Introduction

This study is one of two MSc projects that examine structures in carbonate rocks along the west coast of Malta. This thesis focuses on detailed analysis of small-scale normal faults and their damage zones. More specifically, the study quantifies fracture connectivity within different types of complex damage zones, i.e. damage at fault tips, fault splays and relay zones. This is done by the use of topology (sensu Sanderson and Nixon, 2015).

1.1 Rationale

A great deal of literature focusing on fault damage zones has been published (e.g. Hull, 1988; Evans, 1990; Caine et al., 1996; Childs et al., 1997; Kim et al., 2004; Berg and Skar, 2005; Fossen et al., 2005; Childs et al., 2009; Gudmundsson et al., 2010; Choi et al., 2016) and there is a general agreement that fault damage zones are more complex at fault tips, in linkage zones, relays and bends (e.g. Petit and Barquins, 1988; Childs et al., 1996; Cowie and Shipton, 1998; Ferrill et al., 2000; Fossen et al., 2005; Rotevatn et al., 2007; Bastesen et al., 2009; Dockrill and Shipton, 2010; Ogata et al., 2014). There is, however, a lack of literature describing and quantifying the connectivity of fractures in such structurally complex settings. In the light of this, this study quantifies fracture network properties of damage zones in and around fault tips, splay faults and relay zones, based on outcrop examples of small-scale faults hosted in carbonate rocks. The study is an attempt to understand connectivity and its evolution in fault damage zones.

Topology (sensu Sanderson and Nixon, 2015) is the main method applied and it is based on considering elements of a fault and fracture network in terms of nodes and branches, to gain information about how the fractures within the network relate to each other. Topology is therefore a useful approach to quantify the connectivity of fracture networks (e.g. Manzocchi, 2002; Sanderson and Nixon, 2015). In contrast to topology, the most conventional methods describe the geometric features of single fractures, using parameters as orientation, curvature, length and spacing etc. (e.g. Priest and Hudson,

1976; Ladeira and Price, 1981; Huang and Angelier, 1989; Rives et al., 1992; Wu and Pollard, 1995). These parameters, however, do not give you any direct information about the geometrical relationship between and the arrangement of fractures within the network, or the network connectivity. Understanding the connectivity of faults and their damage is important within the petroleum industry as faults and damage zones may act as traps, as migration conduits or seals for hydrocarbons and other fluids (e.g. Caine et al., 1996; Childs et al., 1997; Aydin, 2000; Bastesen et al., 2009). Especially in low permeability rocks, such as carbonate rocks (used in this study), the permeability is often induced by fractures and their connectivity (e.g. Faulkner et al., 2010). Hence, the aim is to increase our understanding of the connectivity in damage zones. The connectivity is quantified and studied damage zones are used as proxies for evolutionary stages of fault network and damage growth.

1.2 Aims and objectives

The aim of this study is to increase the understanding of the characteristics and development of fracture network connectivity within damage zones of extensional faults. To do this, the geometry and topology are characterised and quantified in fault damage zones of small-scale normal faults, formed in carbonate rocks in western Malta (Fig. 1.1), including: fault tips, splay faults and relay zones. These specific objectives are used to achieve the aims stated above: i) determine the network properties (topology and connectivity) of outcrop examples of small-scale normal faults and their damage zones; ii) quantify variations in connectivity of damage zones and use density maps to record spatial variations in fracture intensity and connecting node frequency; iii) explain differences and similarities in topology and connectivity of the various damage zones; vi) extrapolate the results to discuss the evolution of fault damage zone connectivity during the evolution of normal fault populations.

1.3 Study area

The study area is located along the west coast of Malta (Fig. 1.1). The exposed stratigraphy is dominated by Oligocene to Pleistocene shallow marine carbonates (Felix, 1973; Pedley et al., 1976; Dart et al., 1993). The biomicritic Miocene Globigerina Limestone Formation

form excellent outcrops for detailed studies of damage zones of small-scale normal faults. The Maltese Islands (Malta, Comino and Gozo) are one of the few emerged areas of the Pelagian Platform, located on the NNE flank of the 600 km long Pantelleria Rift (e.g. Reuther and Eisbacher, 1985; Bonson et al., 2007). The Maltese Graben System is a small part of the Pantelleria rift and it is comprised of two main horsts and grabens (Dart et al., 1993). Normal faults generally strike ENE-WSW onshore in the Maltese Graben System, with the exception of the Maghlaq Fault that strikes ESE-WNW, similar to the Pantelleria Rift trend (Pedley et al., 1976; Illies, 1980; Reuther and Eisbacher, 1985; Bonson et al., 2007). The WSW-striking Victoria Lines Fault is a main fault of the Maltese Graben System and separates the Malta Horst from the North Malta Graben. Ras ir Raheb, the study area (Fig. 1.1), is located at the footwall of the Victoria Lines Fault on the Malta Horst (Dart et al., 1993). Full details of the structural- and stratigraphic development of the study area are presented in Section 3.

Figure 1.1: Google Earth image showing the location of the study area, located on the west coast of Malta Island, which is situated in the Mediterranean Sea between Sicily and Tunisia.

2 Theoretical background

The purpose of this chapter is to introduce the general theoretical background of structural discontinuities, i.e. fractures (Section 2.1). Fault zones (Section 2.2) and types of fault damage zones (Section 2.3) used in this study are presented. Additionally, previous work on fracture networks and topology is introduced (Section 2.4).

2.1 Fractures

Fractures are planar to sub-planar brittle discontinuities affecting the upper crust (e.g. Cowie and Scholz, 1992a; Aydin, 2000). The term fracture does not revile the mode of fracturing and are synonymous with discontinuities (see definition in Peacock et al., 2016). These discontinues are zones that usually are narrower than they are long, frequently described as a surface or a plane. Over the surface there is often displacement and changes in mechanical properties (e.g. Chester and Logan, 1986; Kim et al., 2004; Childs et al., 2009). Fractures form as a result of stresses or fluid pressures exceeding the strength of the host rock (e.g. Anderson, 1951; Fossen, 2010, p.126) and typically forms perpendicular to the direction of greatest principal stress (e.g. Marciniak and Kuczyński, 1967). More specific they can form by; (1) thermoelastic contraction near the earth surface due to uplift and erosion; (2) tectonic stress; (3) fluid overpressure at depth forming hydraulic joints, or; (4) a combination (e.g. Laubach, 1988; Aydin, 2000).

Fractures have various characteristics, and are therefore commonly subdivided in to smaller groups (Section 2.1.1). Understanding fractures is important in such disciplines as engineering geology, civil and mining engineering, geothermal research, volcanology, seismology, hydrology and especially petroleum geology (e.g. Dershowitz and Einstein, 1988; Gudmundsson et al., 2010). Fractures may increase the permeability of the host rock and as a consequence act as a fluid conduit, or decrease the permeability, acting as a baffle (retard the fluid flow) or a barrier (stop the fluid flow), and are therefore important for subsurface fluid flow (e.g. Caine et al., 1996; Sibson, 1996; Aydin, 2000; Ortega and Marrett, 2000; Faulkner et al., 2010; Davidson et al., 2016; Fossen and Rotevatn, 2016). As fractures will affect the production rates of hydrocarbons, researchers have tried to describe them geometrically, mechanically and also to illustrate and quantify the patterns

they form (e.g. Dershowitz and Einstein, 1988; Childs et al., 2009). It has become more important to include predicted fracture patterns in exploration, development and drilling due to the control the distribution and connectivity of fractures will have on the sweep of a producing reservoir (e.g. Laubach, 1992; Scholz and Anders, 1994). To understand fracture networks, outcrops are applied as analogues where geologists can better understand the fracture distribution, spacing, density, connectivity, length and fracture bonded layers better than from cores, plugs and logs (e.g. Laubach, 1992).

2.1.1 Fracture types

Fractures can be divided in to three main groups; (1) extension fractures, which include joints, fissures and veins; (2) contraction or compaction fractures, including compaction bands, stylolites and solution seams and; (3) shear fractures, which include deformation bands and faults or; (4) a combination of two or more of three main groups (Fig. 2.1) (e.g. Aydin, 2000; Peacock et al., 2016). Extension fractures display extension normal to the fracture wall. Joints show no shear displacements, but are often extensional in character, although they may be subsequently sheared. Extensional fractures filled with gas or fluids are often called fissures, and are they infilled by minerals they are called veins (e.g. Engelder, 1987; Peacock et al., 2016). Contraction or compaction fractures are characterised by walls that have moved towards each other, and are often called compaction bands, stylolites or solution seams. Stylolites are irregular surfaces affected by pressure solution (Fig. 2.1) (e.g. Aydin, 2000; Fossen, 2010, p.122). Shear fractures have displacements parallel to the fracture wall. Shear fractures are often used for small displacements (mm-dm) and faults are used for greater displacement (Fossen, 2010, p.121). Due to this unclear scaling limit, shear fractures are referred to as faults in this thesis. Deformation bands are characterised by a narrow tabular zone of strain formed in porous granular rocks, they show various types of grain reorganisation and small shear offsets (e.g. Aydin and Johnson, 1978; Aydin et al., 2006; Fossen et al., 2007).

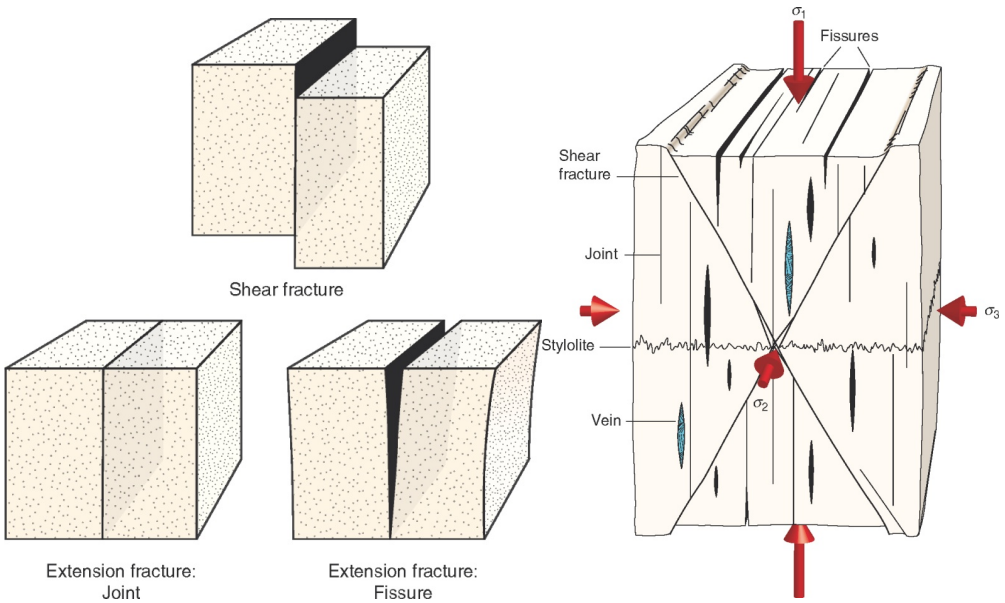

Figure 2.1: Examples of types of fractures formed and their relation to the maximum stress direction (σ_1), illustrated by Fossen (2010, p.121-122).

2.2 Fault zones

A fault zone is comprised of a *fault core*, a *damage zone* and sometimes an extended damage zone or *drag zone* (e.g. Caine et al., 1996; Fossen and Hesthammer, 1998). The *fault core* is where most of the displacement usually is accommodated (>95%) and is associated with one or more slip surfaces and fault rocks. The surrounding *damage zone* typically accommodates less displacement (<5%), which is distributed over a number of discrete structures (e.g. joints, veins, deformation bands, minor faults) and is mechanically related to formation and growth of faults (Sibson, 1977; Cowie and Scholz, 1992c; Antonellini and Aydin, 1994; Scholz and Anders, 1994; Caine et al., 1996; Kim et al., 2004; Childs et al., 2009). The intensity of these structures typically decrease with increasing distance from the fault core (e.g. Chester and Logan, 1986; Antonellini and Aydin, 1994; Scholz and Anders, 1994; Goddard and Evans, 1995; Beach et al., 1999; Gudmundsson et al., 2010). The boundary of the damage zone is therefore located where the intensity is reduced to a background or a minimum value (Beach et al., 1999; Cello et al., 2001; Gudmundsson et al., 2010; Choi et al., 2016). The *drag zone* includes effects of fault growth, like drag (bending layers along the fault, due to brittle-ductile deformation) or rollover of the stratigraphy (Fossen and Hesthammer, 1998), and will not be further discussed as it is generally not considered to be a part of the (brittle) damage zone (Childs et al., 2009).

There is a general positive correlation between fault displacement and damage zone thickness (Evans, 1990; Childs et al., 1997; Beach et al., 1999; Fossen and Hesthammer, 2000; Faulkner et al., 2010), but the plots are often very scattered (e.g. Choi et al., 2016). Several authors explain the scatter with such parameters as lithology, rheology, deformation mechanism, diagenesis, depth of faulting and tectonic environment (e.g. Evans, 1990; Childs et al., 1997; Fossen and Hesthammer, 2000). Asymmetry between damage zone thickness in the hangingwall and footwall may also play a role in the scatter (e.g. Berg and Skar, 2005). Some plots (e.g. Mitchell and Faulkner, 2009; Faulkner et al., 2010) also show that with higher (>200 m) displacements, the thickness of the damage zone has a lower growth rate compared to faults with lower displacements. This is often explained by limited access to outcrops at larger scales or localization of strain at slip surfaces, without continued growth of the damage zone (e.g. Mitchell and Faulkner, 2009; Faulkner et al., 2010). Choi et al. (2016) and Faulkner et al. (2010) suggest that the scatter is caused by diverse ways of defining the thickness of the damage zone, and consequently a summary of data from different researchers will be highly scattered. For this reason, Choi et al. (2016) suggest the use of cumulative fracture frequency, where a change in the gradient of the graph should define the thickness of the damage zone.

2.2.1 Architecture and geometry of fault zones

Fault zones show internal structures and heterogeneous strain distribution over a range of scales and growth stages. Due to differences between different faults, it is not possible that one classification model can be related to all types of fault zones, so conceptual models are established (e.g. Caine et al., 1996; Faulkner et al., 2003; Kim et al., 2004; Childs et al., 2009; Michie et al., 2014). The structural style of the fault core and damage zone, and its various grain sizes and permeabilities, controls if the fault zone will act as a fluid conduit, barrier or a combined conduit-barrier system (Randolph and Johnson, 1989; Smith et al., 1990; Caine et al., 1996).

Permeability structure

Based on faults in outcrops, Caine et al. (1996) present a model of four end-members based on their permeability structure (Fig. 2.2). This classification is based on the relationships between the total fault zone width, the damage zone width and the fault core

width. Based on such controlling factors as internal structure, composition and thickness variations, Caine et al. (1996) present a method to predict whether the fault zone is a conduit, barrier or a combined conduit-barrier system (Fig. 2.2). The permeability structure of a fault zone can be related to the structural regime and stage of fault growth. Discrete structures in the damage zone could give a fault zone a higher permeability and porosity than both the fault core and the host rock (Goddard and Evans, 1995; Caine et al., 1996; Gudmundsson et al., 2010), and the thickness relation of damage zone and fault core is an important effect on the permeability structure of the fault zone (Caine et al., 1996). At late stages in the growth history of a fault zone, grain size reduction and mineral precipitation may cause the fault core to have lower porosity and permeability relative to the host rock (Chester and Logan, 1987; Antonellini and Aydin, 1994; Goddard and Evans, 1995; Caine et al., 1996). A fault core may therefore have acted as a conduit during the early growth stages and as a barrier at a later stage (Caine et al., 1996).

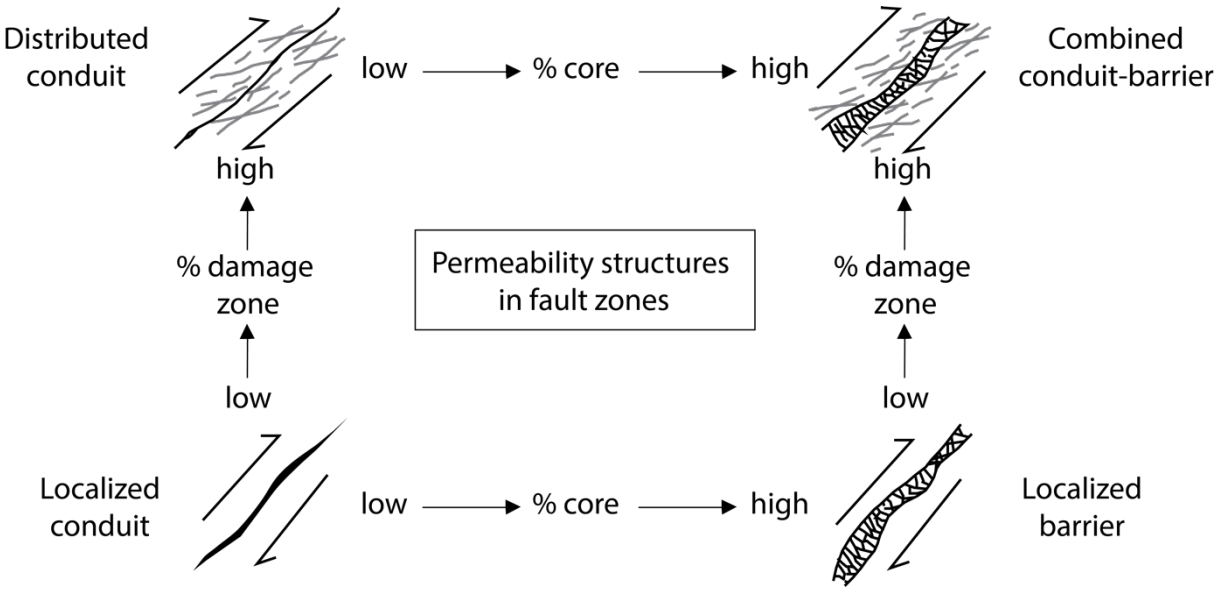

Figure 2.2: Conceptual model for permeability structure of fault zones, based on proportions of damage zone and fault core. Figure modified from Caine et al. (1996).

Fault geometry

Kim et al. (2004) propose a general field-based classification for damage zones, which is based on the geometry of strike-slip faults, but is also designed to be applied to both normal- and reverse faults. The model takes into account where the damage zone is placed in respect to the overall fault geometry. Kim et al. (2004) defines three end-members: (1) fault tip damage zones; (2) wall damage zones and; (3) linking damage zones. All of these

damage zone types may also be classified as along-fault damage zones (sensu Choi et al., 2016). Fault tip damage zones develop due to the stress increase at the tip of the fault relative to the centre of the fault (Cowie and Scholz, 1992c) (Section 2.3.1, Fig 2.3). Linking damage zones develops as a response to interaction and linkage between segments (Kim et al., 2004). Wall damage zones can be caused by abandoned fault tip damage zones as the fault growth and/or by wall damage in response to slip build-up along the fault (Kim et al., 2004). Wall damage zones will not be further discussed in this thesis, as they have not been studied in the field. Linking damage zones, on the other hand, will be subdivided in to splay damage zones (Section 2.3.3) and relay damage zones (Section 2.3.2) (Fig. 2.3). The splay fault damage zones will be a cross-fault damage zone (sensu Choi et al., 2016), as they are studied in cross section (Fig. 2.3). Linking damage zones (Kim et al., 2004) may work in some cases, but it is a very broad classification as linking damage zones may be cross-cutting faults, mutual interactions, single tip interactions or double tip interactions (sensu Fossen et al., 2005).

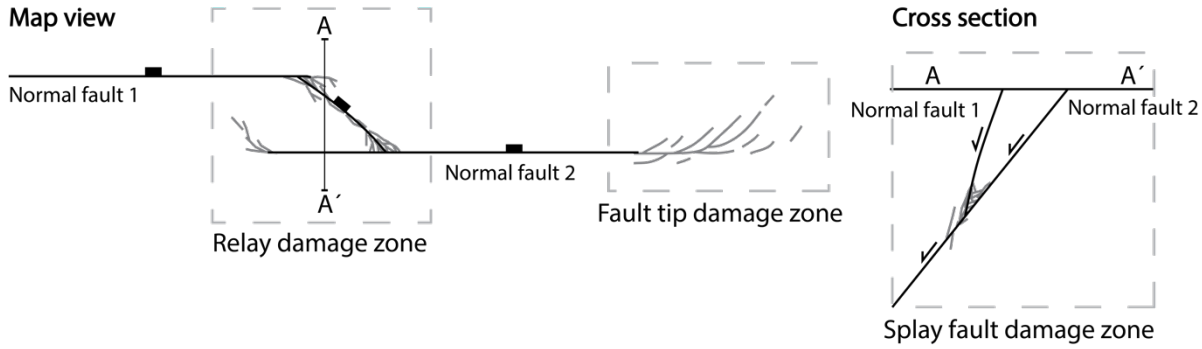

Figure 2.3: Illustration of types of damage zone according to where they are place regarding to the overall geometry of the fault(s). These terms are used for normal fault damage zones for this study. The relay damage zone and the splay fault damage zone correspond to linking damage zones (sensu Kim et al., 2004) or single-tip interaction (sensu Fossen et al., 2005). Relay damage zones forms when two sub-parallel normal faults overlap and interact in map view (Peacock and Sanderson, 1991, 1994), a fault tip damage zones forms at the end/tip of a normal fault and a splay fault damage zone comprise of a master fault and a synthetic splay fault, forming a cone-shaped geometry in cross section. Splay fault damage zones in cross section might be linked to a relay damage zone in map view. More info on the three damage zone types is presented in section 2.3.

Architectural models of fault zones

The traditional classification scheme for fault zones (section 2.2) corresponds well with fault zones formed in siliciclastic rocks, but is often more complicated in carbonate rocks.

For example, Childs et al. (2009) show that the ratio between displacement and fault core thickness is higher for limestones than siliciclastic rocks. This simple model does illustrate the distributed fault core comprising for several slip surfaces that interact, splay, anastomose etc., that typically occur in carbonate rocks (Childs et al., 1997; Faulkner et al., 2003; Childs et al., 2009; Mitchell and Faulkner, 2009; Faulkner et al., 2010; Michie et al., 2014). Michie et al. (2014) study faults in the same field area as described in this thesis, and show that the fault cores are more distributed over several slip surfaces rather than forming a continuous fault core surrounded by a damage zone, more typical for faults in siliciclastic rocks. Michie et al. (2014) suggest a model for fault zones with displacement over 1 m in fine grained carbonate. The model involve a fracture splay zone (FSZ) as the main zone of deformation, where most of the displacement is accommodated through several slip surfaces (and therefore several fault cores), and a weakly deformed damage zone (WDDZ) enclosing the FSZ (Fig. 2.4) (Michie et al., 2014). Both models from Faulkner et al. (2003) and Michie et al. (2014) could be included in the more general cross-fault damage zone type (sensu Choi et al., 2016).

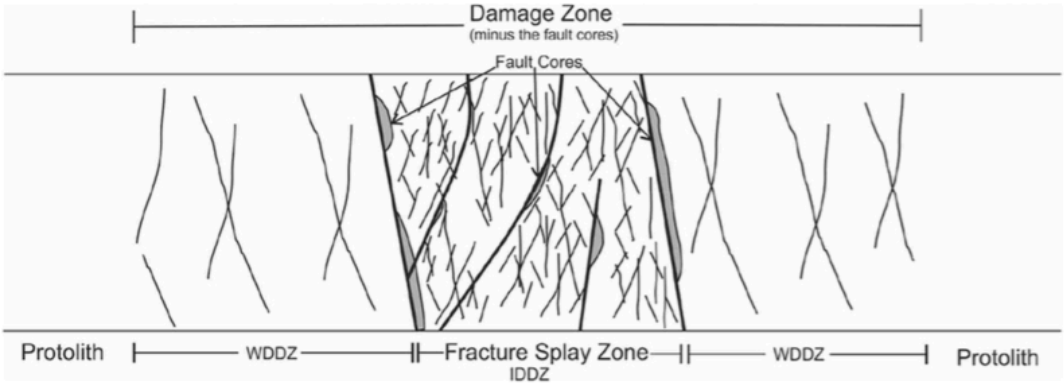

Figure 2.4: Classification scheme for fine-grained carbonates. Fracture Splay Zone (FSZ) includes several slip surfaces and fault cores, enclosed by a Weakly Deformed Damage Zone (WDDZ). Figure from Michie et al. (2014).

Childs et al. (2009) suggest that fault zone complexities and fault core/fault rock thickness are more strongly controlled fault segmentation and geometry during fault growth, than by the rheology of the host rock, although the mechanical stratigraphy commonly controls fault geometry. Mechanical controls on faults are also stressed by Michie et al. (2014), who argue that the FSZ forms due the strength contrast of mechanical layers. The variability of fault geometries due to steps, bends and relay zones etc., during fault

propagation complicates the end-result of a fault core, fault rock and damage zone terminology, illustrated by Childs et al. (2009). The Childs et al. (2009) definition of a damage zone, fault zone and fault core is used here for normal faults investigated in the field area (Fig. 2.5).

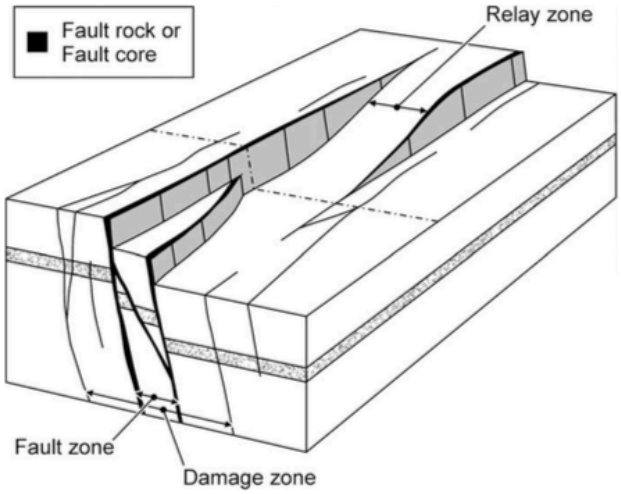

Figure 2.5: Definitions for fault rock/fault core and damage zone used in this thesis, figure and definition from Childs et al. (2009).

2.3 Fault damage zones

Three types of complex damage zones are studied in this thesis; fault tip damage zones (Section 2.3.1), relay damage zones (Section 2.3.2) and splay fault damage zones (Section 2.3.3) are therefore introduced here (Fig 2.3).

2.3.1 Fault tip damage zones

A fault tip process zone is a zone of increased fracturing due to higher stress concentration at the tip of a growing fault (e.g. Petit and Barquins, 1988; Cowie and Scholz, 1992c; Scholz and Anders, 1994; Vermilye and Scholz, 1998). Scholz and Anders (1994) suggest that the width of the process zone is proportional to fault length. A fault tip process zone (e.g. Vermilye and Scholz, 1998) typically forms a fault tip damage zone. Fault tip damage zones are commonly wedge shaped and are dominated by mode II, mode III or mixed mode deformation (Kim et al., 2004). Mode II are shear fractures where movement is into or out of the studied plane, mode III are shear fractures where movement are parallel to the studied plane (e.g. Fossen, 2010, p.439). Mode II tip damage zones are usually

asymmetrical and are typically characterised by wing cracks, horsetail fractures, antithetic faults and synthetic faults. Mode III tip damage zones are more symmetrical and commonly include synthetic and antithetic faults (Kim et al., 2004). Fractures within the fault tip damage zone may act as both lateral and vertical conduits, or as barriers, to fluid flow (e.g. Scholz and Anders, 1994). Fault tips acting as conduits are shown by Ogata et al. (2014), who observed bleaching patterns in fault tip damage zones, indicating paleo-fluid flow. The bleaching is usually concentrated along through-going fractures i.e. that cut through various lithologies and are not bed confined.

2.3.2 Relay damage zones

A relay zone or structure are defined by Peacock et al. (2016) as *a zone of geometric or kinematic linkage between sub-parallel fault segments,* and are most commonly described in extensional settings (e.g. Peacock and Sanderson, 1994; Fossen and Rotevatn, 2016). A relay ramp typically form between the two sub-parallel normal fault segments that step in map view, where the segments interact and transfer strain forming an inclined zone between them. The geometry of the relay ramp is determined by displacement gradients of the segments, where the linkage point is marked by a minimum in displacement (Peacock and Sanderson, 1991, 1994). Larsen (1988) was the first to give a simple overview of the geometry and the transfer of offset in relay zones through relay ramps between listric normal faults. It is now recognised that faults do not have to be listric or connected to create a relay zone (Peacock and Sanderson, 1991).

Peacock and Sanderson (1991, 1994) suggest a four stage development of relay zones; stage 1: fault segments are neither overlapping nor interacting. Stage 2: the segments are overlapping and starting to interact with no physical linkage between the segments, although strain is distributed by bending of the layers in the relay ramp. Stage 3: the fault segments are overlapping and interacting, a linking fault/fracture is formed between the two main segments. Stage 4: the two segments are connected by one or two main faults and the previous fault tips are now minor faults, creating a displacement minimum in the linkage zone. Stage 1 and 2 are often referred to as an intact relay or soft linkage and stage 3 and 4 as a breached relay or hard linkage (e.g. Walsh and Watterson, 1991; Childs et al., 2009). These four stages and their resulting damage are studied here, and are referred to as stage 2 relay damage zones, stage 3 relay damage zone and stage 4 relay damage zones.

Huggins et al. (1995) and Childs et al. (1995) suggest that relay zones may develop from two individual faults approaching each other or by one bifurcating fault. Both scenarios may lead to breaching during continued growth. It is necessary to consider scale when considering soft or hard linkage, as an apparent soft linked structure may be hard linked when observed in more detail (Walsh and Watterson, 1991). Larsen (1988) argues that relay structures only form in extensional settings at low strains, but relays will continue to develop in stage 3 and 4 and thereafter be left as a lens at the fault plane as the through-going fault continues to develop (Peacock and Sanderson, 1991).

Hard linked relay ramps may be considered as linking damage zones (Kim et al., 2004) or single- or double tip interaction damage zones (Fossen et al., 2005). Linking damage zones display a higher degree of complexity than a single fault damage zone both in siliciclastic and carbonate rocks (Martel, 1990; Kim et al., 2004; Fossen et al., 2005; Rotevatn et al., 2007; Bastesen and Rotevatn, 2012). Fracture networks documented for breached relays include increased fracture intensity (number of fractures/m) and diverse fracture orientations (e.g. Bastesen and Rotevatn, 2012). Therefore, it is expected that the complexity of fracture patterns increase as segments grow, interact and link (e.g. Bastesen and Rotevatn, 2012). A common assumption is that joints form nearly parallel to a main normal fault. Calculated stress fields around normal faults, however, show that joints may form at high angles to the fault, especially in relay zones (Kattenhorn et al., 2000). The reason for oblique joints relative to the main fault may be rotation of the maximum principal stress (<30º) within the relay zone. Perpendicular joints on the other hand (up to 75º), are related to the remote stress around the two main faults, which are linked to the ratio of fault-parallel to fault-perpendicular stress (Kattenhorn et al., 2000). During an increase of this ratio, joins growing away from the main fault, forms progressively higher angles to the fault (Kattenhorn et al., 2000). A relay structure will therefore cause a wider damage zone thickness at the linkage area, relative to the damage zone thickness away from the linkage area (e.g. Kim et al., 2004; Fossen et al., 2005). In fault linkage zones it is expected that fracture orientations are more complex and the damage zone is wider, relative to a simple fault where the damage zone in thinner and discrete structures are more parallel to the main fault (e.g. Peacock and Sanderson, 1994; Fossen et al., 2005; Bastesen and Rotevatn, 2012).

Relay ramps are often considered as conduits for subsurface fluid flow, e.g. Bastesen and Rotevatn (2012) showed that breached relay zones in carbonate rock provide both the vertical and the lateral conduits, in addition an increased connectivity across and along faults. Sub seismic structures and factors like facies, composition, structural style, deformation mechanism and burial depth should therefore be accounted when dealing with relay structures subsurface (e.g. Rotevatn et al., 2007).

2.3.3 Splay fault damage zones

A splay fault is a geometrical feature, which describes one (or more) fault that connects with a larger fault that it is related to (sensu Peacock et al., 2016). Splay faults (Anderson, 1951) splay off a main fault at an acute angle to the main fault (e.g. McGrath and Davison, 1995; Perrin et al., 2016), and are also referred to as shears of second order (McKinstry, 1953), secondary faults (Chinnery, 1966) or tip-line bifurcations (e.g. Walsh et al., 2003). A splay fault is typically at an angle of up to 45° to the master fault, with a cone-shaped lens limited by the splay fault and its master fault (Perrin et al., 2016).

The variable terminology describing splays is caused by different nucleation points of the subsidiary fault. Tip-line bifurcation (and splay) is usually used when a propagating fault is split into two segments caused by heterogeneity in the mechanical properties of the host rock (Huggins et al., 1995) or by reactivation of a fault due to stress field reorientation (Woods, 1992; Walsh et al., 2003). This implies that the displacement should be at maximum at the linkage area between the splay fault and the master fault, and decrease with increasing distance to the master fault (Perrin et al., 2016 and references therein). A splay fault may also form passively as an abutment to the main fault, often seen in cross-sections of breached relay zones (Fig. 2.6) (e.g. Childs et al., 1995; Walsh et al., 1999; Bonson et al., 2007; Fossen and Rotevatn, 2016). This implies that minimum displacement of the splay fault should be at the linkage area of the master fault, and the displacement would increase with increasing distance to the fault (Childs et al., 1995; Walsh et al., 1999; Bonson et al., 2007; Fossen and Rotevatn, 2016).

“Splay faults” will as mentioned be termed as a geometrical feature, referring to a synthetic fault causing a cone-shaped geometry, without determination of the nucleation point of the splay fault. Splay faults are most often formed in the hangingwall of the master

fault, although they occur in the footwall (Perrin et al., 2016). They will be included in the linking damage zones of Kim et al. (2004) or in single tip interaction damage zones of Fossen et al. (2005). The linkage point of a splay zone represents a branch line in 3D (e.g. Walsh et al., 1999; Imber et al., 2004; Bonson et al., 2007). Branch lines and linkage areas typical represent areas of strain localisation, it is reported that e.g. fault breccias are formed along branch-lines (Bonson et al., 2007). At early stages in the relay zone, the branch-line may be represented by only a point in 3D, continued growth and breaching of the relay zone (development of a splay zone) will result in a progressively longer branch-line (L- to U- to O-shaped) replacing the tip-line, and may result in a lens surrounded by a continuous branch-line (Fig. 2.6) (Walsh et al., 1999).

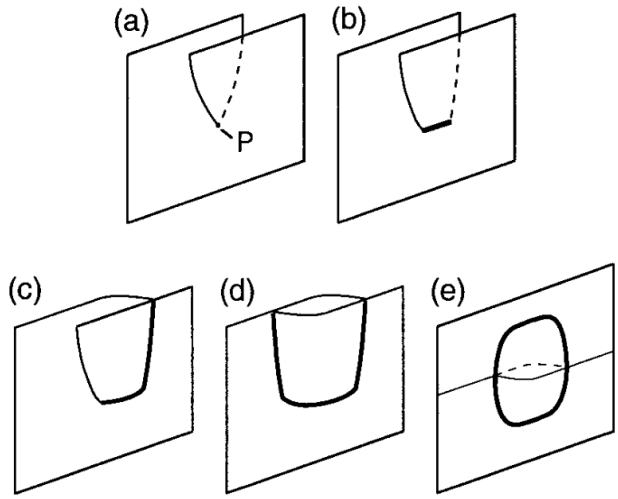

Figure 2.6: Illustration showing the development of a simple relay to a lens and the associated branch-lines (a) Two fault segments overlapping (soft-linked relay) with intersecting branch points (P). (b) Breaching of the relay in the form of a branch-line (bold line). (c) Hard-linkage and an L-shaped branch line. (d) A doubly breached relay ramp showing a U-shaped branch-line. (e) A lens is formed showing a closed branch-line. Note that all these scenarios might show a splay fault in cross section. Figure from Walsh et al. (1999).

2.4 Fracture networks

2.4.1 Fracture geometry and properties

Characterisation of fractures in the field is difficult because outcrops are usually restricted to fracture traces in 2D or in pseudo-3D in the case of the combination of horizontal and vertical outcrops. Outcrops do, however, give much more data than available for fractures in subsurface reservoirs (e.g. Dershowitz and Einstein, 1988). For example, imaging

techniques often have a low resolution and the rock volume of a core is too small to represent the large fracture distribution, as their dimensions are greater than the core (Laubach, 1988; Ortega and Marrett, 2000). Tests show, however, that the fracture orientation and frequency are similar in micro-scale and macro-scale, which can be used for description of a fractured core (e.g. Ortega and Marrett, 2000).

2.4.2 Network properties

A fracture network is the arrangement of two or more fractures that may, or may not interact kinematically and/or geometrically. They display a range of orientations, lengths and sizes (e.g. Laubach, 1992; Manzocchi, 2002; Nixon, 2013). Whilst there are many ways to describe single fractures, the characterisation of fracture networks is more problematic (e.g. Bolander and Saito, 1998). The connectivity (i.e. connections per branch or connections per line) in a fracture network is accomplished where fractures are crossing, abutting or splaying (Manzocchi, 2002). Quantifying the connectivity and adding information about aperture or cementation, could be used to recognise if the fracture network will act as a conduit, baffle or a barrier for fluid flow (e.g. Ortega and Marrett, 2000; Sanderson and Nixon, 2015).

Dershowitz and Einstein (1988) present two approaches to characterise fractures. The first approach is to describe single fractures by its length, aperture, orientations, spacing, fracture type, fracture fill and curvature etc. These values are often represented by average values or in plots to describe the fracture population and is widely used (e.g. Priest and Hudson, 1976; Ladeira and Price, 1981; Huang and Angelier, 1989; Rives et al., 1992; Wu and Pollard, 1995; Sanderson and Nixon, 2015), but will exclude the relationship between the fractures. The second approach is a network model that assumes planar fractures representing a specific geometry (Dershowitz and Einstein, 1988). In this thesis, I use both the single fracture and network approaches to describe different damage zones and the geometric changes occurring along a fault (Section 2.2). Various authors have tried to quantify the connectivity of fracture networks (Laubach, 1992; Bolander and Saito, 1998; Ortega and Marrett, 2000; Manzocchi, 2002; Nixon, 2013; Sanderson and Nixon, 2015; Morley and Nixon, 2016). Laubach (1992) plot fracture terminations in triangular plots, where the end-members are; (1) dead-end termination, including the blind tips of fractures; (2) connected terminations, which is the point where

fractures are abutting or crossing and; (3) constricted terminations, which are intersections of narrow fractures or micro-fractures who provide a connection to neighbouring fractures. The constricted fractures are below the map-resolution of Laubach (1992), but observed in the field. Ortega and Marrett (2000) used a semi-quantitative approach for fracture connectivity, where proportions of connected branches in a network are included. Manzocchi (2002) quantifies I-, Y- and X-nodes and their proportions. I-nodes (isolated nodes) would equal the dead-end terminations (Laubach, 1992), Y-nodes would be the points where the fracture splay or abut and X-nodes would be the point of crossing fractures, hence Y- and X nodes are connecting nodes. The proportions of nodes are plotted in triangular plots to illustrate the contrasts of different fracture networks (Manzocchi, 2002). Manzocchi (2002) also defines number of connections per line (N_L) which quantifies the connectivity. I-, Y- and X-nodes and the triangular plots in addition to connections per line were later used by Sanderson and Nixon (2015) in using topology to characterise fracture networks, which is the main approach in this thesis.

2.4.3 Topology

Topology has been used to describe networks in natural, engineering and social sciences (Latora and Marchiori, 2002; Ravasz and Barabási, 2003; Boccaletti et al., 2006), and is used here to describe the 2D topological character of various fault damage zones (Section 4.1). Topology described the geometrical relationship between and the arrangement of fractures. It also has importance for assessing and quantifying the connectivity in addition to characterise networks (Manzocchi, 2002; Nixon, 2013; Sanderson and Nixon, 2015; Morley and Nixon, 2016; Duffy et al., in review).

A fracture network can be characterized by lines (fracture traces), nodes and branches, which represent a segment of a line limited by nodes (Fig. 2.7) (Manzocchi, 2002; Sanderson and Nixon, 2015; Morley and Nixon, 2016). The topological character of a fracture network is important as two fracture networks can have similar trace lengths, orientation and fracture intensities, but different topologies (Sanderson and Nixon, 2015), which could give very different fluid flow properties. With the use of nodes (I-, Y- and X-nodes), three types of branches are characterised; fully isolated branches (II), partly connected branches (IC) and fully connected branches (CC) (Fig. 2.7). The

proportions of nodes and branches can be plotted in triangular plots and used to address how the fractures relate to each other in a fracture network (Ortega and Marrett, 2000; Manzocchi, 2002; Sanderson and Nixon, 2015). An underdeveloped fracture network would typically include a domination of I-nodes and show low connectivity, while more mature networks will include a higher proportion of Y- and X-nodes and will show a higher connectivity (Sanderson and Nixon, 2015). Note that fracture networks normally include higher proportions of Y-nodes, relatively to X-node. This can be explained by the preservation problem when an active fault accumulates displacement and that younger joint usually stops at older joints, resulting in two Y-nodes rather than one X-node in 2D (Morley and Nixon, 2016).

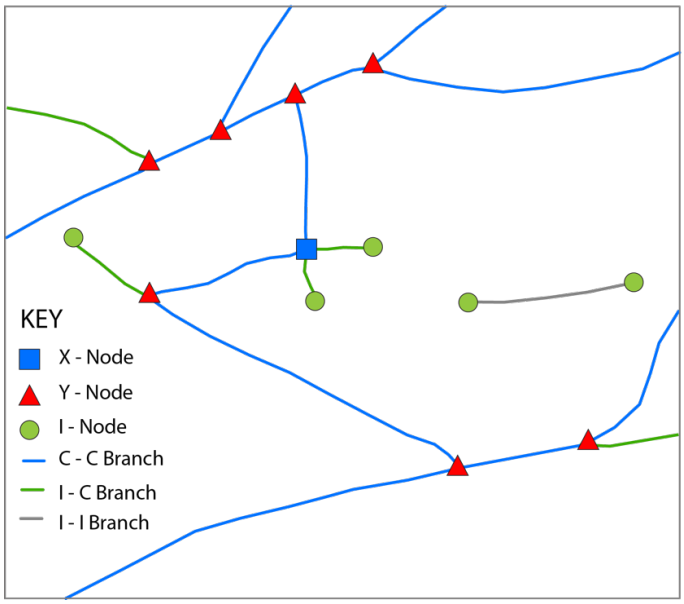

Figure 2.7: Illustration and legend of nodes and branches, displaying X- Y- and I-nodes and the following branches. Terminology from Sanderson and Nixon (2015).

Nodes are points when viewed in 2D, but are lines in 3D, with Y-nodes being branch-lines (Fig. 2.6) and I-nodes being tip-lines (Childs et al., 1995; Huggins et al., 1995; Walsh et al., 1999). With the use of topology (nodes and branches), information of network properties including the connecting node frequency and the connectivity is quantified by connections per line (Cl) and/or connections per branch (Cb). Information is also obtained about single fractures, including fracture frequencies, fracture intensities and dimensionless intensities (Section 4.1) (Sanderson and Nixon, 2015).

3 Geological setting

This chapter provide an overview of the regional structural development (Section 3.1) and the stratigraphic framework (Section 3.2) of the field Mediterranean region. The chapter is mainly focused on the Pantelleria Rift and the Maltese Archipelago.

3.1 Regional tectonic setting

3.1.1 Tectonic evolution of the Central Mediterranean

Today's arrangement of the Mediterranean region is a consequence of the birth and destruction of the major Palaeotethys (Palaeozoic), Neotethys (Palaeozoic-Mesozoic) and the Alpine Tethys-Valais (Mesozoic) oceans. This was a result of tectonic interactions between the Eurasian and Africa-Arabian plates (Cavazza and Wezel, 2003). The evolution includes convergence, extension, rotation of blocks and accretion, in addition to slab roll-back during subduction (Rosenbaum et al., 2002).

The SE-directed subduction of the Alpine-Bentic system, reached the continental collision stage in Miocene times. As a result of this orogeny and the thick continental crust, subduction could not continue and led to inversion. Thinned crust at the SE-front of the Alpine-Bentic system, allowed the Apennines-Maghrebides system to develop along this weak zone. The back arc extension of the Apennines-Maghrebides west directed subduction led to fragmentation of the old Alpine-Bentic Orogen. Slab roll-back further resulted in the opening of Late Oligocene-Miocene (Provençal, Valença, Alboran) basins (Gueguen et al., 1998). Several microcontinents (Kabylies, Balearic Island, Sardinia-Corsica, Calabria) also rifted off the European – Iberian continental margin in Neogene times, favouring the development of basins in the weakened continental crust (Cavazza and Wezel, 2003). The Miocene - Pleistocene (Algerian and Tyrrhenian) basins are back arc basins as a result of eastward slab roll-back of the westward Apennines - Maghrebides subduction (Gueguen et al., 1998).

The basins in the central-western Mediterranean are progressively older from the east to the west (Rehault et al., 1984; Carminati et al., 2012). The central-western basins

developed during the last 30-40 Ma, and are younger than the eastern Mediterranean, which is suggested to be comprised of Mesozoic oceanic crust or thinned continental crust (Robertson and Dixon, 1984; Carminati et al., 2012).

3.1.2 The Pelagian Platform

Malta, Gozo and Comino are the three main islands of the Maltese Archipelago. The Maltese Islands, located in western Central Mediterranean between Sicily and Tunisia, are one of the few emerged areas of the Pelagian Platform (Fig. 3.1) (Reuther and Eisbacher, 1985). The Pelagian Platform consists of the northern part of the African plate and is morphologically described as an epicontinental sea. It is limited by southern Sicily to north-western Libya and eastern Tunisia (Morelli et al., 1975; Finetti, 1984; Micallef et al., 2013). The Pelagian platform consists of 6-7 km thick Mesozoic to Cenozoic carbonates and volcanics. The age and character of the underlying basement is not well known, but Precambrian granites and metamorphic rocks have been drilled on the mainland of Tunisia (Burollet, 1991; Civile et al., 2010) and the North African margin (Jongsma et al., 1985). Morelli et al. (1975) also support a continental character for the upper crust.

The Pelagian Platform can be divided into four structural provinces: 1) The ESE- WNW striking Pantelleria Rift system; 2) The Malta Plateau, which forms the NE shoulder of the rift system; 3) a NNW- SSE striking extensional fault system, the Malta Escarpment, separating the oceanic crust of the Ionian basin from the continental crust of the Malta Plateau; 4) The Apennine – Maghrebian fold-and-thrust belt, along the Eurasian-African plate boundary to the north and west margin of the Pelagian Platform (Fig. 3.1) (Dart et al., 1993; Micallef et al., 2013).

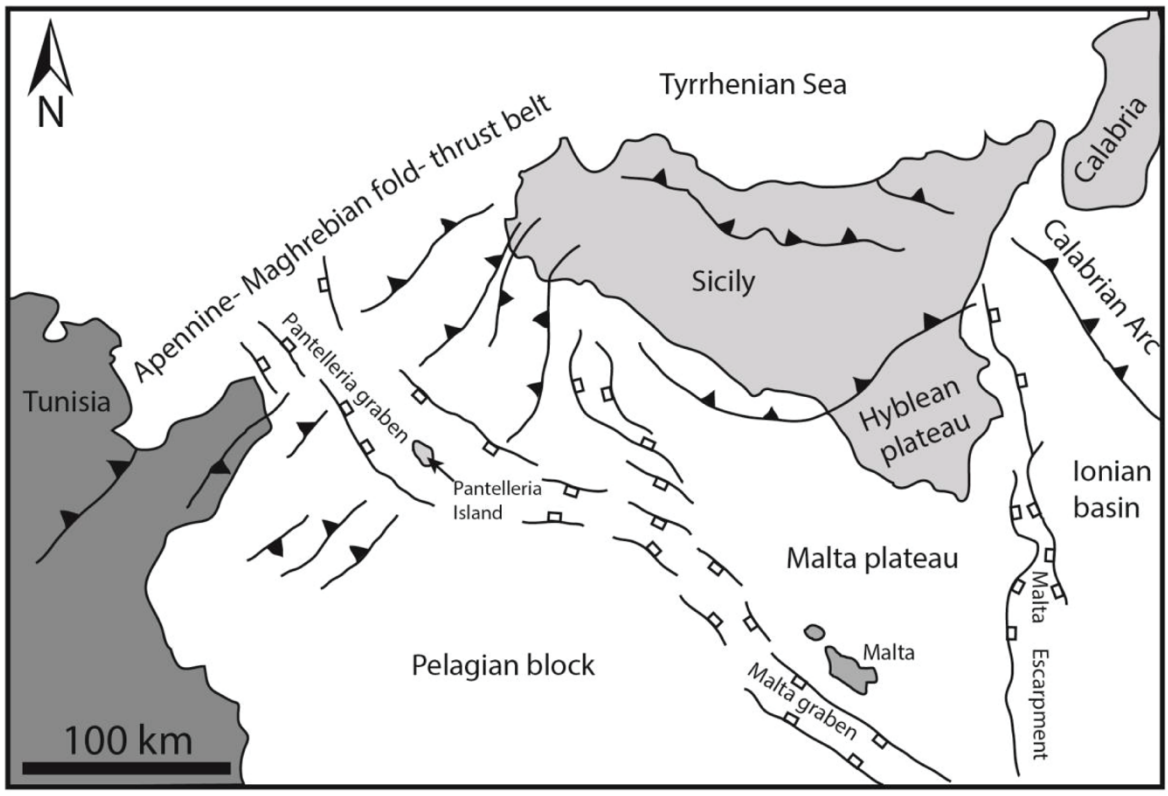

Figure 3.1: Four structural provinces of the Pelagian Platform: 1) The Pantelleria Rift system, 2) The Malta Plateau (and the Hyblean Plateau), 3) The Malta Escarpment, separating the oceanic crust of the Ionian basin from the continental crust of the Malta Plateau; 4) The Apennine – Maghrebian fold-and-thrust belt. Figure from Fossmark (2015) modified after Granath and Casero (2004).

3.1.3 The Pantelleria Rift system

The Maltese Islands are located at the northern shoulder of the Pantelleria Rift system (Reuther and Eisbacher, 1985; Bonson et al., 2007), also called the Sicily Channel Rift (Civile et al., 2010) or Strait of Sicily Rift (Morelli et al., 1975; Cello et al., 1985; Finetti, 1985). The Pantelleria Rift system is an ESE – WNW-striking, 600 km long, elongated trough (Bonson et al., 2007), located in the foreland of the Apennine – Maghrebian trust-and-fold belt (Fig. 3.1) (Reuther and Eisbacher, 1985; Hill and Hayward, 1988; Pedley, 1990; Dart et al., 1993; Bonson et al., 2007). From regional seismic data it is recognised that the Pantelleria Rift is characterised by half grabens and full grabens (Jongsma et al., 1985; Dart et al., 1993). The three main troughs of the rift are the Pantelleria-, Linosa- and Malta troughs and are controlled by NW-trending faults. The water depth of the troughs ranges from 1300 m to over 1700 m, although the water depths are less than 400 m for the rest of the platform (Finetti, 1984; Jongsma et al., 1985; Dart et al., 1993; Civile et al.,

2010). The troughs (Pantelleria, Linosa and Malta) are filled with Plio – Pleistocene turbidites with thicknesses from 1 to 2 km (Civile et al., 2010).

In Plio - Quaternary times the main rifting of the Pantelleria Rift occurred, resulting in faults with throw up to 2.2 km (Finetti, 1984; Dart et al., 1993; Bonson et al., 2007; Civile et al., 2010). Two volcanic islands, Pantelleria and Linosa, also formed as a response to the rifting where the main volcanic activity occurred during Plio – Pleistocene and continued to present day (Calanchi et al., 1989; Civile et al., 2010). The volcanics are typical alkali basalts and hawaiites (Corti et al., 2006) and the petrology indicate anorogenic magmatism in a continental rift setting (Corti et al., 2003).

Interpretation of the troughs of the Pantelleria Rift traditionally have been interpreted as pull-apart basins involving deeper crustal levels as a result of a E-W trending, dextral wrench zone (Finetti, 1984; Cello et al., 1985; Jongsma et al., 1985; Reuther and Eisbacher, 1985; Robertson and Grasso, 1995; Civile et al., 2010). Argnani (1990) postulated that both slab roll-back and mantle convection due to delamination could have produced a N-S extension related to the Apennine-Maghrebian compression. Fault slip data from Dart et al. (1993) also support that fault sets in the Maltese islands is a result of N-S oriented extension, even though the data are biased to onshore exposures of the North Malta Graben. The troughs (Pantelleria, Linosa and Malta) are approximately oriented normal to the collisional front to the NW of the rift, which began in Late Miocene based on the sedimentary succession, which also support a N-S oriented extension (Reuther and Eisbacher, 1985; Dart et al., 1993; Robertson and Grasso, 1995). Grasso et al. (1986) also support a NNE – SSW extension to explain the two fault sets found on the Maltese Islands and in the Pantelleria rift system.

3.1.4 The Maltese Graben system

Uplift of the NNE flank of the Pantelleria Rift and a falling sea level from Miocene times led to emergence of the present day Maltese Archipelago in Messinian times (Pedley, 1987b; Bonson et al., 2007). The Maltese graben system comprises of several extensional basins which is a small part of the Pantelleria Rift (Dart et al., 1993). Five main tectonic structures can be recognised from the Maltese graben system: 1) North Gozo Graben; 2) Gozo Horst; 3) North Malta Graben; 4) Malta Horst; 5) the Pantelleria Rift (Fig. 3.2) (Dart

et al., 1993). The North Gozo Graben and the North Malta Graben intersect the Pantelleria Rift at 66° and 32° respectively (Dart et al., 1993).

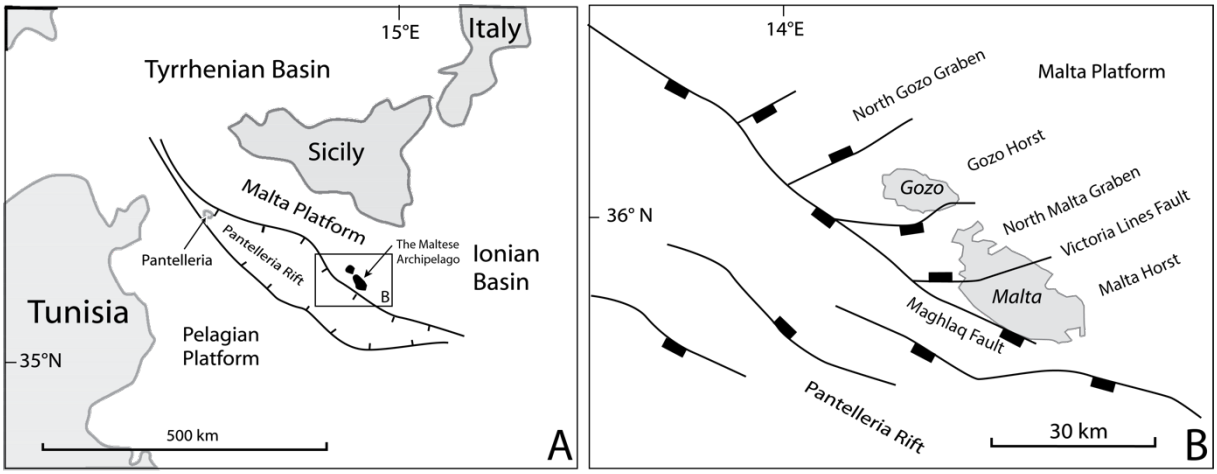

Figure 3.2: A: The Maltese Archipelago emerged at the Northern shoulder of the Pantelleria Rift, between Tunisia and Sicily. B: The Maltese graben comprises of five main units: 1) North Gozo Graben; 2) Gozo Horst; 3) North Malta Graben; 4) Malta Horst and; 5) The Pantelleria Rift. Figure modified from Missenard et al. (2014) and Dart et al. (1993).

Contour maps of Malta by Pedley et al. (1976) indicate that the strata are gently folded and are offset by faults, which is also supported by Dart et al. (1993). The majority of the faults in Malta strike ENE – WSW and are close to orthogonal to an ESE – WNW fault set, which gives two distinct extensional trends (Fig. 3.2) (Pedley et al., 1976; Illies, 1980; Reuther and Eisbacher, 1985; Dart et al., 1993; Bonson et al., 2007). The Maghlaq Fault is exposed at the southwestern coast of Malta, and is the only exposed major fault in the Maltese Archipelago with a Pantelleria Rift trend (ESE-WNW). The fault has the highest displacement of > 210 m on the Maltese islands (Bonson et al., 2007). The Victoria Lines Fault, also called the Grand Fault (Murray, 1890), is striking towards the ENE –WSW like the majority of the faults in Malta (Fig. 3.2). Victoria Lines Fault has a displacement of 195 m, which is the highest in the North Malta Graben, separating the graben from the Malta Horst to the south. Both the main Maghlaq Fault and the faults with the same trend as Victoria Lines Fault are formed as a result of an N-S directed extension (e.g. Dart et al., 1993).

3.2 Regional stratigraphic framework

The stratigraphy of the Maltese islands is dominated by marine, shallow water carbonates. The five main formation of the Maltese islands have been documented by previous workers (e.g. Murray, 1890; Felix, 1973; Pedley et al., 1976; Bosence and Pedley, 1982; Mazzei, 1985; Pedley, 1987b, a, 1990; Dart et al., 1993), but there is a lack of work on the regional stratigraphy in recent times. Based on onshore exposures of the Maltese Islands and fault-related thickness changes of offshore 2D seismic data, a four staged tectono-sedimentary evolution is suggested for the Miocene – Quaternary period (Fig. 3.3): (1) a pre-rift phase (>21 Ma), which includes the Lower Coralline Limestone Formation and the lowest member of the Globigerina Limestone Formation. (2) An early syn-rift phase (21-6 Ma), which is comprised of the middle and upper member of the Globigerina Limestone Formation, the Blue Clay Formation, the Greensand Formation and the two lowest sequences of the Upper Coralline Limestone Formation. (3) A late syn-rift phase (<5 Ma), which include the third depositional sequence of the Upper Coralline Limestone Formation. (4) A post-rift phase (<1.5 Ma suggested by Dart et al. (1993)), mainly comprising of Quaternary deposits (Fig. 3.3) (Murray, 1890; Pedley et al., 1976; Dart et al., 1993; Bonson et al., 2007).

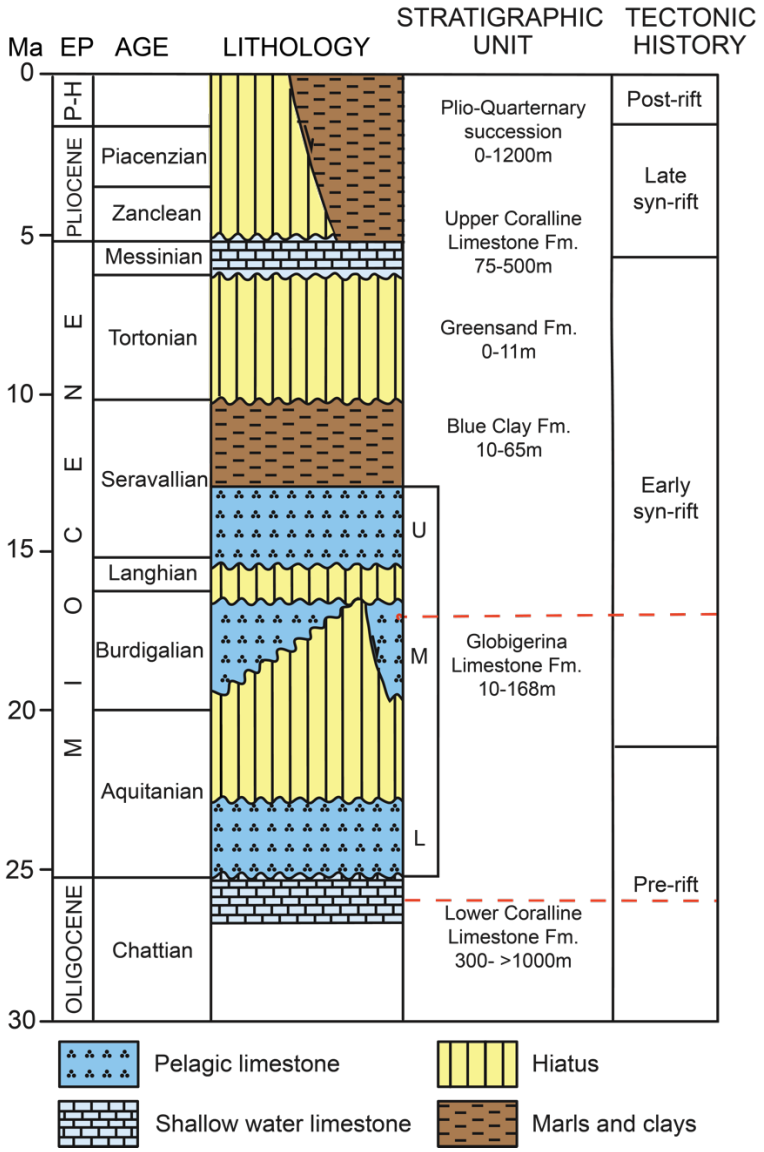

Figure 3.3: The Tectono- stratigraphic log of the Maltese Archipelago from Bonson et al. (2007), originally modified from Dart et al. (1993) and references therein. The log represents the five main formations on the islands and its relation to the tectonic history. EP is abbreviated from "Epoch", where P – H represents "Pleistocene to Holocene" referred to as Quaternary in the text. U, M and L denote "Upper", "Middle" and "Lower" respectively. Numbers below the formation names represent documented thickness variations and the area between the two red, dashed lines indicate the interval exposed in the study area (local stratigraphy of study area in section 5.1).

3.2.1 Pre-rift phase

The Lower Coralline Limestone Formation (LCLF) and the Lower Globigerina Limestone Member (LGLM) comprise the pre-rift succession (Fig. 3.3). The strata show no evidence of fault-related thickness changes or facies-relationship to faults. The sediments were deposited isopachous and tilted by later tectonic movements (Dart et al., 1993).

The upper 140 m of the LCLF are exposed in cliffs at Gozo, although exposures are reduced along the Maltese coastline (Pedley et al., 1976). The unit is generally dominated by shallow water coralline algae limestones and the upper limit is marked by a hardground surface (Bennett, 1979; Dart et al., 1993). Hardground surfaces represent non-depositional periods where the sediments were just under or above the sea-level, causing biochemical and chemical alteration of the sediments (Felix, 1973), which gives a distinct, flat hardground also seen in the field area. The lower part of the exposed LCLF has been interpreted by Felix (1973) as deposits from a shallow gulf environment with increasing open marine conditions upward in the formation. Further the depositional environment is a shallow marine shoal environment, with an exception of SE Malta, where protected, deeper water led to calmer conditions.

The LGLM is the oldest member of the Globigerina Limestone Formation (GLF), which is named by its high (up to 80-90%) amount of planktonic foraminifera (*Globigerina*) (Fig. 3.3) (Murray, 1890; Felix, 1973) and comprises of wackestones and packstones (Pedley, 1987b). The thickness of the Lower Globigerina Limestone Member biomicrites ranges from < 2 m to > 100 m. It is characterised by its honeycomb weathering due to erosion of softer sediments and less erosion of harder intra-burrow cementation (Pedley, 1987b). A phosphorite conglomerate (C1) marks the top of the LGLM (Felix, 1973), described as a second hardground surface (Bennett, 1979; Dart et al., 1993). The conglomerate is generally < 1 m thick (Pedley et al., 1976) and is cut by neptunian dykes marking the onset of the early syn-rift phase (Bennett, 1979; Dart et al., 1993). The depositional environment of LGLM is interpreted by Felix (1973) as a shallow marine platform showing an increase in water depth (Pedley et al., 1976).

3.2.2 Early syn-rift phase

The Middle Globigerina Limestone Member (MGLM), Upper Globigerina Limestone Member (UGLM), Blue Clay Formation, Greensand Formation and the two lowest sequence of the Upper Coralline Limestone Formation (UCLF) all form a part of the early syn-rift succession (Fig. 3.3). These units show subtle thickness variations related to faults, fault-related bathymetric relief and neptunian dykes (Dart et al., 1993) suggesting that the faults were active during deposition of these sediments.

The MGLM comprise of biomicrites similar to LGLM. In the study area, south of Fomm ir-Rih Bay (Fig. 1.1), smaller grained, weaker and lighter phosphorite horizons and nodules of chert are observed (Pedley et al., 1976). The eroded top of the LGLM phosphorite conglomerate is disconformable overlain by the MGLM and its thickness ranges from non-existing, in east Gozo, to 110 m. The MGLM upper limit is also marked by a new main phosphorite conglomerate (C2), which is about 0.5 m thick (Pedley et al., 1976; Bennett, 1979).

The UGLM consist of biomicrites and its thickness ranges from zero in central-eastern Malta to > 20 m in Mellieha, Malta. It is overlying the second phosphorite conglomerate of MGLM (C2) (Morris, 1952; Pedley et al., 1976; Bennett, 1979).

A transition from globigerinid biomicrites of the GLF to globigerinid marls, clays and mudstones marks the base of the Blue Clay Formation, which contains less than 30% carbonate material (Murray, 1890; Pedley et al., 1976). The thickness generally ranges from < 20 m to 65 m at Malta (Pedley et al., 1976), although its maximum thickness is reported to be 96 m from a well in eastern Pantelleria Rift (Dart et al., 1993). The formation has been interpreted by Pedley et al. (1976) to have been deposited in open, muddy marine conditions with water depth from 150 m in the lower part of the formation to 100 m in the upper part. The transition from the Blue Clay Formation to the Greensand Formation is erosive and sharp (Mazzei, 1985).

The Greensand Formation comprise of carbonaceous, bioclastic, glauconitic sand. The glauconitic grains give the formation a distinct greenish colour (Pedley et al., 1976; Dart et al., 1993). It is poorly cemented and therefore easily eroded (Mazzei, 1985). The formation is generally < 1m thick, but it is locally up to 11m thick in local basins at Gozo (Pedley et al., 1976; Dart et al., 1993). The intense bioturbation of the formation suggest a shallow marine depositional environment (Pedley, 1987b). The transition to the overlying UCLF is transitional (Mazzei, 1985).

The UCLF is similar to LCLF and is divided into three depositional sequences (Pedley et al., 1976; Dart, 1991; Dart et al., 1993). The two lowest depositional sequences are early

syn-rift strata (Dart et al., 1993). The first depositional sequence consists of algae biostrome facies (Bosence and Pedley, 1982), whereas the second depositional sequence consists of coarser grained oolitic and bioclastic limestone, with coal and algae patch reef facies in the western areas (Pedley et al., 1976; Dart, 1991; Dart et al., 1993). Both depositional sequence one and two have facies belt trending N-S, sub-perpendicular to the North Malta Graben (Bosence and Pedley, 1982; Dart et al., 1993) and the depositional sequence two show facies changes over the Victoria Lines Fault (Bosence and Pedley, 1982; Pedley, 1987b). Algae biostrome facies of depositional sequence one represents a stable seabed and the biomicrites facies are deposited on the leeward side of the margin of an open shelf. The oolitic and bioclastic limestones of depositional sequence two represent the lee-side of the patch reef in a local tidal delta (Pedley et al., 1976).

3.2.3 Late syn-rift phase

The late syn-rift succession comprises of depositional sequence three of the UCLF as well as turbidites and hemi-pelagic sediments from Plio-Quaternary times (Fig. 3.3). Their facies distributions are strongly fault-controlled, and zones of fault growth show erosion of footwall and deposition in hangingwall (Dart et al., 1993).

The third depositional sequence is only locally preserved in NW Malta and Bingemma-Fomm ir-Rih in western Malta. It consists of cross-stratified, oolitic, pelletoidal and bioclastic limestones (Pedley et al., 1976). The Maghlaq Fault in Ras Hanzir show platform facies at the footwall and slope facies in the hanging wall (Pedley, 1987a; Dart, 1991; Dart et al., 1993), which suggests a late stage of rifting with high relief over the major faults. The deposits generally indicate a shallow subtidal environment, however a reduction of microfossils, lack of macro-fauna and a stromatolite suggests an intertidal or supratidal environment in the upper part of the sequence (Pedley et al., 1976).

The Central Mediterranean was re-flooded during Pliocene where marls and carbonate mudstones were deposited over the UCLF in the Pantelleria Rift and North Gozo Graben and is referred to as the Plio-Quaternary succession. These sediments can be correlated to Sicily (Murray, 1890; de Visser, 1992; Dart et al., 1993). The Pantelleria Rift and the North Gozo Graben had high relief before re-flooding, in contrast to Gozo Horst, North Malta Graben and Malta Horst where Pliocene deposits are non-existent (Dart et al.,

1993). The Plio-Quaternary succession is cut by major faults and not by minor faults, indicating that the rifting was at a late stage at the time, and only the major faults were active.

3.2.4 Post-rift phase

Jongsma et al. (1985) reports that the lack of seismicity since 1965 cannot be used to draw any conclusions on the activity of faults at present. This is due to the short period of observation and the poor distribution of observatories. Even though he reports, based on observations on seismic data, that a smooth seafloor suggests that faulting did occur *prior* to Pliocene times and that minor deformation is a result of differential compaction. Dart et al. (1993) on the other hand, states that the lack of seismicity suggests that sedimentation today occurs in the post-rift phase, and that there is a diffuse transition between the syn-rift and post-rift sediments. Onshore the Quaternary deposits are comprised mainly of talus- and alluvial fan deposits forced in response to the retreat of fault scarps (Trechmann, 1938; Dart et al., 1993).

4 Methods

This chapter introduces the methods used in this study, starting with topology (Section 4.1). Further, it describes the workflow in the field (Section 4.2), during data processing and the statistical analysis (Section 4.3) (Fig. 4.1). Sources of errors are discussed lastly (Section 4.4).

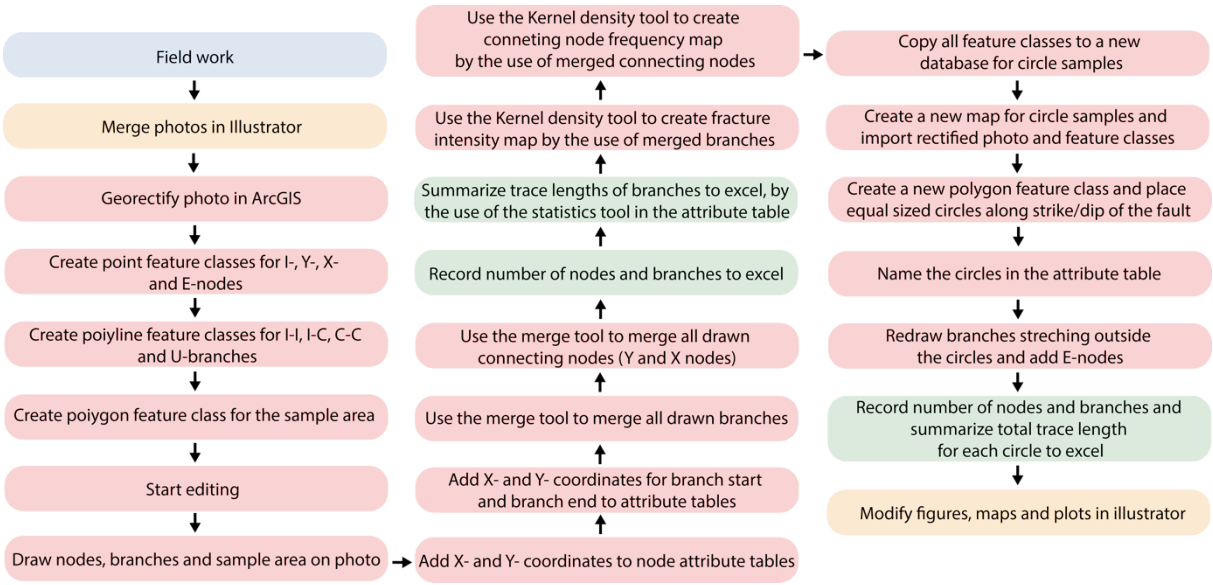

Figure 4.1: Simplified illustration of the workflow used in this study. Note that blue indicates field work (Section 4.2), orange indicates work in Adobe Illustrator CC, red indicates work in ArcGIS and green indicates work in Excel (Section 4.3) (see Appendix I for workflow in ArcGIS and Excel).

4.1 Topology

Topology describes the geometrical relationships fractures have to each other and the resulting connectivity. Topology defines a fracture network as a system of nodes and branches between nodes (Manzocchi, 2002; Nixon, 2013; Sanderson and Nixon, 2015; Duffy et al., in review) (Section 2.4.2 and 2.4.3). An I-node represents the tip of a fracture, a Y-node represents the point of splaying or abutting fractures and an X-node represents the crossing point of two fractures. Y- and X-nodes are therefore connecting nodes (Fig. 4.2) (Manzocchi, 2002; Sanderson and Nixon, 2015). The total number or nodes (N_N) is the sum of the number counts of each node type: I-nodes (N_I), Y-nodes (N_Y) and of X-nodes (N_x). The node proportions (P_I, P_Y *and* P_X) can be illustrated in the triangular node

plot (Fig. 4.3). Branches are limited by one node at each end and are grouped based on the number of connecting nodes; isolated branches (II), partly connecting branches (IC) and fully connecting branches (CC) (Ortega and Marrett, 2000; Sanderson and Nixon, 2015) (Fig. 4.2).

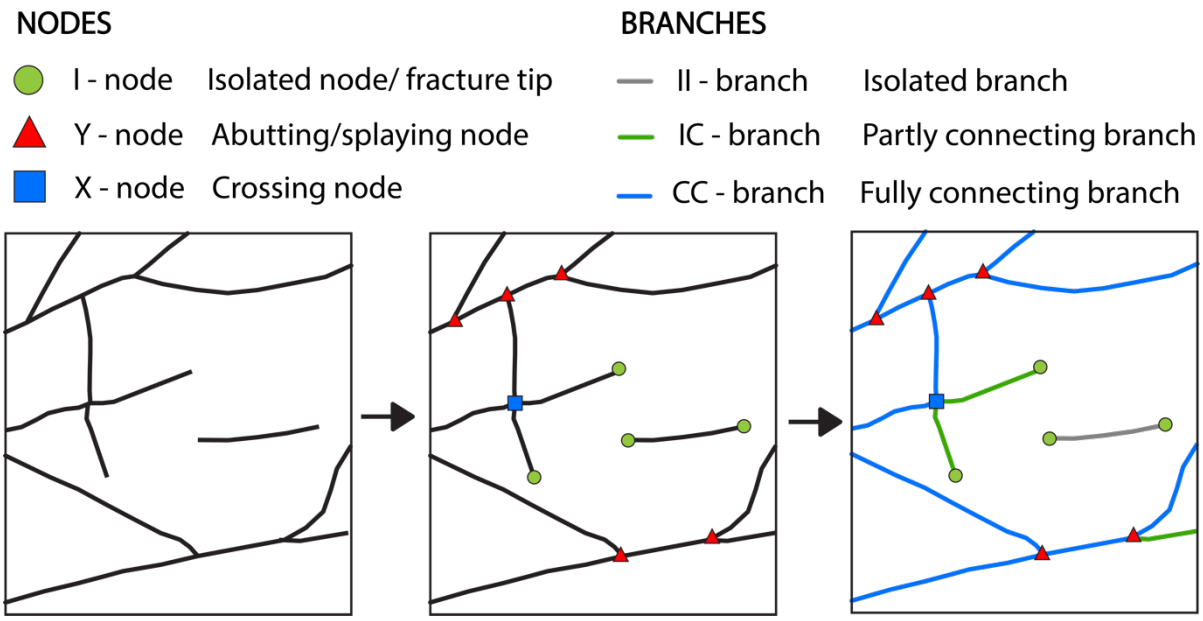

Figure 4.2: Example of the terminology used in topology demonstrated with a rectangular sample area. From a fracture system we define three types of nodes, which represents points of intersections or tips of fractures; fracture tips/ isolated node (I-node), fracture abutments/splays (Y-node) and crossing fractures (x-nodes). The two latter therefore represent connecting nodes. From the nodes, three branch types may be defined; Isolated branches (II-branch), which is limited by two I-nodes, partly connecting branch (IC-branch) limited by one I-node and one connecting node and fully connecting branch (CC-branch) limited by two connecting nodes. The figure illustrates the fixed colours and symbols used in ArcGIS software. Terminology from Sanderson and Nixon (2015).

4.1.1 Connectivity

The number of each branch types may be counted or mathematically calculated. As I-nodes, Y-nodes and X-nodes are associated with 1, 3 and 4 branches, respectively. Then the number of branches (N_B) will be (see Table 1 for abbreviations) (Sanderson and Nixon, 2015):

$$N_B = \frac{1}{2}\,(N_I + 3N_Y + 4N_x) \qquad (1)$$

The average connections per branch (C_B) is be defined to assess the degree of connectivity of a fracture system (Sanderson and Nixon, 2015):

$$C_B = (3N_Y + 4N_x) \,/\, N_B \qquad (2)$$

Connections per branch (C_B) is a dimensionless parameter and ranges from a minimum of 0 to a maximum of 2 connections per branch. C_B is an expression for the connectivity and can be contoured into the triangular node- and branch plots (Fig. 4.3) (Sanderson and Nixon, 2015).

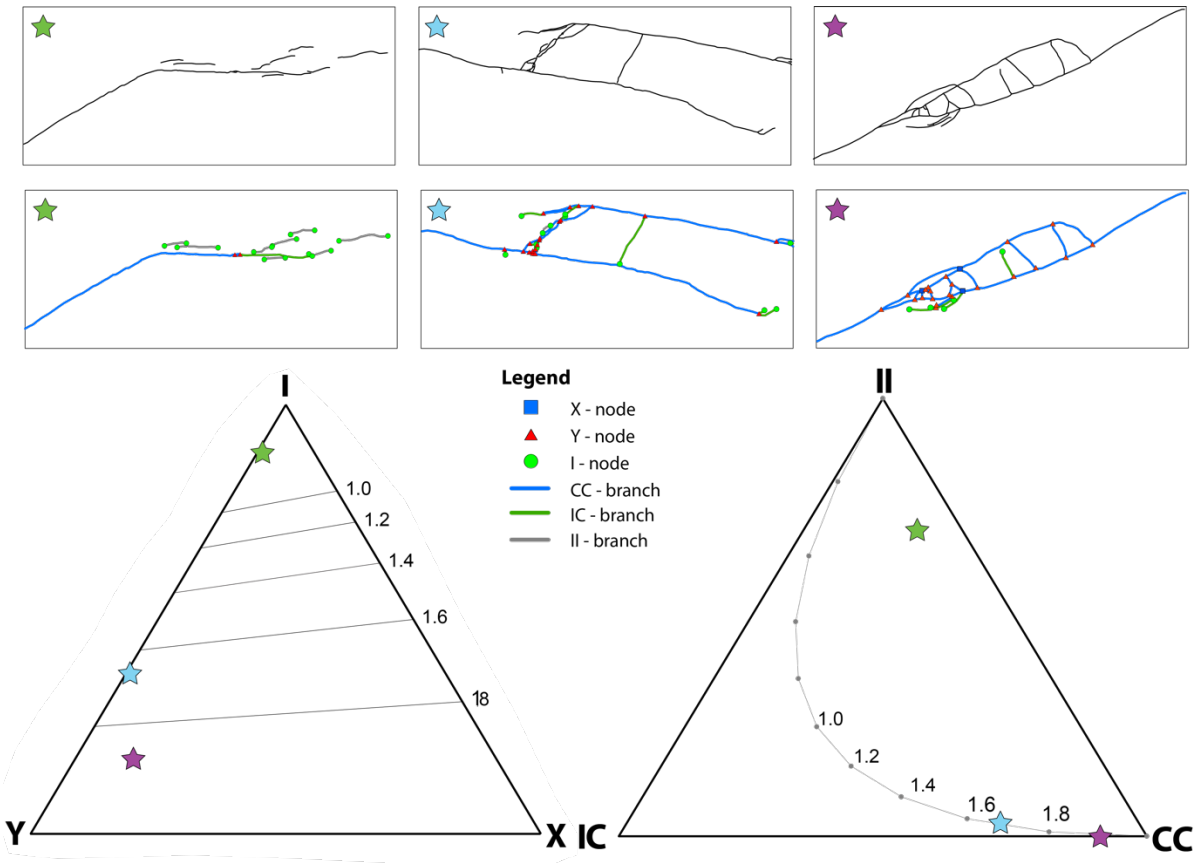

Figure 4.3: Examples of the topology of three small-scale normal fault damage zones. The green star represents a fault tip damage zone, blue and purple stars represents relay damage zones. From the node plot (I, Y and X) and the branch plot (II, IC, CC) it is clear that the green damage zone is dominated by I-nodes and II-branches, while the purple damage zone shows the highest amount of Y- and X-nodes and are therefore dominated by CC-branches. Average connections per branch (C_B) are also shown in both plots.

4.1.2 Euler's theorem – number of faces

Additionally, the number of faces (number of blocks) in the 2D plane may be calculated based on nodes and branches. The formula is based on Euler`s theorem, which states (Richeson, 2012; PowerPoint from David Sanderson) (Table 1):

$$N - B + F = 2 \quad \textbf{or} \quad F = 2 - N + B \tag{3}$$

This theorem includes an "external face", which is replaced by the number of faces that is partly in the circle sample or sample area (N_E) and counting them as half faces, which gives (Table 1):

$F = N_F + 1 - N_E/2$

$N = N_N$

$B = N_B - N_E/2$

Replaced in Euler`s theorem (Table 1):

$$N_N - (N_B - N_E/2) + (N_F + 1 - N_E/2) = 2$$

$$N_N - N_B + N_F = 1 \quad \textbf{or} \quad N_F = 1 - N_N + N_B \tag{4}$$

Finally, we need to exclude the II-branches and the associated I-nodes, as we need connecting nodes and branches to form a closed face (Table 1):

$$N_F = 1 - (N_N - N_{II} \times 2) + N_{IC} + N_{CC} \tag{5}$$

The value for number of faces (N_F) represent a theoretical block number for the sample area based on its topology.

Table 1: Overview of abbreviations used in formulas

ABBREVIATION	MEANING
$\boldsymbol{N_N}$ OR $\boldsymbol{N}$	Number of nodes
$\boldsymbol{N_I}$, $\boldsymbol{N_Y}$ AND $\boldsymbol{N_X}$	Number of I-nodes, Y-nodes and X-nodes
$\boldsymbol{N_B}$ OR B	Number of branches
$\boldsymbol{N_{II}}$, $\boldsymbol{N_{IC}}$ AND $\boldsymbol{N_{CC}}$	Number of II-branches, IC-branches and CC-branches
$\boldsymbol{N_E}$	Number of external faces partially in circle / number of E-nodes
$\boldsymbol{N_F}$	Number of faces
$\boldsymbol{C_B}$	Connections per branch i.e. connectivity

4.1.3 Fracture intersection abundances

Fracture intensity (m^{-1}) is defined as the total trace length (m) of the sample area per unit area (m^2) (Section 4.3.2 and 4.3.3). The fracture frequency (m^{-2}) is the number of branches (N_B) of the sample area per unit area (m^2) (Mauldon et al., 2001; Sanderson and Nixon, 2015). The total trace length (m) is the sum of the trace lengths of individual branches (II, IC, CC), which is extracted from the statistics tool in the attribute table in ArcGIS (Appendix I). Note that the polygon (or circle) defining the sample area will tend to intersect with branches. Intersection points between the polygon and branches are marked with edge-nodes (E-node) and branches are handled by counting them as "half branches" (Section 4.3.3). The connecting node frequency (m^{-2}) is the number of connecting nodes (N_c) per unit area (m^2) (Section 4.3.2) (e.g. Sanderson and Nixon, 2015). Dimensionless intensity, average line length and branch length can all be calculated from these parameters (e.g. Sanderson and Nixon, 2015).

4.2 Field methods

Data used in this thesis were collected in Malta during a total of 6 weeks over two field seasons in September - October 2015 and March - April 2016. Fault tip damage zones, splay fault damage zones and relay damage fault zones were selected according to their variability and accessibility.

4.2.1 Fault damage zone description

The fault localities were marked on Google Earth imagery and the GPS position was taken by the use of the apps Basic GPS and GeoID. The 18 fault damage zones were sketched, photographed and described. Throw was measured where possible and the lithologies were recorded. Measurements of strike and dip were taken of the outcrop and on faults and joints. Strike and dip measurements were taken of branches in damage zones, ranging from a few measurements to over 30 measurements in complex damage zones. The dip could commonly not be recorded in horizontal outcrops, so only strikes were measured. All strike and dips measurements were done by the app GeoID and regularly checked using a field compass.

4.2.2 Topology of fault damage zones

The localities were carefully photographed before any collection of topological data. The natural light colour of the Middle Globigerina Limestone Member makes several fractures hard to identify from photographs. To reduce this problem, the fractures were highlighted with a darker colour-pencil, so that the fractures could be recognized from photographs. Accessibility problems meant that fractures were not mapped or highlighted in vertical sections in the field, so these fractures were mapped from photographs later (Section 4.3). 39 circle samples were collected in the field during the first field season. Multiple circle samples allowed the damage zones to be subsamples, with diameters of 0.50 m, 0.27 m, 0.21 m and 0.20 m, depending on the width of the damage zone. The field circle sample were not used for further analysis, but provided a comparative reference frame for later digitised circle samples (Section 4.3.3). The I-, Y- and X-nodes were counted within these circles. Edge-nodes (E-nodes), which represent crossing point between a branch and the circle, were also counted. Thereafter, the circle samples were recorded using photographs. During the second field season, the fault zones were documented before and after drawing on the fractures and the topology was later recorded by using photographs and ArcGIS (Section 4.3).

4.3 Data processing

The photographs and analysis gained from fieldwork were further processed by merging of photographs in Adobe Illustrator CC, topological analysis in ArcGIS and by calculations and creation of plots in Excel (see Appendix I for workflow in ArcGIS and Excel).

4.3.1 Topology in ArcGIS

Merged and scaled photograph of the selected locality is placed in the ArcGIS – map. The topology was digitised using points for nodes, polylines for branches and polygons for sample area (Fig. 4.2 and 4.3). Nodes and branches are drawn directly on the photograph. When all the nodes and branches are drawn, the sample area is drawn as close to the edge of the damage zone as possible. The attribute table, created automatically in ArcGIS, will include the number of features in the specific feature classes. It also includes lengths of

each branch type. Created coordinates for the branch end and start are used to create length weighted rose-diagrams.

The merging tool is used for a simplified overview of the damage zone and for creation of density maps (Section 4.3.2). All branch-types are merged and coloured black. Similarly, all the connecting nodes (Y-and X-nodes) are merged (see Appendix I for full workflow). Topology is done in various scales, were the largest scale is the overall topology of each damage zone, which is mostly used in this study (e.g. Fig. 4.3, Sections 5.2-5.5). Circle samples along strike (Mauldon et al., 2001; Sanderson and Nixon, 2015) represent a smaller sample area and show along-strike variations in fracture intensity, connecting node frequency and number of faces within the damage zone (Section 4.3.3 and 5.6). The smallest sample area is obtained from the density maps, which attributes the fracture intensity and connecting node frequency variations within the damage zones within cells (Section 4.3.2 and 5.2-5.6).

4.3.2 Density maps in ArcGIS

The *kernel density,* available in the toolbar in ArcGIS, was used for the creation of fracture intensity maps and connecting node frequency maps. Fracture intensity maps show total trace length per square metre within a selected cell size in the damage zone. Connecting node frequency maps show the number of connecting nodes per square metre. A cell size and a search radius are selected for each map. Maps were created for each locality at similar scales for all types of damage zones and at separate scales for fault tip damage zones, relay damage zones and splay damage zones. A cell size of 0.5-1.0 cm and a search radius of 4.0 – 10 cm were used for all the maps. Density maps with similar scales for the three types of damage zones were made to study variations between the various damage zones. Density maps for specific damage zones (fault tip, relay and splay) were made to study variations within the same damage zone type at different scales and stages of evolution.

4.3.3 Circle samples in ArcGIS

Circle samples along strike within the damage zone provide an unbiased estimate of the topology, fracture intensity, connecting node frequency and number of faces. Circle

samples eliminates orientation bias, censoring and trace length bias (Mauldon et al., 2001; Sanderson and Nixon, 2015). Circle samples were made along strike of six of the fault zones, two fault tip damage zones, two relay damage zones and two splay damage zones (Fig. 4.4). The circles were drawn in equal size along strike or dip of the main fault or faults of the fault damage zone (see Appendix I for workflow). In each circle, the branches stretching outside the circle was deleted and redrawn to the end of the circle, where it is limited by a drawn E-node (Fig. 4.4). Thereafter, the number of each node and branch type is summarised, in addition to the total trace length and the area of the circle sample.

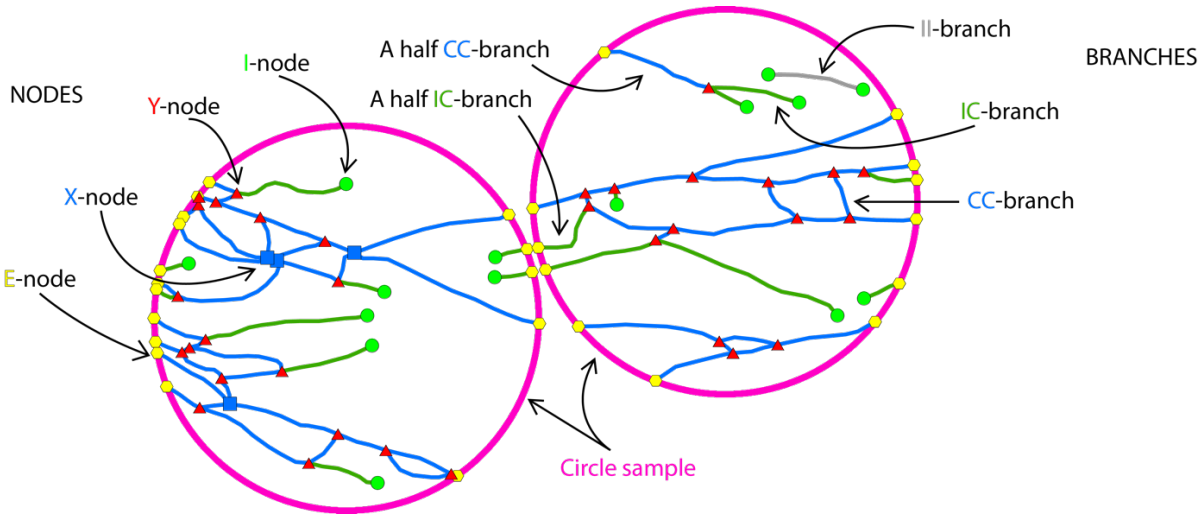

Figure 4.4: Illustration showing a final circle sample in ArcGIS. Nodes and braches are previously drawn in another ArcGIS-project and imported to a new map. The circles are drawn in similar size along strike (or dip). The branches intersecting the circles are redrawn within the circle and marked with an E-node at the intersection point between the branch and the circle. These intersecting braches are counted as half branches for the branch analysis.

4.3.4 Statistical analysis

An excel spreadsheet for topology analysis was populated with data extracted from the ArcGIS maps. Data needed from each locality are; number of each type of nodes, number of each type of branches, total trace length of the locality and the size of the sample area/locality (Appendix I). Each locality and sample area is automatically transferred to triangular plots (in excel) that show the proportions of nodes and branches within the damage zones. The topology of the circle samples is collected separately in a similar way as the whole damage zone. The fracture intensities and the connecting node frequencies

are illustrated in plots instead of density maps, where the along-strike or along-dip variations are shown.

4.4 Sources of error

4.4.1 Sources of errors in the field

Measurements of offset of faults are limited in the field area, due to few regular stratigraphic boundaries and lack of strong regular horizons within the lithologies. The most certain offset measurements are from vertical outcrops over the clear marker bed represented by the conglomerate (LGLM-C1, Fig. 5.3), expressing the boundary between the Lower Globigerina Limestone Member (LGLM) and the Middle Globigerina Limestone Member (MGLM). More uncertain offset measurements were taken at inclined outcrops at weaker and irregular conglomerate horizons (MGLM-C2A and C2B, Fig. 5.3) within the MGLM. In addition, offset-measurements were done over the faults in pavement outcrops, which will lead to some uncertainty due to erosion on these soft, flat surfaces. It still, however, serves as a proxy of the offset. Dip could often not be recorded in horizontal outcrops, so strike measurements presented in rose-diagrams.

4.4.2 Sources of errors during data processing

There are uncertainties when using photographs from the field. The outcrops are never completely horizontal or vertical and the camera lens has some distortion. This leads to some uncertainty of the branch length, in addition to some difficulties when merging the photographs. The photographs will also often be stretched when adding control-points when the photograph is geo-referenced in ArcGIS. This distortion is, however, less than if a photograph that is not stretched, especially when documenting high vertical outcrops without the possibility to get higher up in the terrane, then the total trace length would not be to scale.

Resolution is the main source of error when drawing the nodes and branches in ArcGIS. The uncertainties are relatively low in map view, but larger for localities in cross-section. The uncertainty for localities in map view is highly reduced by drawing on the fractures, making the topology clear within the damage zone. The splay faults in cross section are in

general larger-scale and have lower accessibility than localities in map view. This may result in lower resolution in the topology analysis for these localities. The lower resolution may result in fewer X-nodes, as X-nodes are often found in small-scale fractures in the localities in map view. This could result in a lower apparent connectivity.

There is some deviation between the calculated number of faces (formula 3-5, Section 4.1.2) and the actual number of faces. This is due to the assumption of only one cluster in the sample area, which is most often the case when sampling along a fault in a fault damage zone. In some cases, however, the fracture network will form two or more clusters within the circle sample, causing some deviation from the formula. Based on this, a test was done on the locality K1 (Fig. AII.2 in Appendix II) to quantify this deviation (Fig. 4.5). The plot (Fig. 4.5) shows that there is some deviation between the counted and calculated faces. The trends are similar and the deviation is very small, especially where there are a high number of faces. It is therefore assumed that the deviation between calculated and counted number of faces are negligible. The calculated number of faces is therefore good approximation of the number of 2D blocks in a sample area, and it is way more efficient to calculate this number based on the topology, than counts of the number of faces.

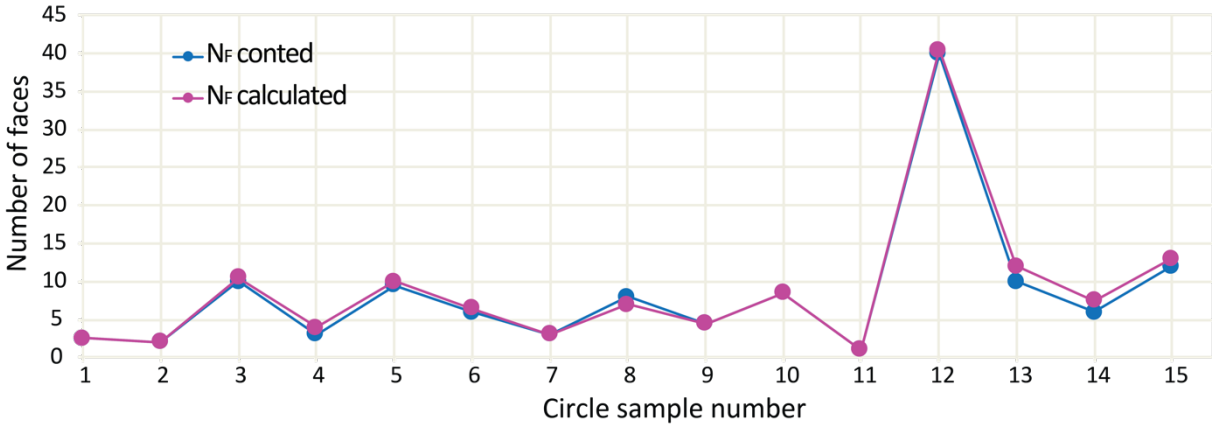

Figure 4.5: Plot showing the deviation between the calculated number of faces ($N_F = 1 - (N_N - N_{II} \times 2) + N_{IC} + N_{CC}$, formula 3-5, Section 4.1.2) and the counted number of faces in circle samples taken along strike of the locality K1 (Fig. AII.2 in Appendix II). The plot indicates that the deviation is negligible, especially at high number of faces.

5 Results

A total of 18 normal fault damage zones are studied and documented. They include six fault tip damage zones, three splay fault damage zones and nine relay damage zones. The local stratigraphic and structural framework of the field area are briefly summarised (Section 5.1). Secondly, the topology, fracture intensity and connecting node frequency for all damage zones are presented (Section 5.2 and Fold-out figures 1 and 2 in Appendix II). The characteristic topology of the three types of damage zones are addressed (Section 5.3, 5.4 and 5.5). Finally, variations within one damage zone are presented by the use of along-strike and along-dip circle samples of the three different damage zone types (Section 5.6 and Figs. AII.1-AII.18 in Appendix II). This chapter focusses on quantifying the topology with special attention to the fracture intensity, connecting node frequency in addition to triangular node- and branch plots of each damage zone.

5.1 Structures and stratigraphy of the field area

5.1.1 Structural framework of the study area

Ras ir Raheb, the study area, is located south of the Victoria Lines Fault, on the west coast of Malta (e.g. Murray, 1890; Dart et al., 1993; Michie et al., 2014) (Fig. 5.1). There are three major faults in the study area, they show displacement of 25.0, 7.0 and 5.1 metres and are all trending ENE - WSW (Michie et al., 2014). Additionally, minor normal faults are exposed in the study area, which show offsets ranging from 0.01 m to 1.50 m. Most of the minor faults trend ENE-WSW and ESE-WNW with a few of them trending NW-SE, dips are ranging from 40° to 86° (Fig. 5.2). Most of the small-scale normal faults are steeply dipping, showing a planar geometry with narrow damage zones (a few cm). Wider damage zones occur where faults are vertically or laterally segmented, thus resulting in several slip planes in one fault array. These local variations are typical around fault bends, fault tips, splay faults and relay zones. The three latter are closely studied and presented in the following sections. An overview of faults and localities are given in figure 5.1.

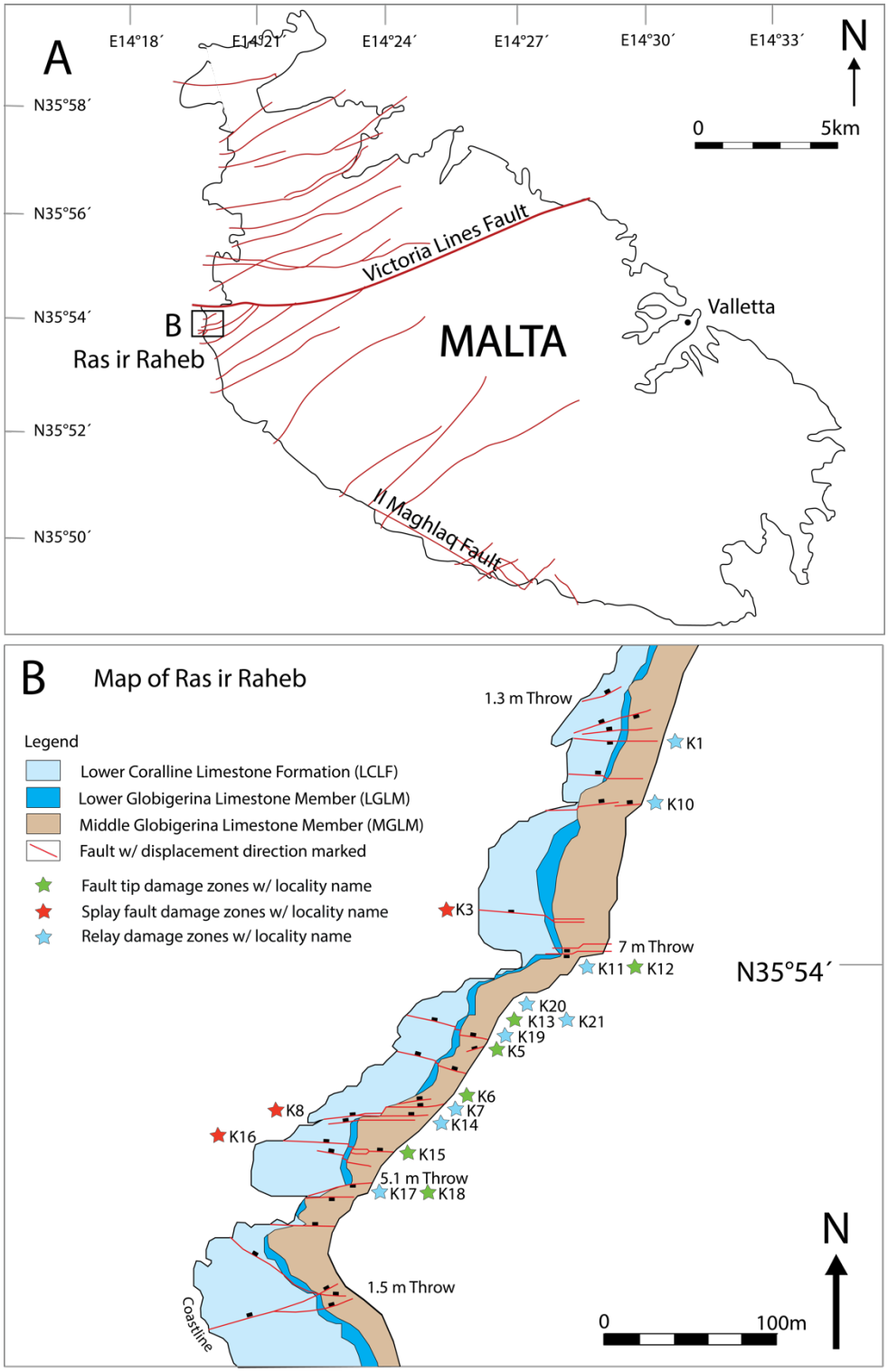

Figure 5.1: A) Structural map of Malta, indicating location of the study area, Ras ir Raheb. B) Mapped normal faults at Ras ir Raheb. The map only include fault with throw over 0.1 m, faults exhibiting throw over 1 m is written in figure. Locations of studied localities are marked with stars indicating damage zone type. Note that localities often include a normal fault with throw below 0.1 m, and will therefore not always belong to a mapped fault in the figure. Figure modified from Michie et al. (2014). Splay damage zones are studied in vertical outcrops of LGLM and MGLM. Fault tip damage zones and relay damage zones are studied in pavement outcrops of MGLM.

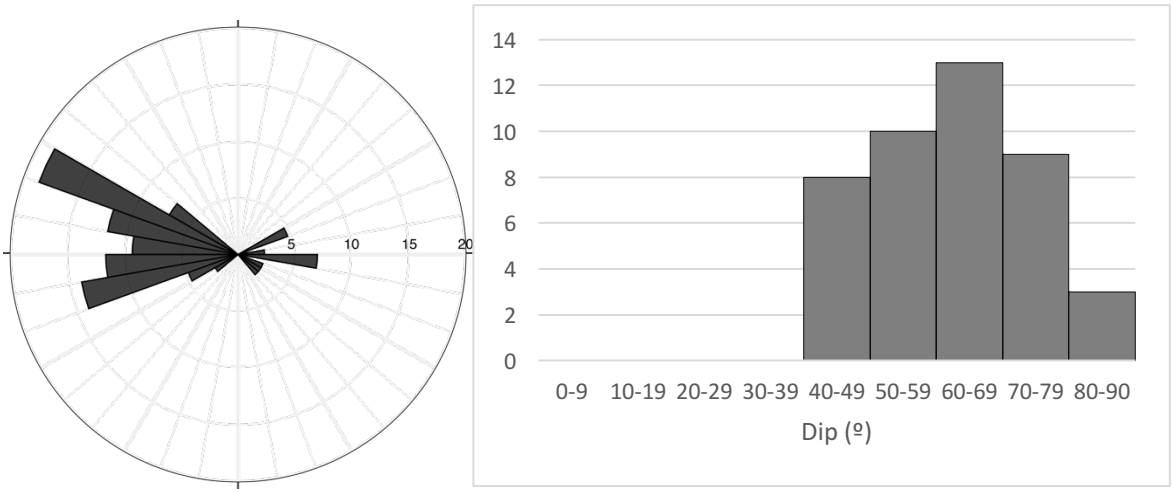

Figure 5.2: Rose diagram (left) representing the strikes of faults with throws between 0.1 and 1 metre in Ras ir Raheb, two measurements of each fault are included in the rose diagram. Note that the strikes are not length-weighted. Histogram (right) represents the distribution of measured fault dips.

5.1.2 Stratigraphy of the study area

At Ras ir Raheb, the Lower Coralline Limestone Formation (LCLF) and the Globigerina Limestone Formation (GLF) are exposed. More specifically the Lower Globigerina Limestone Member (LGLM) and the Middle Globigerina Limestone Member (MGLM) of the GLF is the focus for structural analysis. The local lithology is presented in a stratigraphic column in figure 5.3. It includes packstones, wackestones and mudstones, which is subdivided into 11 informal units briefly summarised below. Note that studied splay fault damage zones are exposed in vertical outcrops which includes LGLM, LGLM-C1 and MGLM-1. Relay damage zones and fault tip damage zones are exposed in pavement outcrops between MGLM-C2A and MGLM-C2B (Fig. 5.3).

Lower Coralline Limestone Formation (LCLF)

The exposed section (LCL-1 to LCL-4) of LCLF is dominated by packstones and a thinner interval of wackestone (Fig. 5.3). LCL-1 and LCL-4 comprise of packstones and macrofossils of bryozoans, solitary corals, echinoids and bivalves are observed. The LCL-2 shows a higher mud content and is therefore characterised as a wackestone. Observed macrofossils include algae and bryozoans. The overlying LCL-3 is a packstone characterised by an irregular and erosional base and macrofossils of algae and gastropods. Limiting the LCL-4 is the characteristic hardground surface, which is caused by biochemical and chemical alternations during non-depositional periods where

sediments were just under or below the sea-level at the time (e.g. Felix, 1973; Bennett, 1979; Dart et al., 1993).

Lower Globigerina Limestone Member (LGLM)

The LGLM unit is a wackestone which includes macrofossils of bivalves, bryozoans and burrows (Fig. 5.3). It is light yellow in colour, are weakly bedded and easily eroded. A distinct phosphorite conglomerate (LGLM-C1) marks the top of LGLM. LGLM-C1 is characterised by its dark brown colour and an increase in macrofossils, including bryozoans, solitary corals, bivalves and shark teeth. LGLM-C1 is approximately 50 cm thick, clast supported, polymodal and show inverse grading. The clasts are sub rounded to rounded and up to 20 cm in diameter in the upper part. The base is irregular and shows deep burrows infilled with phosphoritic 0.1-1 cm clasts.

Middle Globigerina Limestone Member (MGLM)

MGLM is characterised by its light yellow colour and are highly bioturbated mudstones. MGLM-1 is biomicritic mudstones, showing burrows where some include small phosphorite clast infill. Macrofossils of shark teeth is also observed. The clean mudstones are disrupted by an irregular phosphoritic conglomerate horizon, MGLM-C2A (Fig.5.3). MGLM-C2A is ~ 50 cm thick, highly matrix supported and bimodal. The clasts are sub rounded to rounded, 0.2-3 cm in diameter showing and average size of 0.5 cm. The base show ~ 30% of clast and the top ~10% giving it a normal graded appearance. High amounts of macrofossils are observed and include bryozoans, solitary corals, bivalves and shark teeth. Overlying the MGLM-C2A is the second interval of clean light yellow mudstones, MGLM-2. This unit include bioturbation and are massively bedded like MGLM-1. The older MGLM-C2B is ~ 90 cm thick and has a similar character as the MGLM-C2A, except it has clasts up to 8 cm in diameter with an average size of 1 cm. Macrofossils in the unit include bioturbation, echinoids, bivalves, bryozoans, solitary corals and shark teeth. The uppermost unit MGLM-3 is a thick (~ 22m) third section of light yellow biomicrites and it includes chert nodules, bioturbation and macrofossils of gastropods and bivalves (Fig. 5.3).

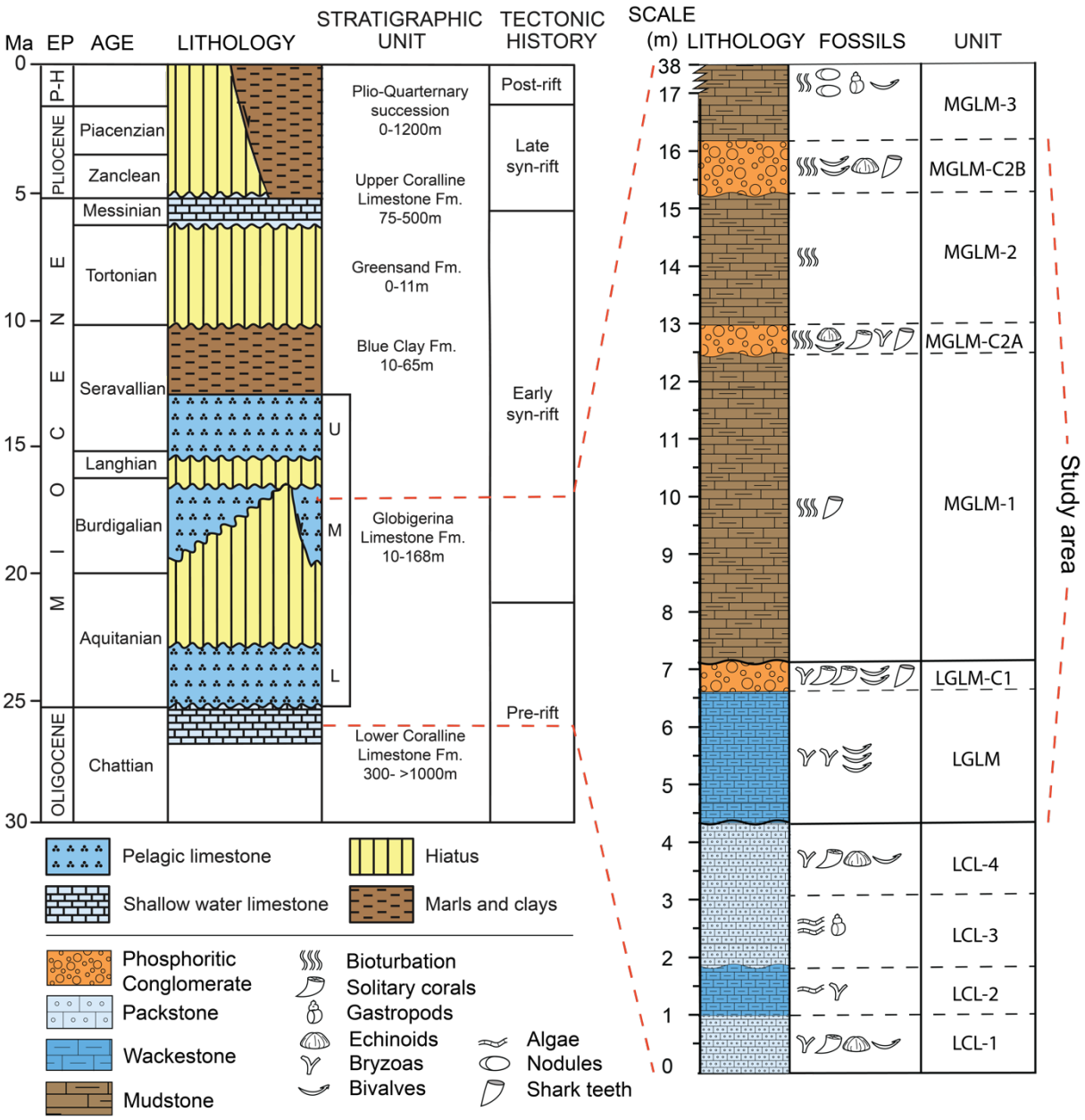

Figure 5.3: Stratigraphic column from Dart et al. (1993) to the left. It includes the age of all documented lithologies, its stratigraphic name and thickness variations of the formations. At last, it includes the tectonic history of the Maltese region. Studied formations include the pre-rift and early syn-rift deposits. Local stratigraphy of Ras ir Raheb is shown in a stratigraphic column to the right. The column includes the lithology, macrofossils observed and informal unit names. Note that studied splay fault damage zones are exposed in vertical outcrops, which includes LGLM, LGLM-C1 and MGLM-1. Relay damage zones and fault tip damage zones are studied in pavement outcrops between MGLM-C2A and MGLM-C2B.

5.2 Geometry and topology of the studied damage zones

The topology of the 18 studied damage zones has been analysed and used to calculate fracture intensity and connecting node frequency (see A3 overview in Fold-out figure 1 and 2 in Appendix II). The damage zones are grouped into six fault tip damage zones, three splay fault damage zones and nine relay damage zones, based on their geometry (Table 2). A fault tip damage zone displays a wedge-shaped geometry where a fault is tipping out laterally and may include one or several main fault segments tipping out in the same direction (e.g. Scholz and Anders, 1994; Kim et al., 2004). Splay fault damage zones comprise of a normal fault segment(s) with footwall- or hangingwall splay fault(s), forming a cone-shaped geometry (e.g. McGrath and Davison, 1995; Perrin et al., 2016). Relay damage zones occur along two similarly dipping normal faults that overlap and/or link in map view, as a relay ramp is born to it is breached (stage 1 to 4) (e.g. Peacock and Sanderson, 1991, 1994; Fossen and Rotevatn, 2016). Damage zones are arranged from those with high proportions of I-nodes to those with low proportions of I-nodes in the figures (Fold-out figure 1 and 2 in Appendix II).

Table 2: Damage zone types and locality names

Damage zone type	Locality names
Fault tip damage zones	K5, K6, K12, K13, K15, K18
Splay fault damage zones	K3, K8, K16
Relay damage zones	K1, K7, K10, K11, K14, K17, K19, K20, K21

The node plot (Fig. 5.4a and Fold-out figure 1) shows that all of the damage zones are dominated by I- or Y-nodes. K1, which is a stage 4 relay damage zone, has the lowest proportion of I-nodes (12.4%) and thus exhibits the highest proportion of connecting nodes. The maximum proportions of X-nodes are documented in the stage 4 relay damage zones K7 and K19, with 10.7 % and 10.3 % of X-nodes respectively. In contrast, K13 is a fault tip damage zone (Fig. 5.4a) and has the highest proportion of I-nodes (89.5 %). Average connections per branch (C_B), i.e. the connectivity, of the studied damage zones range from 0.52 (K13) to 1.91 (K1), which is indicated in the node plot (Fig. 5.4a). Generally, low connectivity (below 1.60 C_B) are recorded in fault tip damage zones and stage 2 relay damage zones, high connectivity (over 1.80 C_B) are recorded in stage 4 relay

damage zones. In the node plot (Fig. 5.4), there is an overlap between the three types of damage zones close to the I-Y axis, between 1.20 and 1.80 C_B. Relay damage zones overlap with both fault tip damage zones and splay fault damage zones in the node- and branch-plots. However, fault tip damages zones and splay fault damage zones do not overlap in the plots. Splay fault damage zones show the lowest variability and are the most clustered damage zone type in the plots (Fig. 5.4). The general trend is that relay damage zones display the highest connectivity, splay fault damage zones display medium connectivity and fault tip damage zones show the lowest connectivity (Fig. 5.4).

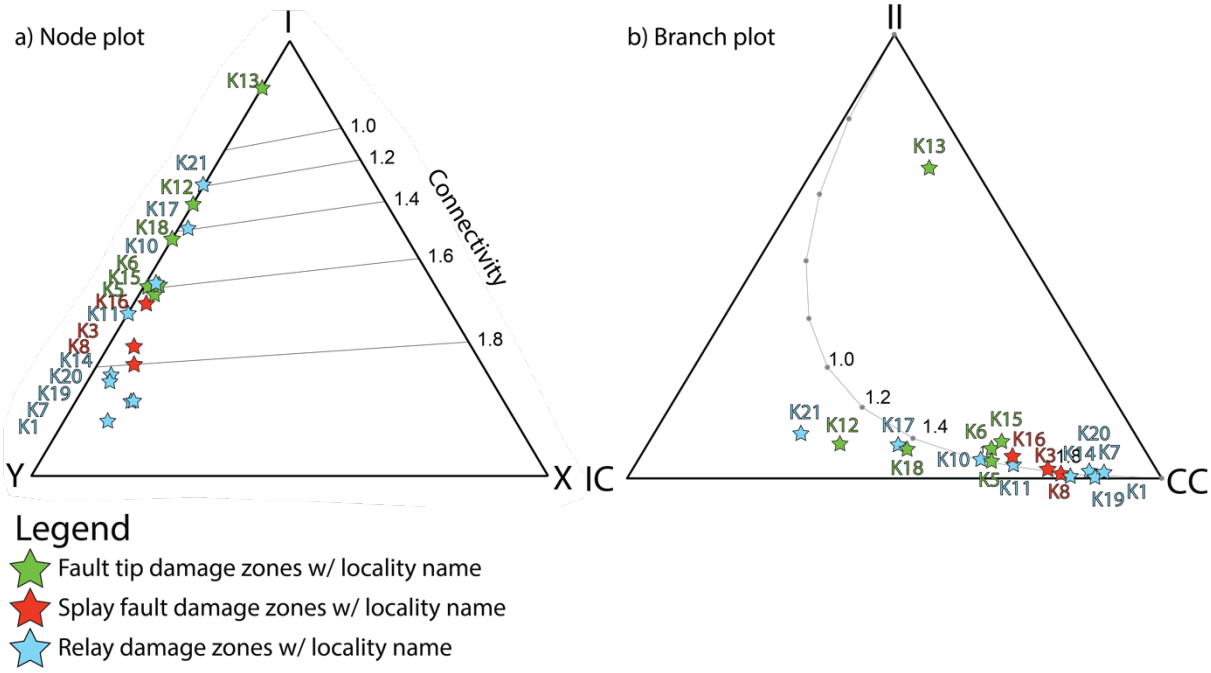

Figure 5.4: a) Node plot: percentages of I-, Y- and X-nodes mapped for each damage zone studied, presented in a triangular node plot. The colour of the stars represents the damage zone type and the locality name is marked in the figure. b) Branch plot: percentages of II-, IC- and CC-branches mapped for each damage zone studied. The damage zone type is indicated by the colour of the stars and the locality name is included. Together, figures (a) and (b) represent the overall topology of all the damage zones studied and both plots indicate the connectivity of the localities.

5.2.1 Fracture intensities

Fracture intensities for all 18 damage zones are presented in Fold-out figure 1 in Appendix II. The fracture intensity maps have been generated in ArcGIS (Section 4.3). The intensity ranges from 10 m^{-1} to 210 m^{-1}. Most of the damage zones show fracture intensities under 100 m^{-1}, with the exception of six localities; K1, K7, K19, K20, K8 and

K3 represented by stage 3 and 4 relay damage zones and splay fault damage zones (Fold-out figure 1 in Appendix II). The higher values are located in linkage areas of the relay zones and in splay areas of the splay faults, which are areas of localised deformation and higher fracture intensities. The maximum fracture intensity of 210 m^{-1} is located in the splay zone of K3, followed by K7 and K8 with a maximum of 166 m^{-1} and of 164 m^{-1}, respectively.

5.2.2 Connecting node frequencies

Connecting node frequencies for all 18 damage zones are presented in Fold-out figure 2 in Appendix II. The maps were made in ArcGIS (Section 4.3). Connecting node frequencies range from 0 m^{-2} to 16000 m^{-2}. Fault tip damage zones do not exhibit connecting node frequencies greater than 4000 m^{-2} (K5) (Fold-out figure 2 in Appendix II). Higher connecting node frequency values are restricted to areas of local complexity within relay damage zones and fault splay damage zones, similar to higher values of the fracture intensity maps. The maximum connecting node frequency is recorded in the splay point of K3 and in the linkage area of K7.

5.3 Geometry and topology of fault tip damage zones

The studied fault tip damage zones are most commonly dominated by horsetail fractures, although en-echelon fractures are observed (Figs. 5.5 and 5.6) (sensu McGrath and Davison, 1995). Fracture intensities for fault tip damage zones range from 10 m^{-1} to 120 m^{-1} (Fig. 5.5). The fault tip damage zones with no X-nodes (K13, K12 and K18) do not exhibit fracture intensities in excess of 80 m^{-1} (Fig. 5.5c, d, e). The higher values are associated with areas around bifurcation points, where a segment bifurcates into two or more segments towards the fault tip. The maximum fracture intensity for individual fault tip damage zones generally increases with increasing proportions of connecting nodes within the damage zone, indicated by red arrows (Fig. 5.5). The connecting node intensities range from 0 m^{-2} to 5010 m^{-2} (Fig. 5.6). The fault tip damage zones with no X-nodes (K13, K12 and K18) do not exceed connecting node frequencies of 1500 m^{-2} (Fig. 5.6c, d, e). The higher values are restricted (as the fracture intensities) to area around bifurcation points towards the fault tip.

The six fault tip damage zones (Fig. 5.6) have connectivity ranging from 0.52 to 1.62 C_B, so they show a spread in both the node- and the branch-plots (Figs. 5.5a, b and 5.6a, b). Arrows in triangular plots indicate increasing connectivity of the fault tip damage zones (Figs. 5.5a, b and 5.6a, b). All fault tip damage zones display a low proportion of X-nodes, with a recorded maximum of 2.9 % in K5, which also has the highest proportion of Y-nodes at 55.2 % (Figs. 5.5a, b, h and 5.6a, b, h). There are no X-nodes recorded for fault tip damage zones with connectivity less than 1.43 C_B (K13, K12 and K18). The fault tip damage zones show a greater spread in the branch plot than in the node plot. This is mostly due to K13, which has 69.6 % of II-branches, whilst the others have between 4.2 % and 7.9 % of II-branches.

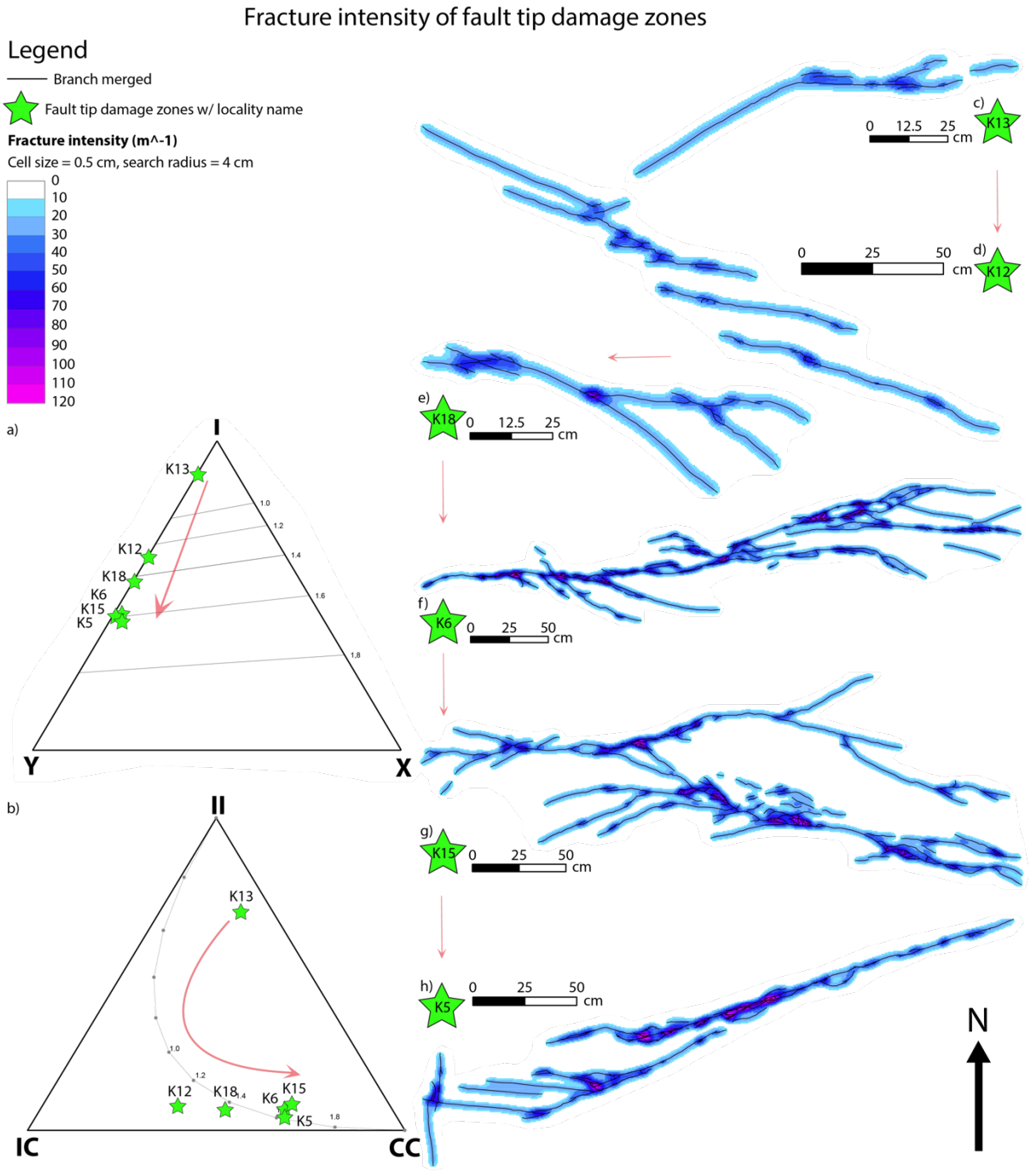

Figure 5.5: Fracture intensity maps of fault tip damage zones. The documented fault tip damage zones are all exposed in the MGLM. a) Node plot of the mapped fault tip damage zones with associated locality name. The red arrow indicates increasing percentages of connecting nodes (Y- and X-nodes) and increasing connectivity. b) Branch plot of the mapped fault tip damage zones with associated locality name. The red arrow indicates increasing percentages of connecting branches (IC and CC) and increasing connectivity. c) to h) Maps of fault tip damage zones, arranged according to arrows in the triangular plots (a and b), which implies increasing amounts of connecting nodes and increasing connectivity downward in the figure (c to h). Note that the overall fracture intensity generally increases with increasing percentages of connecting nodes (Y- and X-nodes).

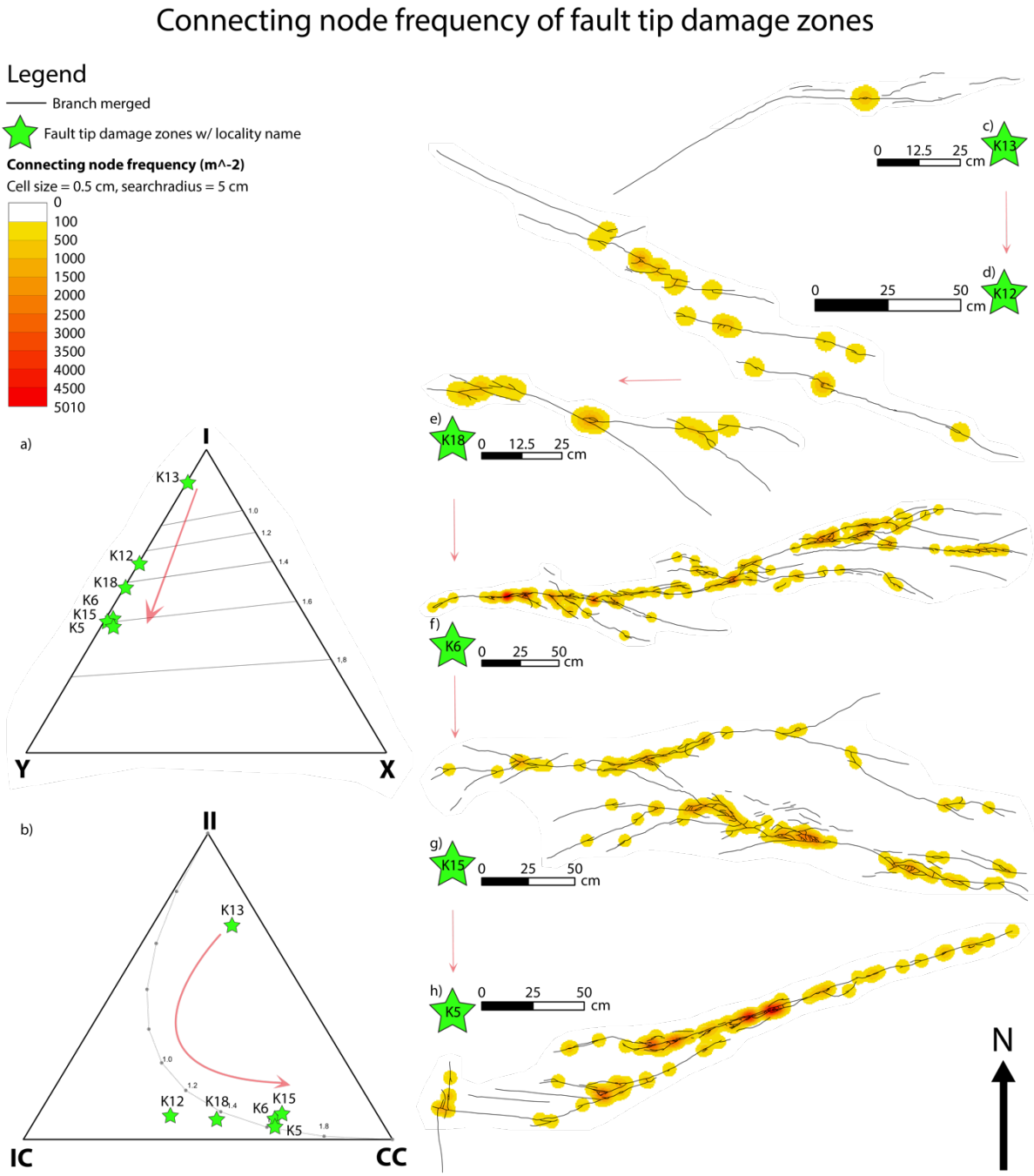

Figure 5.6: Connecting node frequency maps of fault tip damage zones. The documented fault tip damage zones are all exposed in the MGLM. a) Node plot of the mapped fault tip damage zones with associated locality name. The red arrow indicates increasing percentages of connecting nodes (Y- and X-nodes) and increasing connectivity. b) Branch plot of the mapped fault tip damage zones with associated locality name. The red arrow indicates increasing percentages of connecting branches (IC and CC) and increasing connectivity. c) to h) Maps of fault tip damage zones, arranged according to arrows in the triangular plots (a and b), which implies increasing amounts of connecting nodes and increasing connectivity downward in the figure (c to h). Note that the overall connecting node frequency generally increases with increasing percentages of connecting nodes (Y- and X-nodes).

5.4 Geometry and topology of splay fault damage zones

The splay fault damage zones show fracture intensities ranging from 10 m^{-1} to 180 m^{-1} (Fig. 5.7). K16 has the lowest fracture intensity recorded for the splay faults and has a greater proportion of I-nodes relative to K3 and K8 (Fig. 5.7). The maximum fracture intensity is recorded in the splay zone and the lens of K3 (Fig. 5.7b). Note that K8 has the greatest overall connectivity recorded in both the node- and the branch-plots, but does not have the highest local fracture intensity (Fig. 5.7c, d, e). Fracture intensities are generally less than 100 m^{-1}, with higher values restricted to lenses and the splay zones of K3 and K8. The connecting node frequency for splay fault damage zones range from 0 m^{-2} to 10500 m^{-2} (Fig. 5.8). Again the maximum values are recorded in the splay and the lens of K3, even though K8 has the greatest connectivity of both the node- and branch plots (Fig. 5.8). The connecting node frequency generally stays below 2000 m^{-2}, with the higher values being restricted to lenses and splay zones of K16, K3 and K8.

The three splay fault damage zones have connectivity ranging from 1.64 to 1.80 C_B, hence they show a low variability in connectivity (Figs. 5.7d, e and 5.8d, e). The lowest C_B of 1.64 is recorded in K16, the medial C_B of 1.76 is recorded in K3 and the highest C_B of 1.80 is shown in K8. Splay fault damage zones are clustered in both the node and the branch plots, reflecting a low variability in topology (Figs. 5.7d, e and 5.8d, e). The node plot shows that splay fault damage zones have large proportions of connecting nodes, ranging from 60.2% to 74.2% (Figs. 5.7d and 5.8d). There are very few isolated branches (1.1 % to 5.2%), with the majority of the branches being either partly connected (18.1% - 25.3%) or fully connected (69.5% - 80.7%) (Figs. 5.7e and 5.8e).

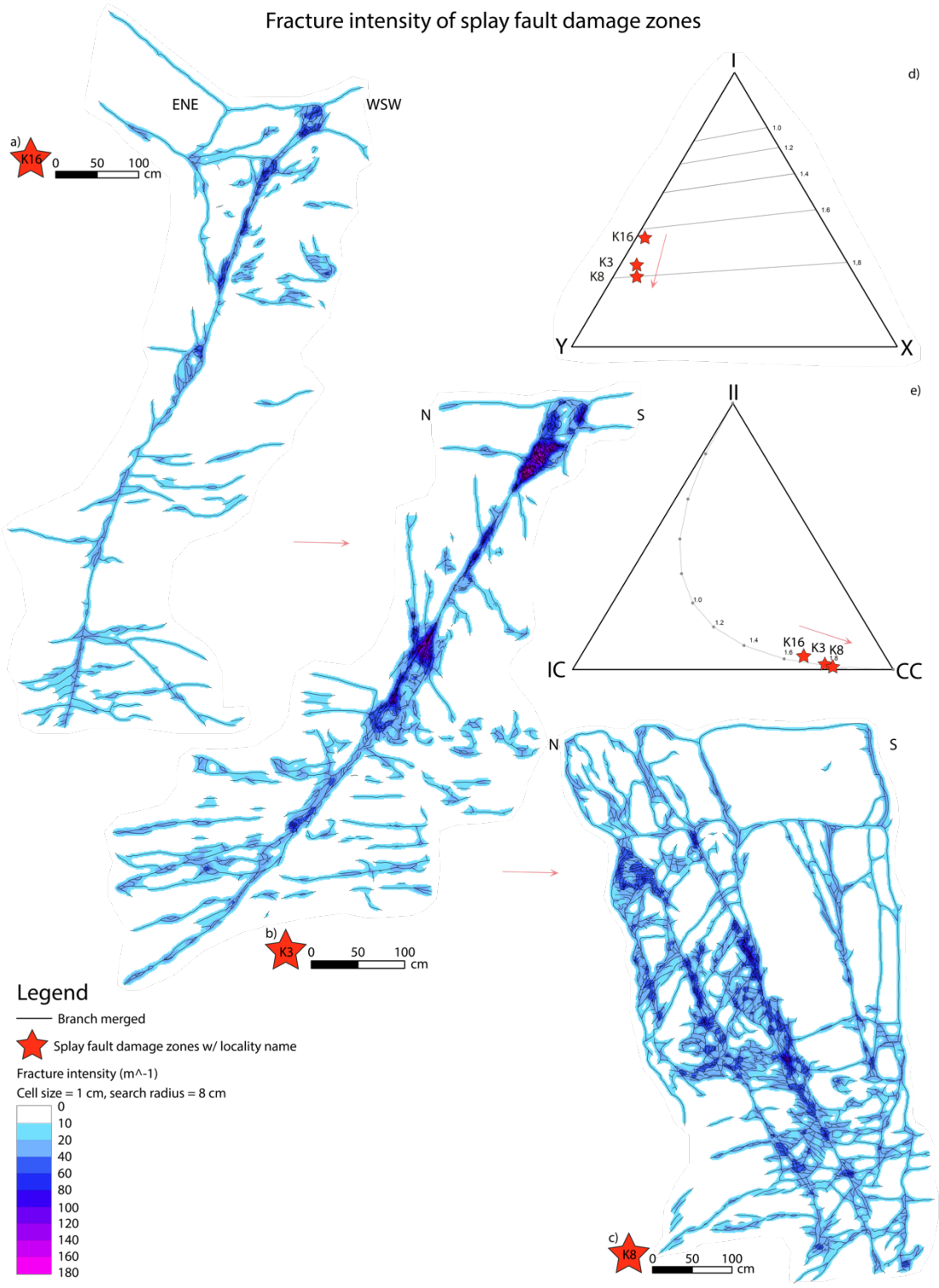

Figure 5.7: a) to c) Fracture intensity maps of splay fault damage zones. These splay fault damage zones are all exposed in vertical outcrops of the LGLM and MGLM. The splay fault damage zones (a to c) are arranged according to arrows in the triangular plots (d and e), which implies increasing amounts of connecting nodes and increased connectivity from K16 to K3 and K8 (a to c). The overall fracture intensity increases with increasing percentages of connecting nodes (Y- and X-nodes). d) Node plot of the mapped node within splay fault damage zones with associated locality name. The red arrow indicates increasing percentages of connecting nodes (Y- and X-nodes) and increasing connectivity. e) Branch plot of the mapped branches of

splay fault damage zones with associated locality name. The red arrow indicates increasing percentages of connecting branches (IC and CC) and increasing connectivity.

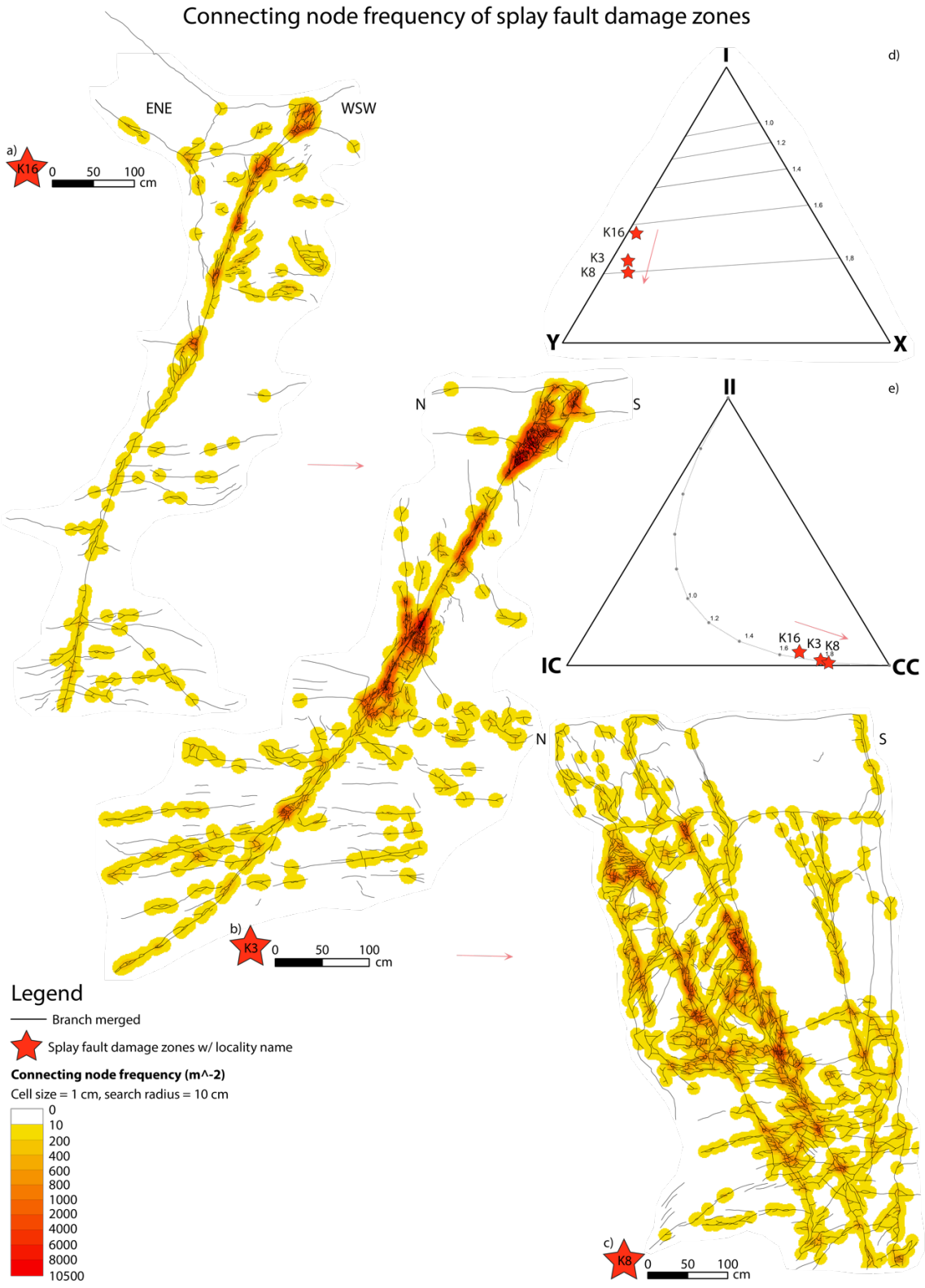

Figure 5.8: a) to c) Connecting node frequency maps of splay fault damage zones. These splay fault damage zones are all exposed in vertical outcrops of the LGLM and MGLM. The splay fault damage zones (a to c) are

arranged according to arrows in the triangular plots (d and e), which implies increasing amounts of connecting nodes and increasing connectivity from K16 to K3 and K8 (a to c). Note that the overall connective node frequency generally increases with increasing percentages of connecting nodes (Y- and X-nodes), although the local connecting node frequency varies. d) Node plot of the mapped nodes within splay fault damage zones with associated locality name. The red arrow indicates increasing percentages of connecting nodes (Y and X) and increasing connectivity. e) Branch plot of the mapped branches within the splay fault damage zones with associated locality name. The red arrow indicates increasing percentages of connecting branches (IC and CC) and increasing connectivity.

5.5 Geometry and topology of relay damage zones

The relay damage zones show fracture intensities ranging from 10 m^{-1} to 200 m^{-1} (Fig. 5.9). Stage 2 relay damage zones have fracture intensities below 80 m^{-1}, with the exception within K10, east of the soft linked area (Fig 5.9c, d, e). Stage 3 relay damage zones have fracture intensities up to 140 m^{-1} (Fig. 5.9f, g, h) and stage 4 relay zones include the highest values (Fig. 5.9i, j, k). The maximum value (200 m^{-1}) is located in K7, and K1 reaches 183 m^{-1}. K7 has larger areas with high intensities (Fig. 5.9a, b). K7 and K19 also have similar topologies but differences in their local fracture intensities. Fracture intensities are generally less than 80 m^{-1}, with greater intensities restricted to linkage areas and smaller relays within the larger relay localities.

The connecting node frequencies range from 0 m^{-2} to 12000 m^{-2} (Fig. 5.10). Stage 2 relays have the lowest connecting node frequencies, less than 1000 m^{-2}, with the exception of K10 east of the soft linked area (Fig. 5.10c, d, e). Stage 3 relay zones have connecting node frequencies under 5000 m^{-2} (Fig. 5.10f, g, h). The most connected relays are represented by stage 4 relay damage zones, which have connecting node frequencies up to 12 000 m^{-2} (Fig. 5.10i, j, k). Frequencies are generally less than 3000 m^{-2}, with the higher values restricted to linkage areas and smaller relays within the larger relay localities. As mentioned, K19 and K7 have similar to identical topology, but show large differences in their local connecting node frequencies (Fig. 5.10a, b).

The nine relay damage zones have connectivity ranging from 1.20 to 1.91 C_B, giving the plotted localities a spread in both the node- and the branch-plots (Figs. 5.9a, b and 5.10a, b). The minimum conectivity is recorded in K21 and the maximum in K1. Node plots show

that some of the relay damage zones are dominated by I-nodes and some by Y-nodes, where the ones dominated by I-nodes represent stage 2 relay damage zones and the ones dominated by Y-nodes represents stage 3 and 4 relay damage zones (Figs. 5.9a and 5.10a). The localities consist of 33.3 % to 87.6 % of connecting nodes. Note that the relays with the lowest connectivity (K21, K17, K10 and K11) contains 0 % to 1.8 % of X-nodes, while the more connecting relays (K14, K20, K19, K7 and K1) contain 3.7 % to 10.7 % of X-nodes. The branch plot shows a domination of IC- and CC-branches with 0 % (K1 and K19) to 10.0 % (K21) of II-branches (Figs. 5.9b and 5.10b). The connected relays show 82.5 % (K14) to 91.2 % (K1) of CC-branches, while the less connected relays contain 27.5 % (K21) to 70.8 % (K11) of CC-branches. The connectivity of relay damage zones shows that stage 2 relays exhibit low connectivity, stage 3 relays exhibit medium connectivity and stage 4 relays show high connectivity (Fig. 5.9a, b). The gradual increase in connectivity is also reflected in their geometry, where the stage 3 and 4 relay damage zones show a connected or linking geometry, resulting in high proportions of CC-branches and therefore higher connectivity. Stage 2 relay damage zones, on the other hand, display a more bifurcating and soft linking geometry, resulting is a higher proportion of IC-branches and therefore lower connectivity (Fig. 5.9a, b).

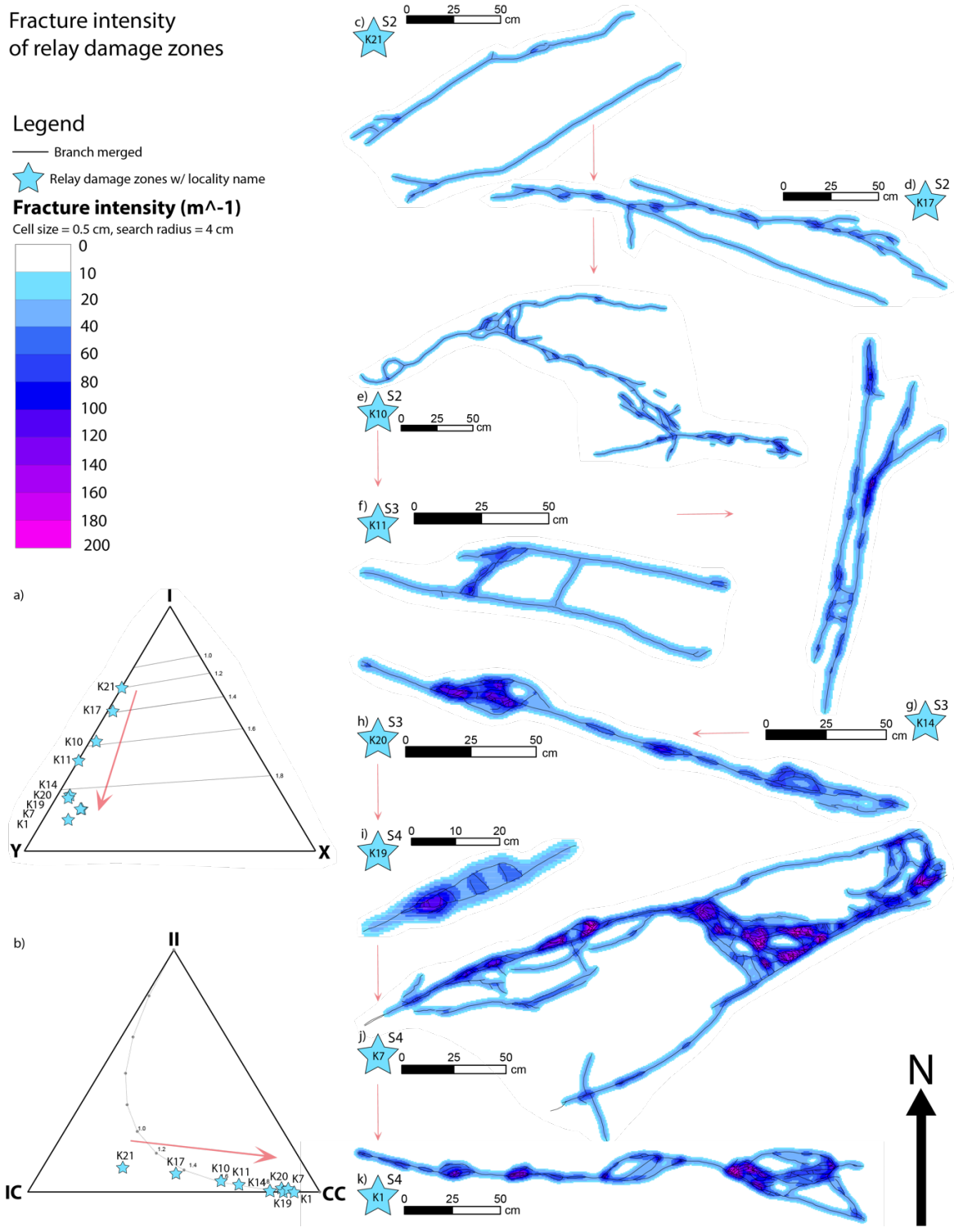

Figure 5.9: Fracture intensity maps of relay damage zones. These relay damage zones are exposed in the MGLM. a) Node plot of the mapped nodes of the relay damage zones with associated locality name. The red arrow indicates increasing percentages of connecting nodes (Y- and X-nodes) and increasing connectivity. b) Branch plot of the mapped branches of relay damage zones with associated locality name. The red arrow indicates increasing percentages of connecting branches (IC and CC) and increasing connectivity. c) to k) Maps of relay damage zones, arranged according to arrows in the triangular plots (a and b), which implies increasing amounts of connecting nodes and increasing connectivity downward in the figure (c to k). The

stages of individual relay structures are indicated by S2 to S4, where S2 = Stage 2 etc. Note that the overall fracture intensity generally increases with increasing percentages of connecting nodes (Y- and X-nodes).

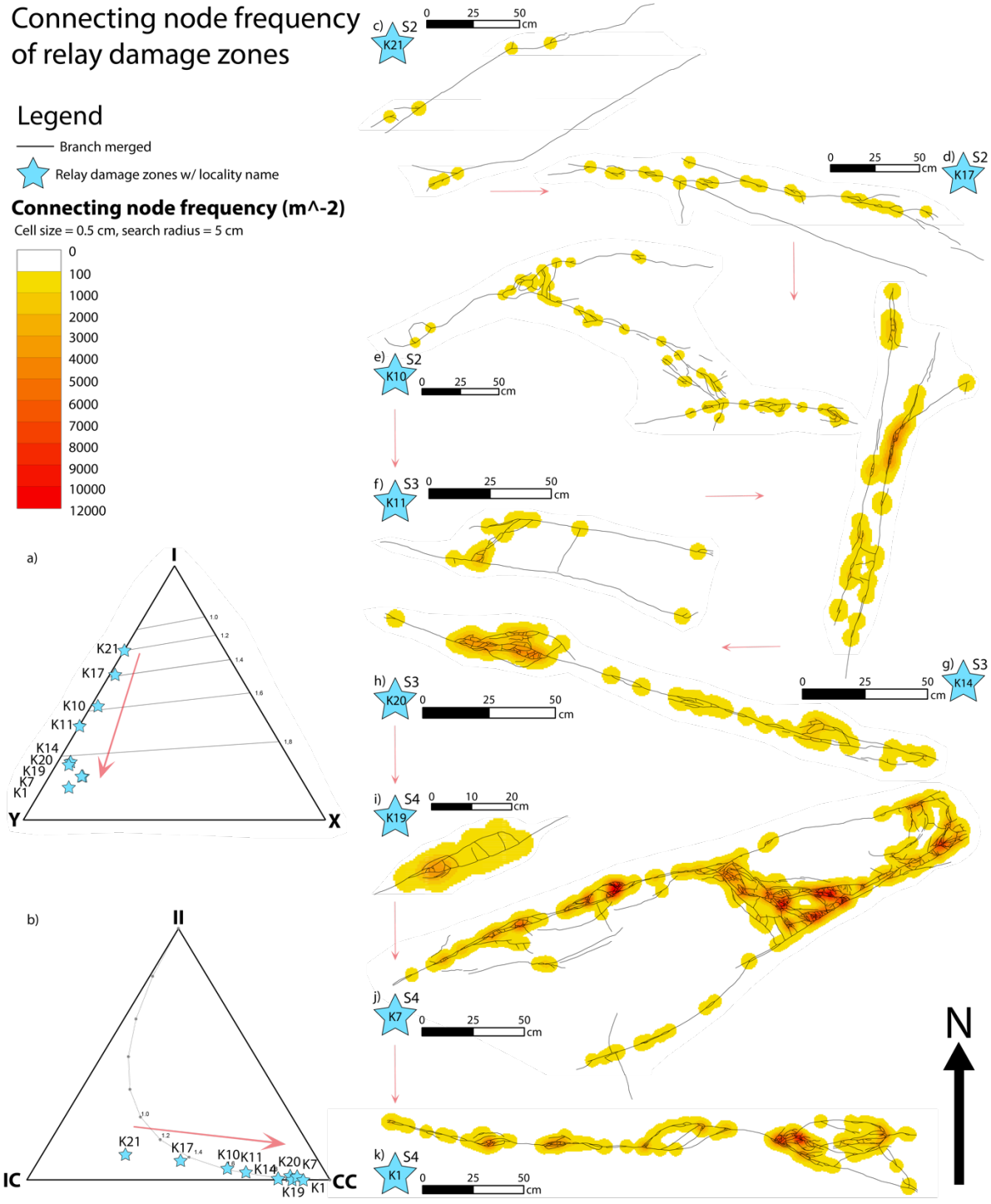

Figure 5.10: Connecting node frequency maps of relay damage zones. The documented relay damage zones are exposed in the MGLM. a) Node plot of the mapped nodes of the relay damage zones with associated locality name. The red arrow indicates increasing percentages of connecting nodes (Y- and X-nodes) and increasing connectivity. b) Branch plot of the mapped branches of relay damage zones with associated

locality name. The red arrow indicates increasing percentages of connecting branches (IC and CC) and increasing connectivity. c) to k) Maps of relay damage zones, arranged according to arrows in the triangular plots (a and b), which implies increasing amounts of connecting nodes and increasing connectivity downward in the figure (c to k). The stages of individual relay structures are indicated by S2 to S4, where S2 = Stage 2 etc. Note that the overall connecting node frequency generally increases with increasing percentages of connecting nodes (Y- and X-nodes).

5.6 Spatial variability within damage zones

This section gives a more detailed overview of the variability within individual damage zones. An example of a damage zone resulting from a fault tip (section 5.6.1), a splay fault (section 5.6.2) and a relay (section 5.6.3) are presented with density maps and circle samples along strike or dip (Figs. 5.11 - 5.16). Density maps for the remaining 15 damage zones are added to Appendix II (Figs. AII.1 – AII.18), where three of them have associated circle sample figures (Figs. AII.2, AII.4 and AII.6).

5.6.1 Fault tip damage zone variability – K5

K5 is a small-scale (max. throw: 1 cm) ENE-striking normal fault exposed in a pavement outcrop within the MGLM (Fig. 5.11). The normal fault tips out towards the WSW, within two main soft linked segments, one segment to the WNW and one to the ESE (Fig. 5.11b, c). The tip is splaying into a set of WNW-directed wing-cracks that form a horsetail geometry, also suggested by the length weighted rose-diagram (Fig. 5.11a). The maximum fracture intensity is 120 m^{-1} (Fig. 5.11d). The fracture intensity generally stays below 60 m^{-1}, and the higher values are restricted to bifurcation points or bifurcation areas in the damage zone (Fig. 5.11d). Bullseyes in the fracture intensity map matches bullseyes in the connecting node frequency map, which shows a maximum value of 5010 m^{-2}, also restricted to areas of bifurcation (Fig. 5.11e).

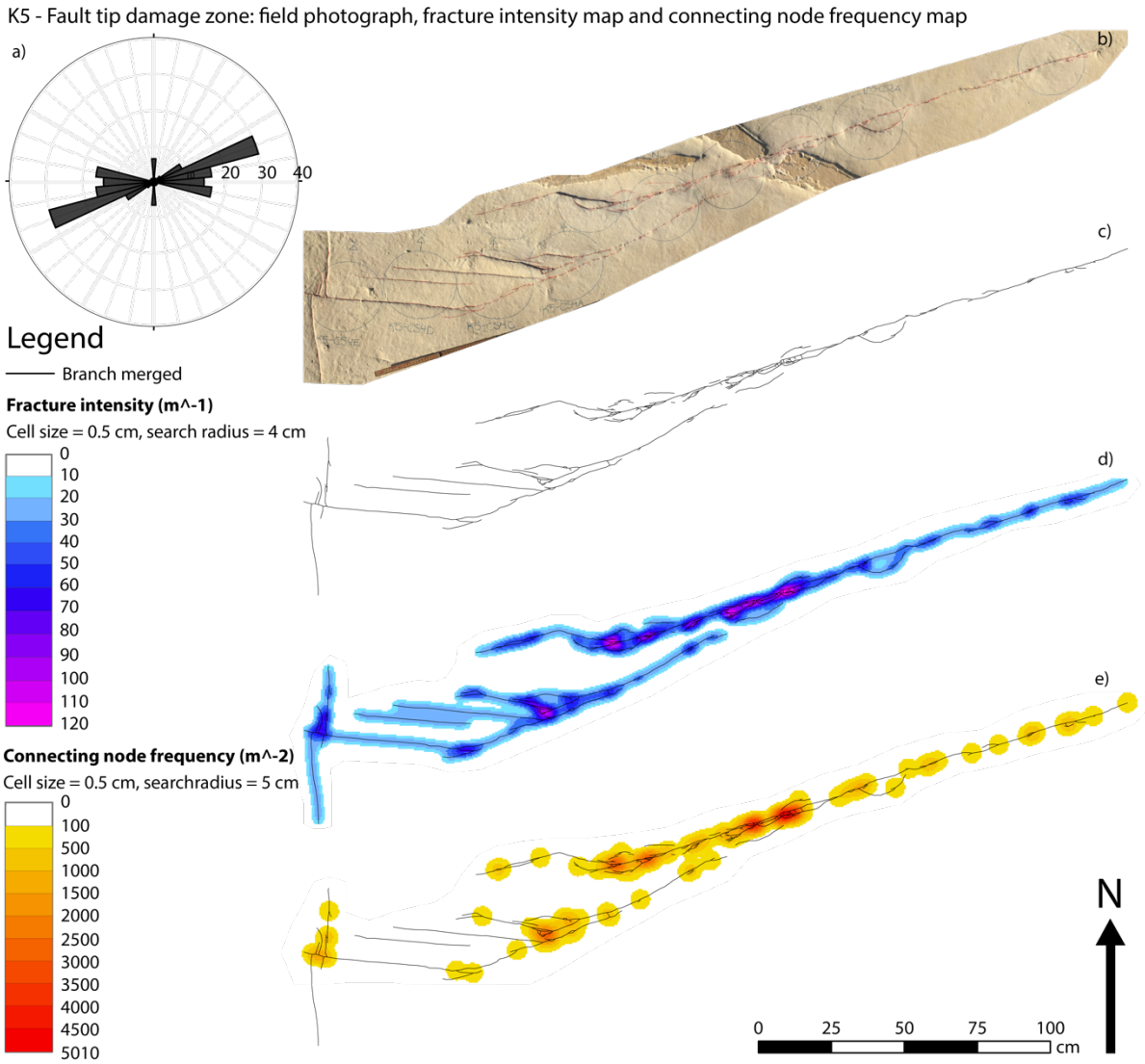

Figure 5.11: K5 is a normal fault tip damage zone tipping out towards the WSW and it is exposed in the MGLM. a) Rose diagram include length-weighted strikes of all branches within the locality. b) Field photograph. c) Associated merged branches. d) Fracture intensity map, created from c). e) Connecting node frequency map, the connecting nodes (Y and X) are used for generating the map.

Along-strike circle samples (CS) (Fig. 5.12a) represent a larger sample area (0.0263 m^2) than the cells of the maps (Fig. 5.11d, e). Hence, they show lower values than both the fracture intensity map and the connecting node frequency map. A total of 16 CS are placed along the strike of K5, with CS 1 to 10 representing the main fault tip damage zone and CS 11 to 16 representing the simpler part of the normal fault damage zone (Fig. 5.12a). The simple normal fault samples shows fracture intensities ranging from 9.0 to 16 m^{-1} (Fig. 5.12c). The fracture intensity of the fault tip damage zone (CS 1 to 10) ranges from 14 m^{-1} (CS2) to 35 m^{-1} (CS5). The higher fracture intensities are located in CS 5 to 10, where the fault bifurcates and transfers strain to the two main segments within the fault tip damage

zone. The higher fracture intensities correspond to the highs in both connecting node frequency and number of faces (Nf) of the CSs (Fig. 5.12c, d, e). Note that variations in values from one sample to another are similar for fracture intensity, connecting node frequency and Nf. In contrast, the maximum value for Nf (10) and connecting node frequency (952 m^{-2}) are located in CS10 rather than in CS5, where the maximum value for fracture intensity is located. Note that CS5 is located immediately after a bifurcation point and therefore has more fractures and longer trace lengths. Thus, a CS may have high fracture intensity but low connecting node frequency.

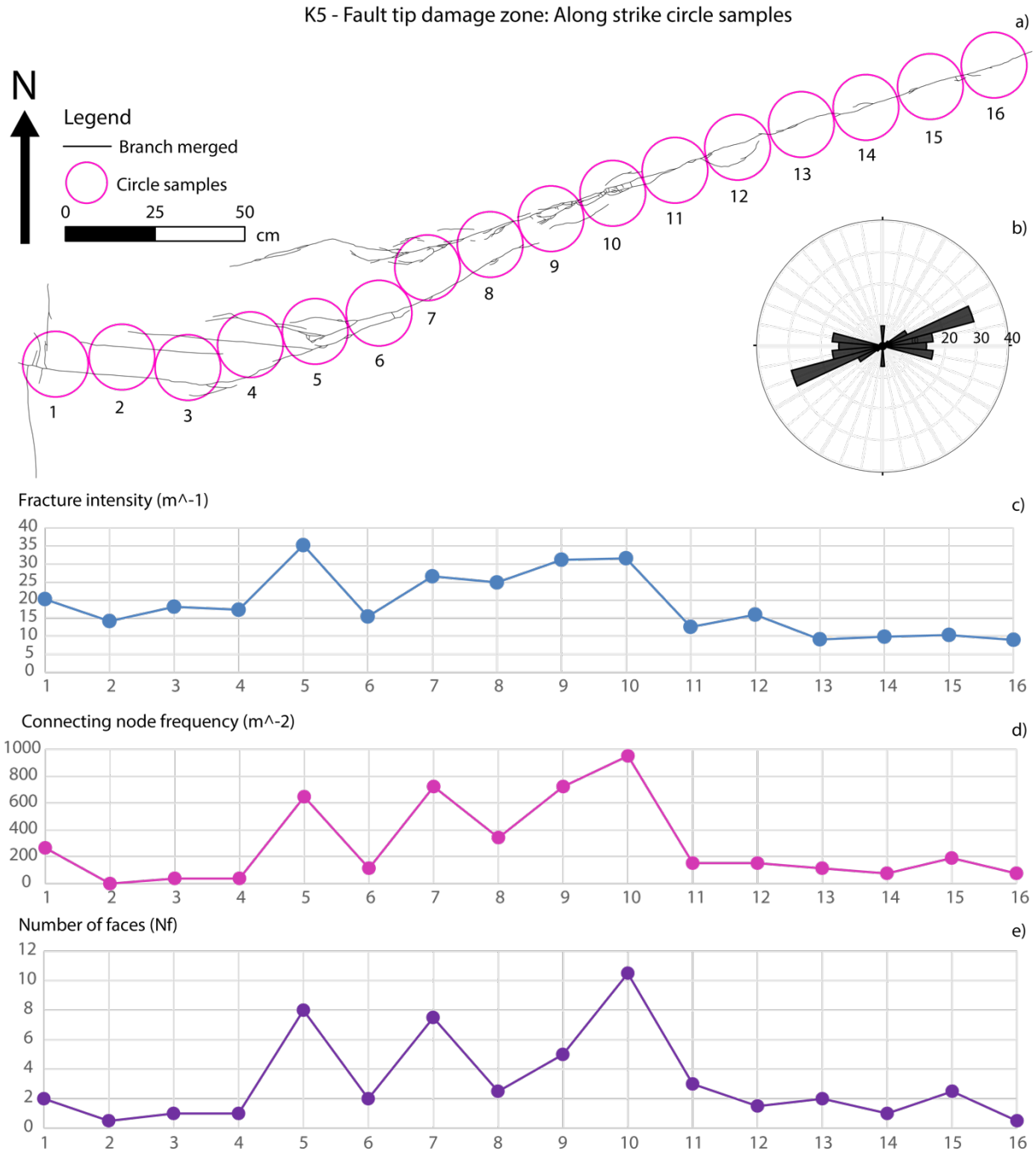

Figure 5.12: a) Mapped branches of K5 with circle samples (0.0263 m^2) along strike of the normal fault. b) Rose diagram presenting the length-weighted strikes of all the branches within the damage zone. c) Graph of fracture intensities (y-axis) of associated circle samples (1 to 16, x-axis). d) Graph of connecting node frequencies (y-axis) of associated circle samples (1 to 16, x-axis). e) Graph of number of faces (y-axis) of the associated circle samples (1 to 16, x-axis).

5.6.2 Relay damage zone variability – K7

K7 is a small-scale (max. throw: 8 cm) stage 4 relay damage zone exposed in a pavement outcrop within the MGLM (Fig. 5.13). It is formed by two main NWN dipping normal faults. The two main segments generally strike to the WSW and to the NW in the breaching area (Fig. 5.13b). Strikes for all the branches are recorded, length-weighted and presented in the rose diagram, which reflect a wide range of orientations within the relay zone (Fig. 5.13a). Fracture intensities show values ranging from 10 m^{-1} to 200 m^{-1} (Fig. 5.13d), and the connecting node intensity ranges from 0 m^{-2} to 12 000 m^{-2} (Fig. 5.13e). The fracture intensity map and the connecting node frequency map show maximum values both in the breaching area and in the smaller-scale relay to the WSW along the northern main segment (Fig. 5.13d, e). All of the higher values of both the fracture intensity and the connecting node intensity are concentrated along the main through-going fault and are especially dense in the breaching area (Fig. 5.13).

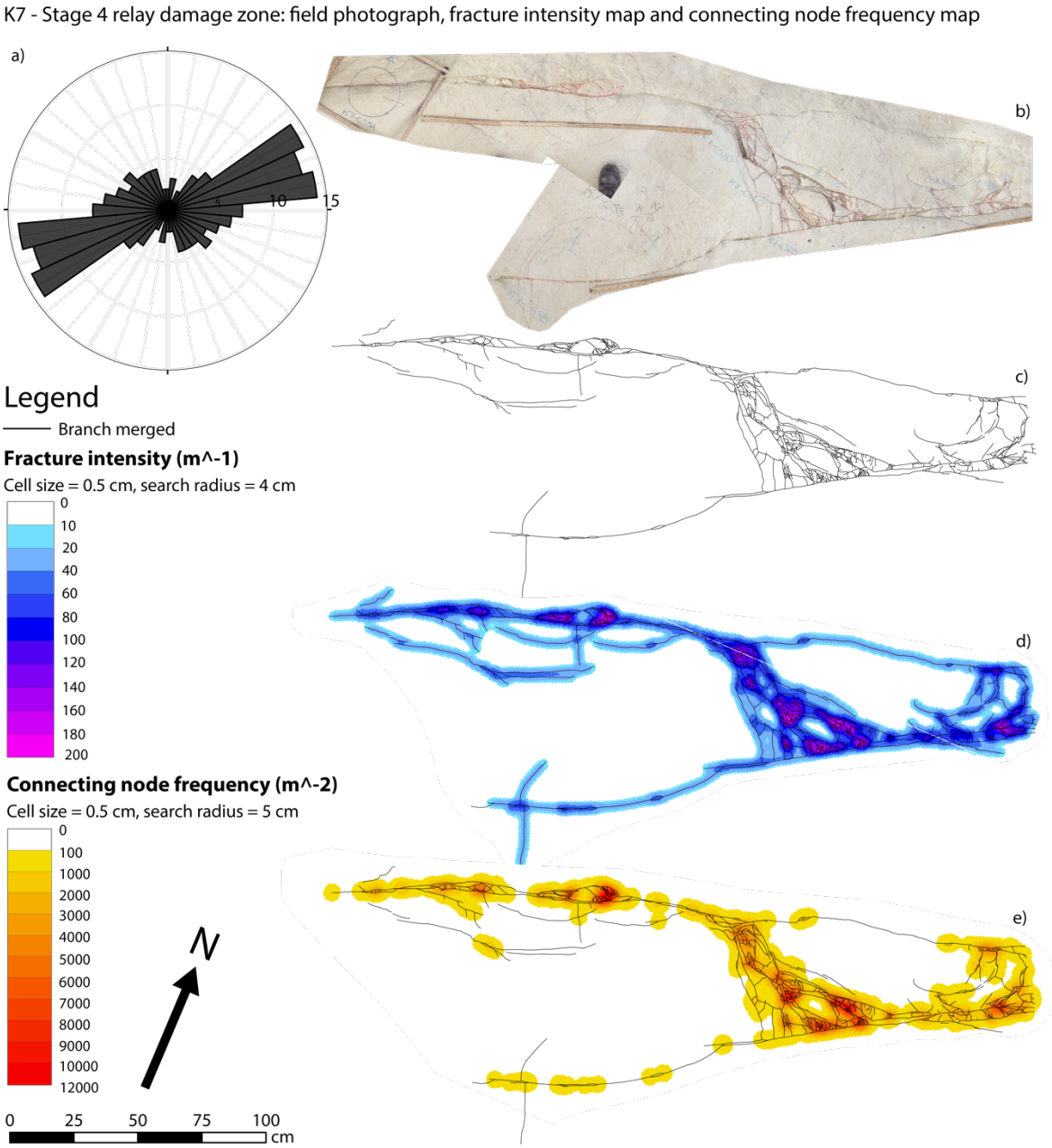

Figure 5.13: K7 is a stage 4 relay damage zone and is exposed in the MGLM. a) Rose diagram include length-weighted strikes of all branches within the locality, the two main segments strike towards the WSW. b) Field photograph. c) Associated merged branches. d) Fracture intensity map of K7 is created from c). e) Connecting node frequency map, created by the connecting nodes (Y and X).

14 Circle samples (0.0313 m^2) are placed along strike of the main through-going fault of the stage 4 relay damage zone (Fig. 5.14b), and represent a larger sample area than the fracture intensity and connecting node frequency maps (0.005 x 0.005 m) (Fig. 5.13d, e). Both the fracture intensity and the connecting node intensity increase from CS1 to CS6, where bifurcating geometries are documented. Note that CS5 and CS6 also represent a smaller-scale hard-linked relay structure within the main segment and display an

increase in fracture intensity, connecting node frequency and Nf (Fig. 5.14b). CS7 and CS8 represent relatively low values, where the segment mainly bends towards the southern main segment (Fig. 5.14). Furthermore, the fracture intensity, connecting node frequency and Nf increases from CS9 towards maximum in CS11, which represent breaching of the relay ramp, bending of the main segment and it exhibit the main linkage area of the relay structure.

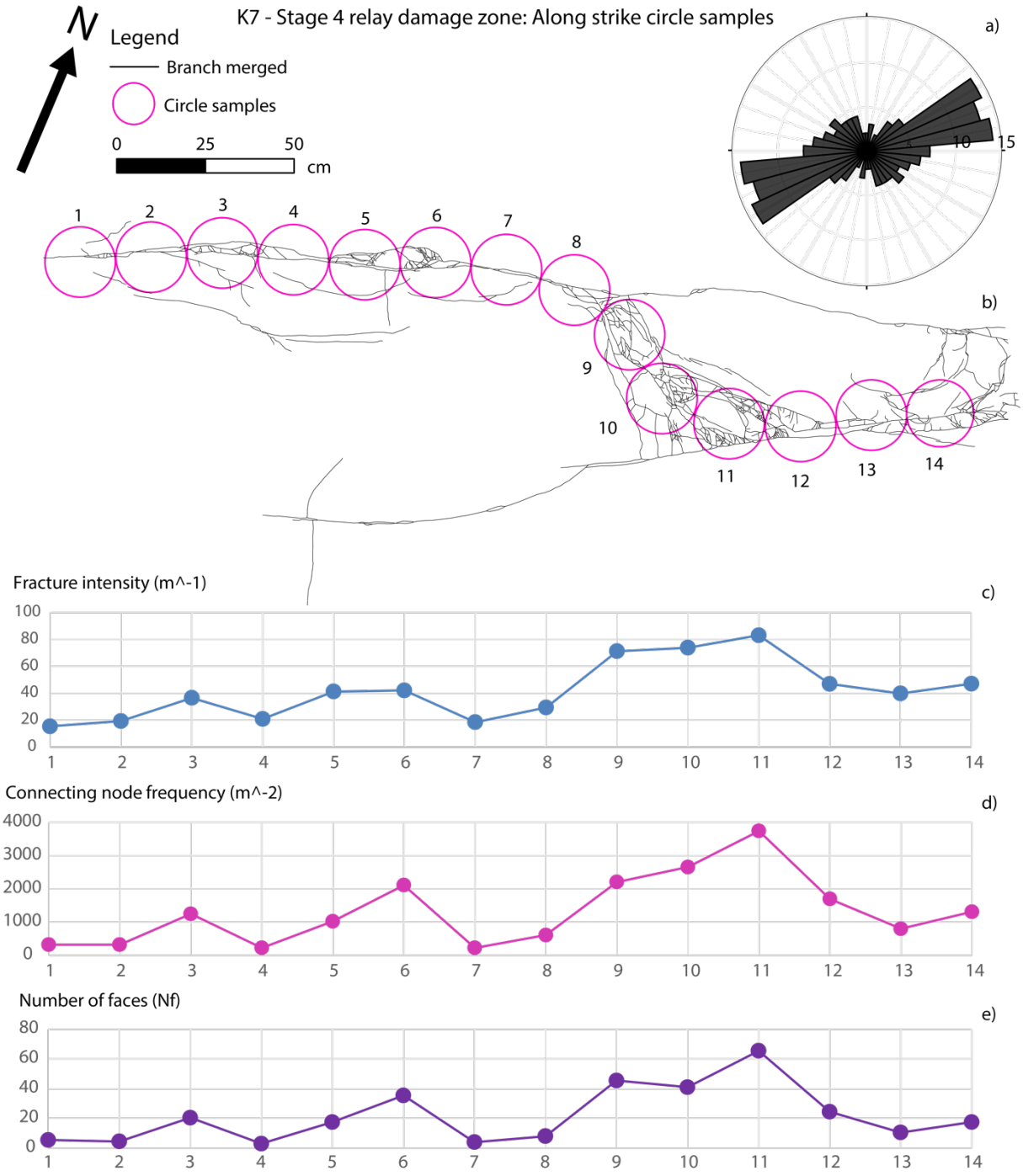

Figure 5.14: a) Rose diagram showing the length-weighted strikes of all the branches within the K7 damage zone b) mapped branches of K7 with circle samples (0.0313 m^2) along strike of the normal fault. c) Graph of fracture intensities (y-axis) of the associated circle samples (1 to 14, x-axis). d) Graph of connecting node frequencies (y-axis) of the associated circle samples (1 to 14, x-axis). e) Graph of number of faces (y-axis) of the associated circle samples (1 to 14, x-axis).

5.6.3 Splay fault damage zone variability – K3

K3 is a WSW-striking normal fault offsetting the LCLF, LGLM and MGLM with a maximum throw of 40 cm. The vertical outcrop of the splay fault shows a lens stretching in and above the conglomerate (LGLM-C1, Fig. 5.3) and the footwall splay zone is located in the upper part of the outcrop (MGLM-1) (Fig. 5.15). The fault is planar in the MGLM-1, with a dip of $\sim 60°$, and in the LGLM the fault has a more listric character showing a gentler dip with depth. Note that the rose diagram is dominated by the layer-parallel branches in the LGLM, which is due to their long lengths (Fig. 5.15a). The fracture intensity map shows intensities ranging from 10 to 180 m^{-1} (Fig. 5.15d). Fracture intensities are mainly less than 100 m^{-1}, with higher values restricted to the lens- and the splay area. The higher fracture intensities coincide with the higher connecting node frequencies, which have a maximum value of 10500 m^{-2} (Fig. 5.15e). Hence, higher values are restricted to the lens- and the splay area, and the remaining fault trace has connecting node frequencies less than 4000 m^{-2}.

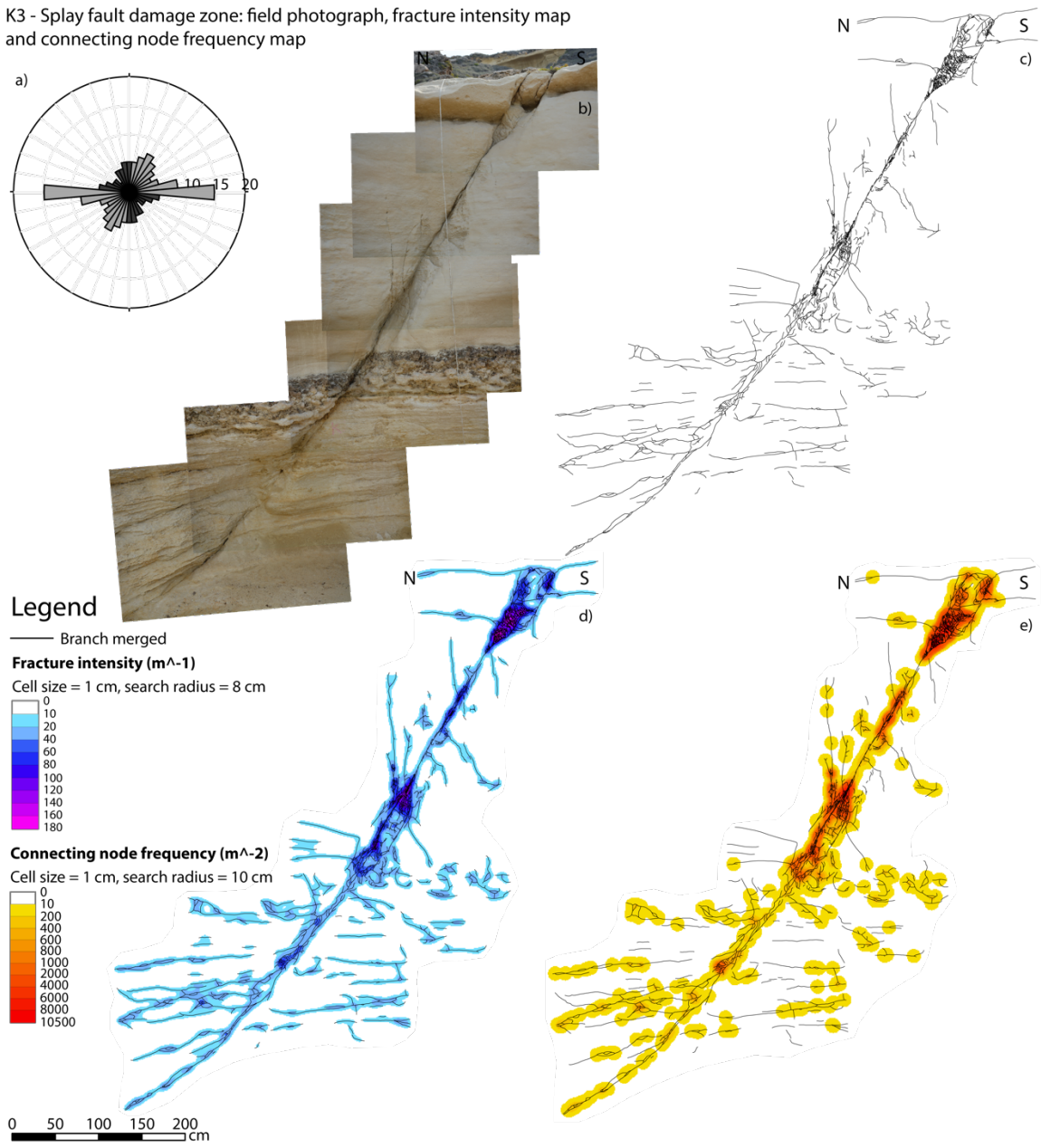

Figure 5.15: K3 is a splay fault damage zone and it is offsetting the LGLM and MGLM. a) Rose diagram include length-weighted dips of all branches within the locality. b) Field photograph and its c) associated merged branches. d) Fracture intensity map of K3 is created from c). e) Connecting node frequency map is created by the connecting nodes (Y and X).

42 circle samples (0.033 m^2) are placed along dip of K3 (Fig. 5.16b). The pink interval, CS1 to CS11, represent a simple part of the LGLM. The fracture intensities range from 10 to 23 m^{-1} (Fig. 5.16c), the connecting node frequencies range from 30 to 303 m^{-2} (Fig. 5.16d) and Nf range from 0 to 5 (Fig. 5.16e). In all graphs, the pink interval represents a stable area with relatively low values. The blue interval, CS12 to CS24, represents the transition from LGLM to MGLM and includes the MGLM-C1 and the lens (Fig. 5.16). The

fracture intensities in the blue interval range from 18 to 102 m^{-1}, the connecting node frequencies range from 121 to 3793 m^{-2} and Nf ranges from 1 to 59. Peak values are located in CS20, CS23 and CS24 for all the three graphs (Fig. 5.16c, d, e). CS24 represents the linkage point of the lens and the maximum connective node frequency for the blue interval. CS23 is a complex area below the linkage point, representing the maximum fracture intensity and Nf. The yellow interval, CS25 to CS31 represents a simple part of the MGLM. The fracture intensities range from 10 to 37 m^{-1}, the connecting node frequencies range from 152 to 1335 m^{-2} and the Nf from 4 to 20.5, all graphs showing its highest values in CS27 to CS29. The purple interval, CS32 to CS37, represents the bifurcation/linkage area and the parent segment of the footwall splay. The purple interval represents the overall maximum value of the fracture intensity (123 m^{-1}), the connecting node frequency (6767 m^{-2}) and the Nf (102), all in CS34. The peak value occurs in CS34, representing a large part of the splay damage zone (Fig. 5.16b). CS33 to CS35 represent significantly higher connecting node frequencies than the highest values for the blue interval. In general, the purple interval represents the peak values of the fracture intensity, connecting node frequency and Nf. The red interval, CS38 to CS41 represents the footwall splay of the splay zone. The fracture intensity range from 23 to 58 m^{-1}, the connecting node frequencies range from 243 to 1639 m^{-2} and Nf from 3 to 19. Hence, the complexity of the red interval may be comparable with the complexity of the blue interval.

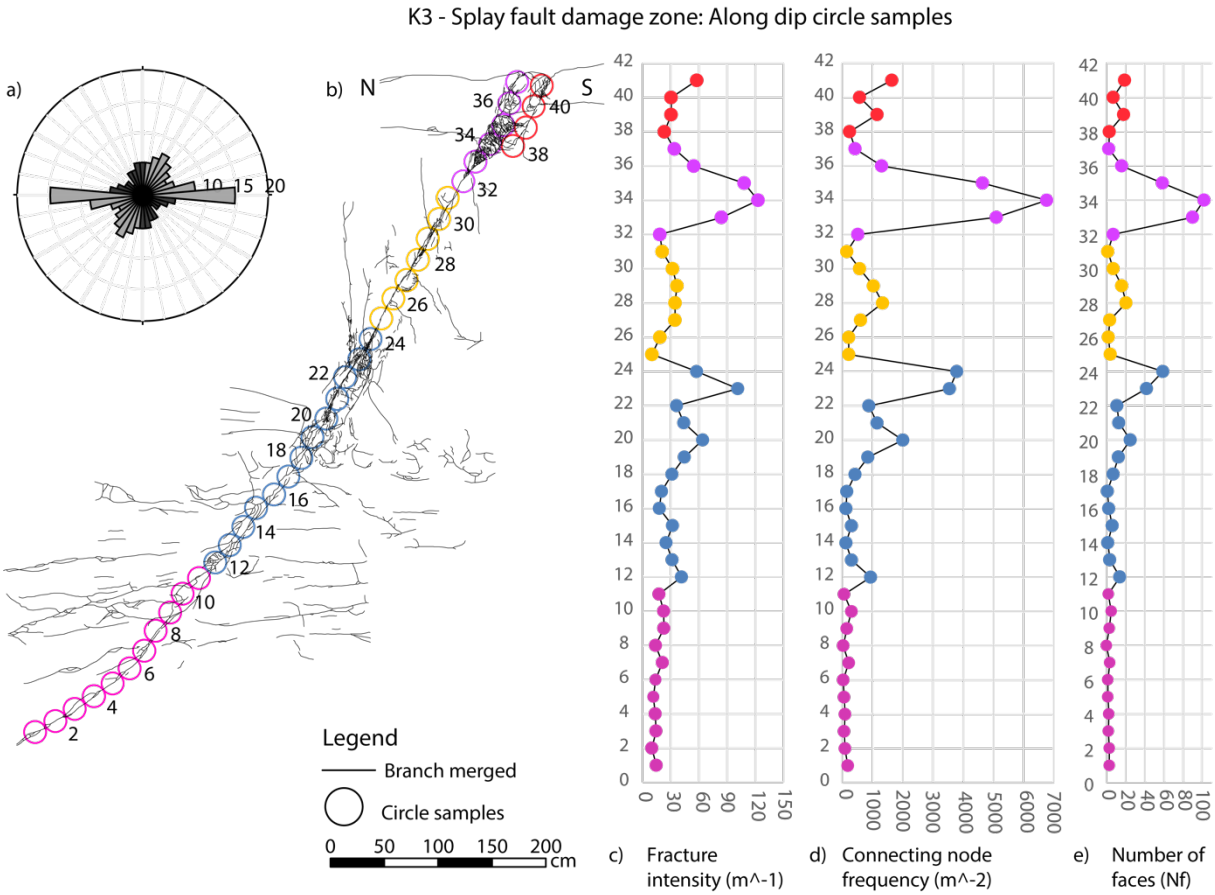

Figure 5.16: a) Rose diagram showing the length-weighted dips of all the branches within the K3 damage zone. b) Mapped branches of K3 with circle samples (0.033 m^2) along dip of the normal fault. c) Graph of fracture intensities (x-axis) of the associated circle samples (1 to 41, y-axis). d) Graph of connecting node frequencies (x-axis) of the associated circle samples (1 to 41, y-axis). e) Graph of number of faces (x-axis) of the associated circle samples (1 to 41, Y-axis).

6 Discussion

This chapter aims to addresses the causes of topological similarities and differences of the studied damage zones (Section 6.1) and the internal spatial variability occurring along strike/dip of individual damage zones (Section 6.2). The typical topological character of the damage zone types is also discussed (Section 6.3). Further, the documented topology is used to discuss how connectivity evolves over time as faults and their damage grow and develop (Section 6.4). Finally, implications for topology, connectivity and fluid flow are discussed, in addition to limitations using topology on seismic resolution datasets (Section 6.5).

6.1 Topological similarities and differences between fault damage zone types

The topology of documented relay damage zones overlap with the topology of fault tip damage zones and splay fault damage zones (Fig. 6.1). This implies that relay damage zones show similar proportions of nodes and branches as fault tips at stage 2 (and stage 1) and similar proportions of nodes and branches as splay fault damage zones in stage 3. Consequently, the damage zones will show similar connectivity.

Overlap between fault tip damage zones and relay damage zones in the node- and branch-plots occur only with stage 2 relay damage zones (Fig. 6.1). This is explained by the fact that a stage 2 relay damage zone represents two fault tip damage zones approaching each other (e.g. Fossen and Rotevatn, 2016), resulting in a bifurcating geometry in both cases and therefore similar topology and connectivity. In contrast to a stage 2 relay damage zone where two fault tips propagate in opposite directions, a fault tip damage zone propagates freely in one direction and the stress increase zone is not disturbed by the stress drop zone of neighbouring faults (e.g. Willemse et al., 1996; Gupta and Scholz, 2000). A stage 2 relay damage zone has a limitation of space and time for the fault tip to develop the typical wedge shape geometry due to growth retardation as the tip propagates into the neighbouring faults stress drop zone (e.g. Willemse et al., 1996; Gupta and Scholz, 2000; Fossen and Rotevatn, 2016). Additionally, the tip will eventually link to

the neighbouring fault segment and form a stage 3 relay damage zone (e.g. Peacock and Sanderson, 1991, 1994).

Topology of stage 3 relay damage zones overlap with the topology of splay fault damage zones in the node- and branch plots (Fig. 6.1). At the point of hard linkage (stage 3) more connecting nodes and connecting branches form between the two main segments in plan view, resulting in a higher connectivity than stage 2 relays and fault tips. A cross section through a breached relay ramp may also show a splay fault damage zone (e.g. Childs et al., 1995; Walsh et al., 1999; Bonson et al., 2007; Fossen and Rotevatn, 2016) (Fig. 2.6) and could demonstrate why such overlap in topology occurs. Overlap in topology could be explained by the fact that both damage zones are a result of two hard linking faults, or single (or double for relays) tip interaction (sensu Fossen et al., 2005), where relays are observed in plan view and splays are observed in cross section. Hard linkage (stage 3 relay damage zones and splay fault damage zones) results in a higher connectivity than fault tip damage zones and stage 2 relay damage zones. In general, the relay damage zones show highest proportion of Y-nodes and CC-branches and highest connectivity, the splay fault damage zones show medium proportion of Y-nodes and CC-branches and medium connectivity. The fault tip damage zones show lowest proportion of Y-nodes and CC-branches and the lowest connectivity (Fig. 6.1).

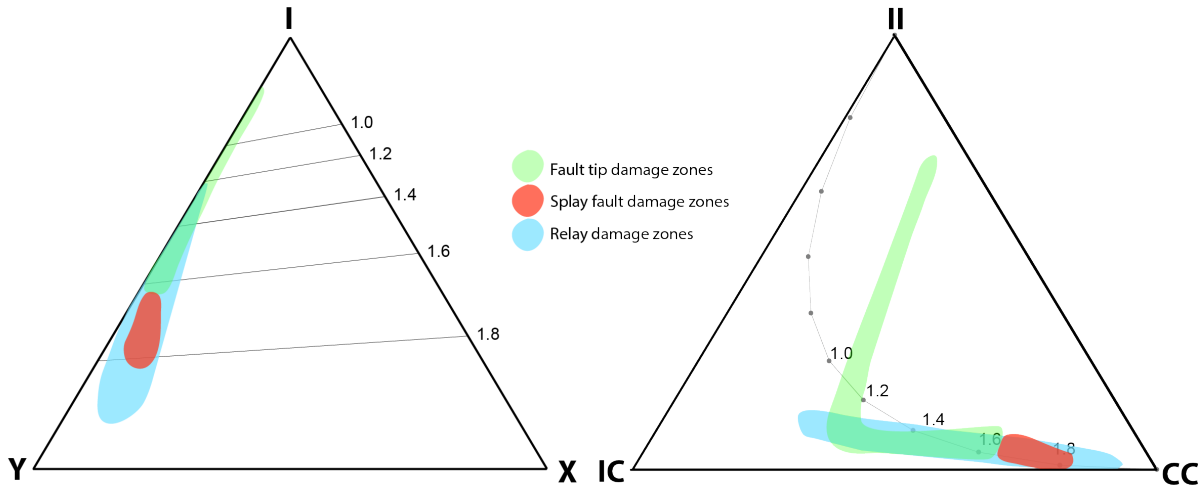

Figure 6.1: Node- and branch plots showing the topology of fault tip-, splay fault- and relay damage zones. The node plot shows the percentages of I- Y- and X-nodes within the damage zones. The branch plot represents the percentages of II- IC- and CC- branches within the damage zones. Polygons are contoured from plotted and studied examples of the three damage zone types.

6.2 Spatial variability within fault damage zones

All the studied damage zones (fault tip, splay and relay) include simple and complex parts. The simple parts comprise a fault segment and damage with low fracture intensity, connecting node frequency and number of faces. A more complex part includes high and highly variable fracture intensity, connecting node frequency and number of faces. The documented complex parts are wider damage zone areas, such as areas of bifurcation, linkage and bends, which result from increased stresses and stress perturbations (e.g. Rawnsley et al., 1992; Aarland and Skjerven, 1998; Meyer et al., 2002; Berg and Skar, 2005). Perturbed stress field related to slip-events on faults control the orientation of smaller-scale fractures, due to rotation of the principal stresses (e.g. Rawnsley et al., 1992; Barton and Zoback, 1994). It has been predicted that stresses are perturbed and increased both at fault tips and where fault segments interact (e.g. Segall and Pollard, 1980; Willemse and Pollard, 1998; Tamagawa and Pollard, 2008). This caused a more complex fracture network geometry than the simple parts, which formed in a way that is more consistent with the regional stresses. On a larger scale this implies that the studied zones of bifurcation or linkage areas may act as conduits for fluid flow if the fractures are unfilled dilatation fractures and/or faults (as in the study area) or as a baffle or barrier in the case of deformation bands or mineralised fractures (e.g. Larsen, 1988; Caine et al., 1996; Sibson, 1996; Childs et al., 1997; Aydin, 2000; Rotevatn et al., 2007; Ferrill and Morris, 2008; Bastesen et al., 2009; Faulkner et al., 2010; Davidson et al., 2016) (see Section 6.5.1 for more fluid flow aspects).

6.3 Evolution of the topology of fracture networks during fault growth

As a fault grows and develops, its character will typically change with greater amounts of strain, resulting in increased displacement and damage (e.g. Walsh and Watterson, 1988; Cowie and Scholz, 1992a, b, c; Cartwright et al., 1995; Cowie et al., 2000; Micarelli et al., 2006; Childs et al., 2009). The studied damage zones may add important information about the evolution of damage during fault growth. Connectivity develops with time and maturity (e.g. Morley and Nixon, 2016; Duffy et al., in review). Therefore, present day damage zones characterised by low connectivity represent analogues for immature

damage zones, while damage zones with high connectivity represent analogues for mature damage zones. All three damage zone types show variable degree of connectivity and may be related to different stages of fault growth. In this section the results are used to illustrate how connectivity evolves over time.

6.3.1 Topology of fracture networks during development of a fault tip

The studied examples of fault tip damage zones can be divided into stage 1 and stage 2 fault tip damage zones (Fig. 6.2). The nodal topology of stage 1 fault tip damage zones is dominated by I-nodes and have no X-nodes, while braches are dominated by II-branches and IC-branches. Thus, stage 1 fault tip damage zones have a lower connectivity than stage 2 fault tip damage zones. Stage 2 fault tip damage zones still have high amounts of I-nodes, but are dominated by Y-nodes and show the development of some X-nodes. Branches are dominated by CC-braches, although they still have a fair amount of IC-braches (Fig 6.2). Based on these observations stage 1 fault tip damage zones are immature and therefore less complex than stage 2 fault tip damage zones. This implies that stage 1 fault tip damage zones have lower values of fracture intensity, connecting node frequency, number of faces and lower connectivity relative to stage 2 fault tip damage zones.

Ultimately, a fault tip damage zone will form a topology similar to the contoured stage 1 fault tip damage zones. With accumulation of strain, it will develop to show a topology similar to the contoured stage 2 fault tip damage zones (Fig. 6.2). In sum, the topology will develop from an I-node and II-branch to IC-branch dominated system and further, to a Y-node and CC-branch dominated system with higher connectivity. It can also be suggested that stage 1 fault tip damage zones form at the tip of shorter faults than stage 2 tip damage zones, as the width of the stress increase zone at a fault tip is proportional with the fault length (Cowie and Scholz, 1992a; Scholz and Anders, 1994; Cowie and Shipton, 1998; Vermilye and Scholz, 1998). The reason for more damage in the hangingwall relative to the footwall of a fault is often due to fault tip propagation toward the bending hangingwall (e.g. Lewis et al., 2002; Berg and Skar, 2005), implying more damage at fault tips with more bending and higher displacement (conceptual stage 2) and less damage at lower displacement and less bending (conceptual stage 1). At higher amount of strain, the fault tip damage zone is left as a part of the wall damage zone, if the length of the fault increases significantly (e.g. Kim et al., 2004). Note that in this study the polygons do not overlap

(Fig. 6.2). However, such an overlap could appear if more fault tip damage zones were studied.

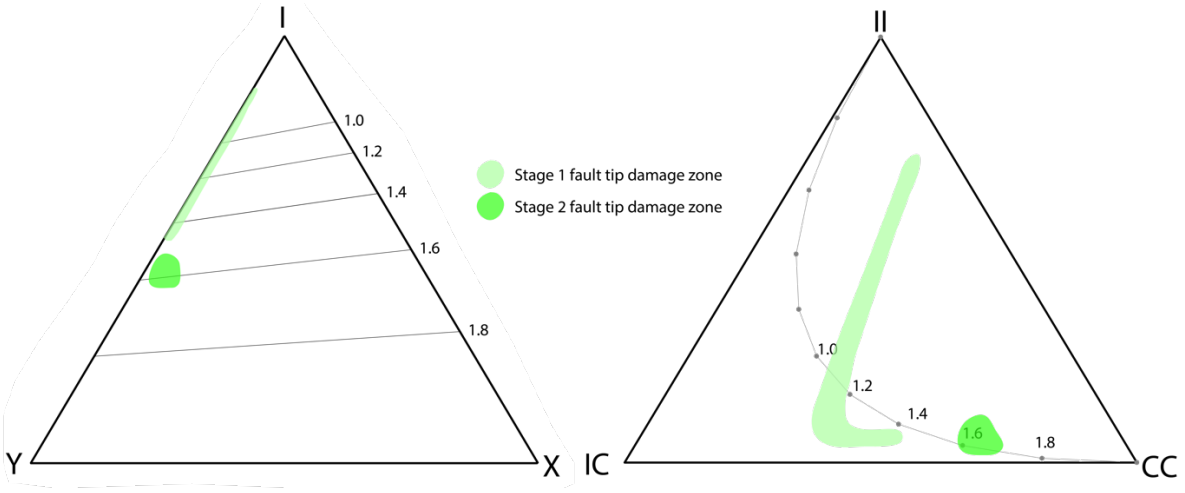

Figure 6.2: Node- and branch plots showing the topology of fault tip damage zones. The node plot shows the percentages of I-, Y- and X-nodes within the damage zones. The branch plot represents the percentages of II-, IC- and CC- branches within the damage zones. Polygons are contoured from plotted and studied examples of stage 1 and 2 fault tip damage zones.

6.3.2 Topology of fracture networks during development of a splay zone

Splay fault damage zones display a high degree of architectural variability, although they all include splay fault(s) and lens(es). The three studied examples vary from weakly deformed to highly deformed and from distributed to localised deformation. Despite the architectural differences they show less variability in topology and connectivity (Fig. 6.3). The architectural differences are reflected in the fracture intensity, connecting node frequency and number of faces etc. and are therefore accounted for by the use of parameters gained from topology. Splay fault damage zones plotted in the lower part of the polygon (Fig. 6.3) show distributed deformation, with higher amounts of connecting nodes and number of faces than a splay fault damage zone plotted in the upper part of the polygon. This implies that the upper part of the polygon could represent a narrow conduit (or baffle/barrier) for fluid flow, while the lower part could represent a wider conduit (or baffle/barrier). As offset is accommodated at the faults, the amount of connecting nodes will increase along with the connectivity of the splay fault damage zone. This is due to the increase in fracture intensities and formation of more connecting branches in and around the splay zone. Mechanical stratigraphy may play an important role as the studied faults

always display the occurrence of lenses in and above the conglomerate (LGLM-C1, Fig. 5.3). This is also observed by Michie et al. (2014) on a larger scale in the study area. Additionally, there is a higher occurrence of layer-parallel fractures in the Lower Globigerina Limestone Member (LGLM) than in the Middle Globigerina Limestone Member (MGLM), which gives the LGLM more distributed deformation and the MGLM more localised deformation (lenses and splays).

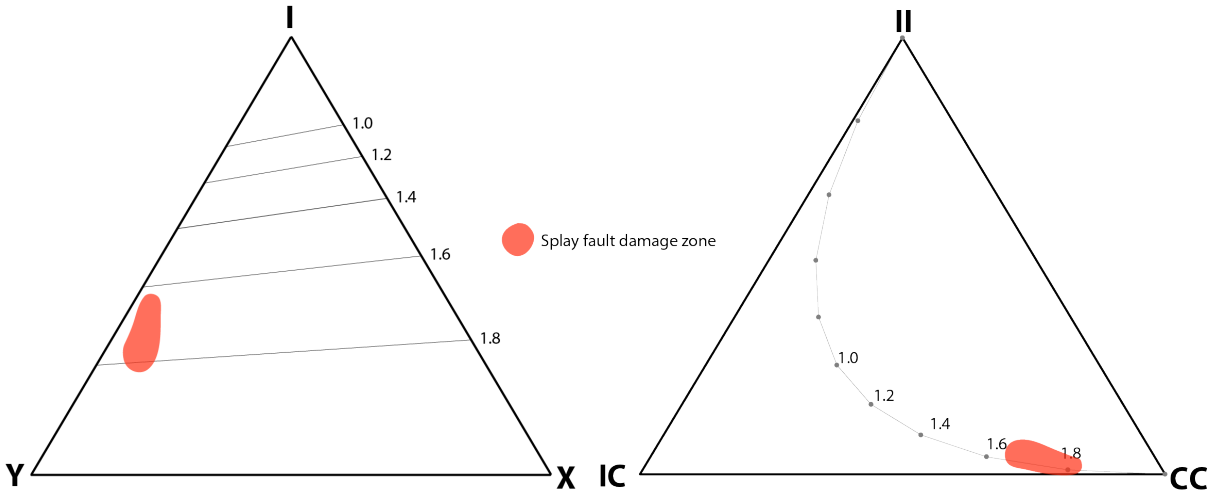

Figure 6.3: Node- and branch plots showing the topology of splay fault damage zones. The node plot shows the percentages of I-, Y- and X-nodes within the damage zones. The branch plot represents the percentages of II-, IC- and CC- branches within the damage zones. Polygons are contoured from plotted and studied examples of splay fault damage zones.

6.3.3 Topology of facture networks during the development of a relay zone

The birth and destruction of relay ramps are well documented in the literature and their evolution well described (e.g. Larsen, 1988; Peacock and Sanderson, 1991, 1994; Walsh and Watterson, 1991; Huggins et al., 1995; Childs et al., 2009; Bastesen and Rotevatn, 2012; Fossen and Rotevatn, 2016). The resulting damage and topology have been documented in this study (Fig. 6.4.) and confirm the increasing complexity with time. It is worth mentioning that stage 1 relay damage zones do not occur in the field area and may not be that common since soft linkage could occur early in the growth history when fault segments approach each other. Smaller scale stage 1 relays can be found within other damage zone types and are not observed standing alone. However, their topological character would be similar to immature fault tip damage zones. A conceptual stage 1 relay

damage zone is approximated in the node- and branch plots and studied stage 2, 3 and 4 relay damage zones are separate polygons contoured around studied examples (Fig. 6.4).

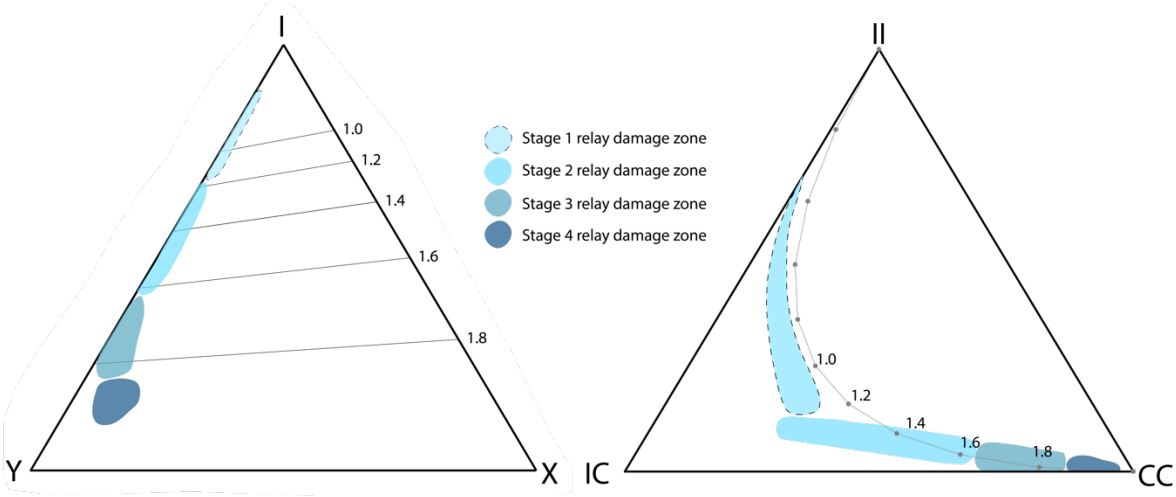

Figure 6.4: Node- and branch plots showing the topology of relay damage zones. The node plot shows the percentages of I-, Y- and X-nodes within the damage zones. The branch plot represents the percentages of II-, IC- and CC- branches within the damage zones. Polygons are contoured from plotted and studied examples of stage 2, 3 and 4 relay damage zones. A conceptual stage 1 relay damage zone is also indicated in both plots.

The fault tip(s) of a stage 2 relay damage zone will most likely be in the stress drop region of the neighbouring fault and its growth is therefore retarded (e.g. Willemse et al., 1996; Gupta and Scholz, 2000). As strain is accommodated, growth will continue and the relay ramp will be breached to form a stage 3 relay damage zone. More connecting nodes and branches are formed in the breaching area of a stage 3 relay damage zone, resulting in a higher connectivity. With even more accommodation of strain, the fracture system will increase its connectivity as more branches link to the trough-going fault of the stage 4 relay damage zone. The increase in connectivity and orientation complexities from stage 2 to 4 relays can be related to the stress perturbation around the growing faults and their relative stress drop and stress increase zones as previously mentioned (e.g. Willemse et al., 1996; Gupta and Scholz, 2000; Kattenhorn et al., 2000). Additionally, orientation complexities could be caused by increase in the ratio of fault-parallel to fault-perpendicular stress, causing fractures to grow at higher angles relative to the main fault (e.g. Kattenhorn et al., 2000). Note that further studies may show an overlap in topology between the stages. However, the plots show a good approximation of the topology of the damage occurring around different stages of relay growth. Furthermore, the stage of a

relay damage zone might be hard to interpret in low resolution seismic datasets where linkage geometries are strongly influenced by resolution: for example a stage 3 relay damage zone at outcrop resolution may be viewed as a stage 2 relay damage zone at seismic resolution (e.g. Walsh and Watterson, 1991).

6.4 Evolution of fault networks and their topology

This study focuses on detailed analyses of small-scale normal faults and quantification of variations within damage zones and the variation with time. Such detailed analyses are of importance to understand large-scale fault networks and their evolution of damage. Parameters such as displacement versus length, number of active faults and accumulation of throw with time have previously been added to describe the evolution of fault networks during rifting (e.g. Cowie et al., 2000; Gawthorpe and Leeder, 2000). Valuable information can be added to these evolutionary models by implementing topology, so that we can better understand how the arrangement and connectivity of the fault network and damage within, developed temporally. Duffy et al. (in review) and Morley and Nixon (2016) suggest evolutionary trends of topology and connectivity with increasing strain, covering the fault network evolution. In this study information is added from the small-scale damage occurring during rifting. The studied damage zones are used as proxies for different stages of damage zone growth, where damage zones with a low connectivity represent an immature stage and damage zones with high connectivity represent a mature stage. Thus, a three-stage model for the topological development of simple rifting is suggested in this study (Fig. 6.5). Concepts from literature showing the transition from distributed to localised strain during the evolution of a normal fault system are used as a baseline for the fault development (e.g. Nicol et al., 1997; Cowie et al., 2000; Gawthorpe and Leeder, 2000; Walsh et al., 2001; Meyer et al., 2002) and additional information gained from topology are added to the model (Fig. 6.5).

Stage 1: Fault initiation

This stage is characterised by initiation and growth of multiple isolated faults, hence the network shows distributed strain (e.g. Cowie et al., 2000; Gawthorpe and Leeder, 2000; Walsh et al., 2001). Typical damage zones in this stage of the fault network evolution are stage 1 and 2 fault tip damage zones and stage (1-) 2 relay damage zones. Underdeveloped

splay fault damage zones may also occur (Fig. 6.5). Topology is therefore characterised by a domination of I-nodes and IC-branches. The connectivity stay below 1.6 C_B (average connections per branch) and low values of fracture intensity, connecting node frequency and number of faces characterise the fault network (Fig. 6.5). Single-phase rifting experiments with low strains from Duffy et al. (in review) show connectivity below 1.0 C_B. However, adding damage zone topology will revile a higher connectivity at this stage (~1.2-1.6 C_B). In general, this stage is characterised by isolated fault tips and a domination of I-nodes and IC-branches due to low connectivity damage zones (i.e. fault tip damage zones and soft linked relay damage zones).

Stage 2: Interaction and linkage

As extension continues, existing faults extend their lengths, resulting in more interaction and linkage of fault segments (Fig. 6.5) (e.g. Fossen and Hesthammer, 2000; Gawthorpe and Leeder, 2000). This evolutionary stage is characterised by a maximum number of active faults. Stress shadows of soft- and hard-linked faults can, however, cause decreased activity of neighbouring faults (e.g. Cowie et al., 2000). The increase of fault segment interaction results in a domination of stage 3 relay damage zones, while isolated fault segments will typically include stage 2 fault tip damage zones. More complex splay fault damage zones are also developed (Fig. 6.5). Consequently, the topology is characterised by a domination of Y- nodes, in addition to more X-nodes relative to stage 1. The increase in connecting nodes result in a higher connectivity (~1.6-1.8 C_B), due to more connecting nodes formed at breached relays and splays. This results in increased connecting node frequency and a domination of IC- and CC-branches. Total trace length will generally increase during this evolutionary stage, resulting in an increase in fracture intensity. The connectivity is comparable with Milne Point Alaska (Duffy et al., in review), however, the fault network show more connections across strike, in contrast to simple rifting with minor connections across strike (Fig. 6.5). Summarised, this stage is dominated by interaction damage zones and a domination of Y-nodes and IC- and CC-branches due to damage zones with medium connectivity (i.e. stage 3 relay damage zones and more complex splay fault damage zones).

Stage 3: Through – going fault zones

Continued extension results in localisation of stain within the fault network. Deformation is concentrated along a few through-going faults, causing inactivity of minor faults in stress shadows of major faults (Fig. 6.5) (Cowie et al., 2000; Gawthorpe and Leeder, 2000; Walsh et al., 2001). Active through-going faults typically involve stage 4 relay damage zones, which are single breached or doubly breached, and complex splay fault damage zones (Fig. 6.5). The damage around the through-going faults is dominated by connecting nodes and CC-branches. The fracture intensity and connecting node frequency continues to increase and displacement is accommodated by major faults due to localisation of strain (e.g. Walsh et al., 2001). The inactive, minor faults in the stress shadows of the trough-going faults do not experience damage zone growth throughout this stage and thereby retain their topology. Even though the minor fault damage zones are abandoned they typically have C_B around 1.60. The overall topology shows a highly connective system (>1.8 C_B) relative to previous stages (Fig. 6.5). Note that the high connectivity is along strike, not across strike (i.e. faults are parallel and not connected with other faults) (Duffy et al., in review), however, the complex damage along strike will be highly connective. In general, this stage is characterised by through-going fault zones and the topology is highly dominated by Y-nodes and CC-branches due to damage zones with high connectivity (i.e. stage 4 relay damage zones and complex splay fault damage zones).

Summarised, this implies that during extension, damage zones in fault networks evolve from being dominated by I-nodes and IC-branches (stage 1) to a system dominated by Y-nodes and CC-branches (stage 3). Consequently, the damage within the fault network will show low relatively connectivity at an early stage (stage 1), but comparatively high connectivity as extension progresses (stage 3) (Fig. 6.5).

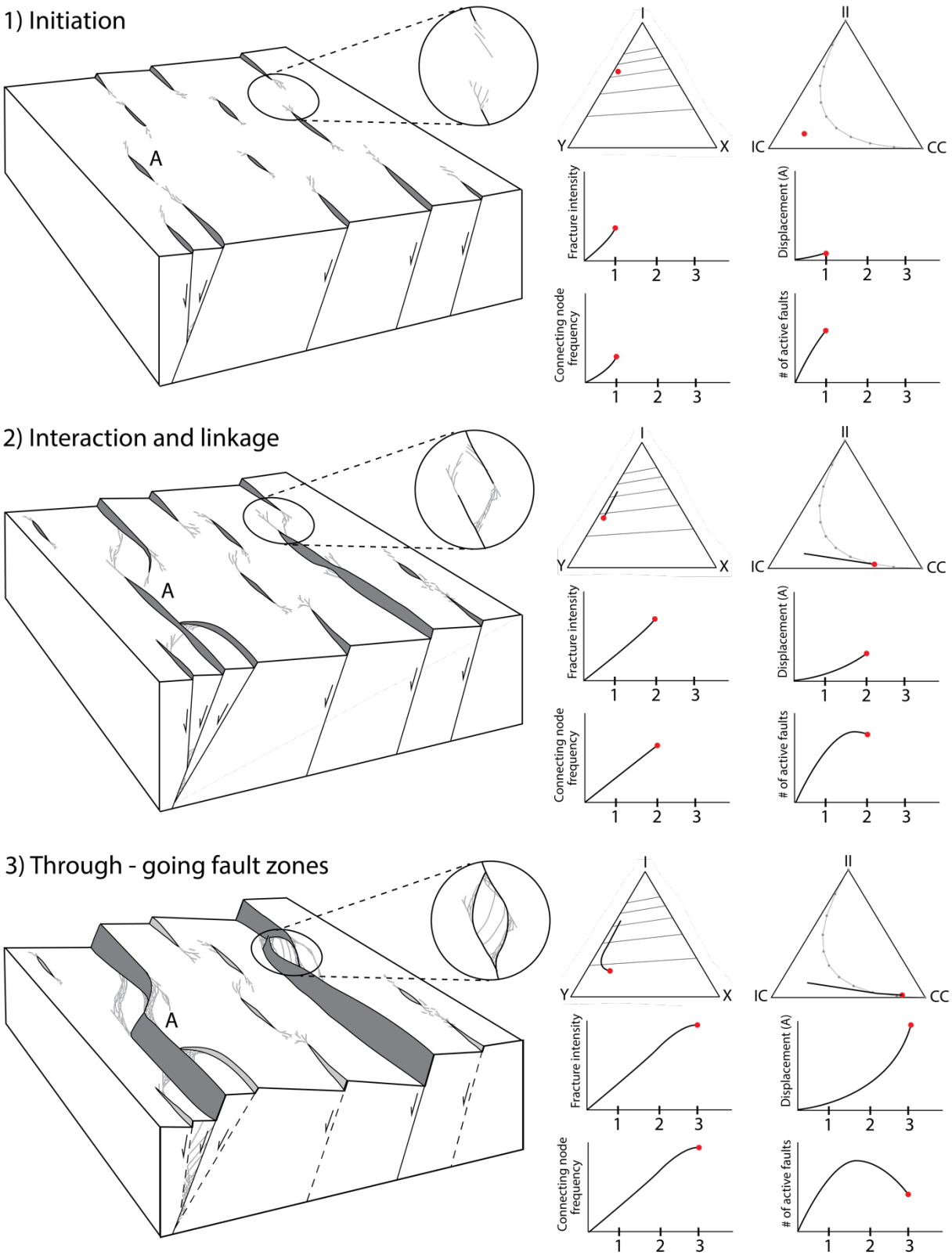

Figure 6.5: Conceptual model showing how topology and connectivity evolves during the evolution of a rift fault network. The fault growth aspects are modified from Cowie et al. (2000) and Gawthorpe and Leeder (2000), whereas the aspects of topology and connectivity are from this study. For each stage, six diagrams are included; node plot, branch plot, fracture intensity plot, connecting node frequency plot, displacement plot and number of active faults plot. The node plot shows the proportions of nodes, where average

connections per branch (i.e. connectivity) is indicated. The branch plot shows the proportions of branches, where the connectivity is indicated. The fracture intensity plot indicates the relative fracture intensity of the stages (1 to 3, x-axis). Connecting node frequency plot indicates the relative connecting node frequency of the three stages (1 to 3, x-axis). The total accommodation of displacement for segment A is indicated in the displacement plot for the three stages (1 to 3, x-axis). The relative number of active faults in the fault network is indicated in the lowermost right plot throughout the three stages (1 to 3, x-axis). Stage 1) Initiation: multiple isolated faults are formed during early rift initiation and topology shows a domination of I- nodes and IC-branches. Fracture intensity, connecting node frequency and displacement are low at this stage, while the number of active faults is relatively high. Overall, the connectivity of the network is low at this stage (<1.6 C_B). Stage 2) Interaction and linkage: Interaction and linkage between fault segments dominate in this stage. A higher number of active faults are recorded, although decreased activity characterise faults in stress shadows of interacting faults. Due to fault interactions, the fault network is more connected, which is reflected by higher percentages of connecting nodes (Y, X) and IC- and CC- branches. Fracture intensities and connecting node frequencies increases. The fault network and its damage zones show a medium connectivity at this stage (~1.6-1.8 C_B). Stage 3) Through-going fault zones: Deformation is localised along a few through-going faults, while smaller faults become inactive. Due to the increase in displacement of the major faults, fracture intensity and connecting node frequency continue to increase during this stage. Topology of abandoned faults will remain relatively constant, although the activity on the through-going faults increases the amount of connecting nodes and branches. The connectivity of the network is high at this stage (>1.8 C_B).

6.5 Implications and limitations

6.5.1 Structural controls and fluid flow in fault and fracture networks

In low permeability rocks, fracture-dominated permeability is strongly linked to structural connectivity (e.g. Faulkner et al., 2010). Thus, it is crucial to understand the variations occurring in structurally complex settings and how these zones control the fluid flow. Results from fault tip damage zones show that there is an increase in fracture intensity, connecting node frequency and number of faces before, in and after bifurcation points (Figs. 5.11 and 5.12). The connectivity of fault tip damage zones records low connectivity and maturity (Section 6.3.1 and 6.4). It is observed that the fault tip damage zones localise present day fluids (rainwater or seawater) due to wet patches around the fault tip and dry host rock. This is consistent with Ogata et al. (2014) who documented bleaching patterns around fault tips as an indication for paleo-fluid flow. It is also consistent with work from Curewitz and Karson (1997) who document that hydrothermal outflows most often occur at fault tips and fault interaction zones, as these are regions

with elevated stresses. Additionally, Tamagawa and Pollard (2008) shows that the most productive wells are located at fault tips of active faults, where perturbed stress field cause the fractures to dilate or shear and therefore increase the permeability. Wet patches observed at fault tips (study area) are also consistent with redox fonts and cemented mounds in the damage zones, more closely studied in the related sister MSc project (Vilde Dimmen).

Increased fracture intensity, connecting node frequency and number of faces are documented along the through-going fault in breached relay damage zones, with peak values in the linkage zones (Figs. 5.13 and 5.14). Dockrill and Shipton (2010) also document fluid pathways in such structurally complex areas as relay ramps, fault intersections and fault bends, mainly due to the irregular geometry causing perturbed stress fields (e.g. Rawnsley et al., 1992; Aarland and Skjerven, 1998; Meyer et al., 2002; Berg and Skar, 2005; Tamagawa and Pollard, 2008). Curewitz and Karson (1997) show that it is typical that hot springs occur where two or more faults interact due to re-opening of fractures in the perturbed stress fields (e.g. Segall and Pollard, 1980). This conforms with work showing that linkage areas in relay structures are associated with high fracture frequencies and fracture sets with highly variable orientations and therefore act as conduits for fluid flow (e.g. Rotevatn et al., 2007; Bastesen et al., 2009; Rotevatn and Bastesen, 2014). Additionally, Fossen et al. (2005) argues that these types of linkage areas (branch points) are areas of high structural complexities and fluctuating orientation patterns, also documented in this study.

The reasons for fluid localisation in these areas are due to a number of factors. Increased connectivity and connective node frequency gives a greater permeability, especially in originally low-permeability rocks. As mentioned earlier, perturbed stress fields around fault tips and interaction zones cause fractures to dilate or shear cause fractures to remain open and to be conduits for fluid flow (e.g. Segall and Pollard, 1980; Martel, 1990; Curewitz and Karson, 1997; Kattenhorn et al., 2000; Tamagawa and Pollard, 2008). Hence, spatial variability and complex areas should be documented and care should be taken when placing a well near a possible linkage area (e.g. Fossen et al., 2005; Rotevatn et al., 2007) as faults in general are associated with drilling hazards (e.g. Grauls et al., 2002; Faulkner et al., 2010).

6.5.2 Limitations using topology on seismic resolution datasets

Topology quantifies network properties by the use of dimensionless parameters and is therefore not biased to scale, however, there are some precautions to be made when using topology in seismic resolution datasets. This study is based on high resolution outcrop data. When applying this method to seismic resolution datasets, different topologies may be reviled due to low resolution. For example, Nixon et al. (2012) show that with a lower seismic resolution a higher amount of I-nodes and lower amounts of Y- and X-nodes will be observed relative to seismic data with higher resolution. These findings imply that high-resolution outcrop data shown in this study, should be included when using topology of fault networks in seismic, if not the data will be biased and appear less connected. For larger scale fault networks, there will be a preservation problem for X-nodes at high displacements and the topology will be more dominated by I- and Y-nodes. In these cases, the displacement minimum and maximum are clear and one should divide Y and X-nodes into splaying nodes (Ys), abutting nodes (Ya) and crossing nodes (Yc/X) to form a new triangular plot. This will prevent the fault network to plot along the I-Y line of the node plot and may give a more detailed topological description of the fault network (e.g. Nixon et al., 2012; Nixon, 2013; Morley and Nixon, 2016).

6.5.3 Implications for topology and connectivity

This model (Fig. 6.5) increases our understanding of damage zone growth and the resulting topology and connectivity. Digitising topology of various damage zone types will quantify parameters presented in detail in this study (topology, connectivity, fracture intensity, connecting node frequency and number of faces). Additionally, fracture frequency, dimensionless intensity, average branch/line length, average face size and length are easily calculated from the same parameters (Sanderson and Nixon, 2015). An advantage using topology is that it is dimensionless and therefore the topology for different structurally complex settings can be used and compared on a range of scales. Some studied examples show similar topology, but highly variable fracture intensity and connecting node frequency which is much more scale-dependent. Thus, it is convenient to get all these parameters by topological characterisation in ArcGIS, in addition to a neat overview of the connectivity of the studied damage zone. Duffy et al. (in review) document

the evolution of topology in single and multiphase rifts, but they do not include the damage zones. Their study shows that single phase rifting results in low final connectivity, while this study shows that if one includes the damage zones in such characterization, it results in high final connectivity along strike. The connectivity across strike, however, will be low between the two main trough-going faults of the simple rift fault network (Fig. 6.5, stage 3). The low across strike connectivity may serve as a favour in a scenario where the faults are considered to act as a trap for hydrocarbons. A low across strike connectivity, may be a hindrance where faults are considered to be conduits in a fracture-dependent, low-permeability rock. The high connectivity along faults will serve as fluid conduits, while the areas with low connectivity (and damage) will not be swept. From a reservoir perspective, fracture intensities and connecting node frequencies could populate cells in a reservoir model. Additionally, the connectivity could be directly related to permeability both around faults and in host rock.

7 Conclusions and further work

7.1 Conclusions

This study has attempted to reveal the network properties of damage occurring around fault tips, splay faults and relay ramps. This was done by the use of traditional field data and topological characterisation of small-scale normal faults formed in carbonate rocks along the west coast of Malta. From the work presented in this study, the following conclusions are drawn:

- Fault tip damage zones can be divided into two stages based on their topology. Stage 1 fault tip damage zones are dominated by I-nodes and do not include X-nodes, hence they have low connectivity (<1.43 C_B). Stage 2 fault tip damage zones are dominated by Y-nodes, hence they show higher connectivity (1.58 - 1.62 C_B) than stage 1 fault tip damage zones.
- Splay fault damage zones show high degree of architectural variability and low variability in topology. They are dominated by Y-nodes and CC-branches and thus show medium connectivity (1.64 - 1.80 C_B).
- Relay damage zones are traditionally divided into 4 stages based on their development and are also reflected in their topology. Stage 2 relay damage zones shows a low connectivity, stage 3 have a medium connectivity and stage 4 show high connectivity (>1.80 C_B). This indicates that connectivity develops with maturity.
- Connectivity (and topology) of fault tip damage zones are similar to the connectivity of stage 2 relay damage zones, due to their propagating tips and bifurcating geometry, which results in the lowest connectivity of studied damage zones. Splay fault damage zones show similar connectivity as stage 3 relay damage zones due to linking/bifurcating segments, thus a medium connectivity. Stage 4 relay damage zones are the most complex linking damage zone and show the highest connectivity observed.
- Circle samples along strike/dip of damage zones show a strong correlation between fracture intensity, connecting node frequency and number of faces (blocks in 2D). Fracture intensity maps and connecting node frequency maps show that high values are restricted to areas of bifurcation and linkage. Hence,

bifurcation- and linkage areas will also show a high number of faces. These high connectivity zones could act as conduits for fluid flow.

- The studied damage zones are used as proxies for different stages of damage zone growth, where damage zones showing a low connectivity represent an immature stage and damage zone with a high connectivity represent a mature stage. This can be integrated in a three stage model (Fig. 6.5): Stage 1) initiation: during an early stage of rifting a high amount of isolated faults are formed. Each fault will include two fault tip damage zones and stage (1-) 2 relay damage zones are formed. This results in domination isolated nodes and partly connecting branches. The damage zones of the fault network therefore show a low connectivity. Stage 2) Interaction and linkage: as rifting continues, the faults within the fault network will increase their length and displacement, which leads to interactions and linkage between neighbouring fault segments. This leads to domination of stage 3 relay damage zones. This is reflected in the topology by an increase in connecting nodes and branches, resulting in a medium connectivity. Stage 3) through-going fault zones: strain is localised along a few through-going fault zones. This results in a domination of stage 4 relay damage zones the major faults and relatively constant damage along the inactive fault segments within stress shadows of major faults. This implies higher amounts of connecting nodes and branches causing a high connectivity at this stage.

7.2 Further work

This study manly focus on the damage occurring around complex normal fault settings as fault tips, relay zones and fault splays. It would be interesting to investigate the topology of other complex settings, as damage occurring around conjugate faults (crossing faults). Also, more simple settings should be investigated, as the topology of wall damage occurring around a single fault. Such investigation could add valuable information to the three stage rift model suggested in this study (Fig. 6.5). Additionally, it would be of interest to study more fault tip, relay and splay examples to investigate the overlap occurring in topology and connectivity of stage 1 and 2 fault tip damage zones and the overlap between the four stages of relay growth. These types of damage could also be documented larger scale faults, in compressional and strike slip settings, to investigate

similarities and/or differences in their topological character. Further documentation of topology and connectivity in damage zones could also be done in extensional plaster-experiments and for other lithologies with different strength.

Another interesting venue for further research would be to integrate the fracture intensity, connecting node frequency, number of faces and connectivity in reservoir models to relate them to the fluid flow in complex areas around faults. There is not much done on fault modelling, and the usual input would be fracture frequency, average fracture length and orientations. Fracture length could be replaced with branch length, which is much more precise, and the connectivity could be added to models. Additionally, analyses could be done to relate the studied parameters to the relative permeability in such structurally complex settings.

8 References

Aarland, R.K., Skjerven, J., 1998. Fault and fracture characteristics of a major fault zone in the northern North Sea: analysis of 3D seismic and oriented cores in the Brage Field (Block 31/4). Geological Society, London, Special Publications 127, 209-229.

Anderson, E.M., 1951. The Dynamics of Faulting (Revised.). Edinburgh, London.

Antonellini, M., Aydin, A., 1994. Effect of faulting on fluid flow in porous sandstones: petrophysical properties. AAPG Bulletin 78, 355-377.

Argnani, A., 1990. The Strait of Sicily rift zone: foreland deformation related to the evolution of a back-arc basin. Journal of Geodynamics 12, 311-331.

Aydin, A., Johnson, A.M., 1978. Development of faults as zones of deformation bands and as slip surfaces in sandstone, in: Byerlee, J.D., Wyss, M. (Eds.), Rock Friction and Earthquake Prediction. Springer, pp. 931-942.

Aydin, A., 2000. Fractures, faults, and hydrocarbon entrapment, migration and flow. Marine and Petroleum Geology 17, 797-814.

Aydin, A., Borja, R.I., Eichhubl, P., 2006. Geological and mathematical framework for failure modes in granular rock. Journal of Structural Geology 28, 83-98.

Barton, C.A., Zoback, M.D., 1994. Stress perturbations associated with active faults penetrated by boreholes: Possible evidence for near-complete stress drop and a new technique for stress magnitude measurement. Journal of Geophysical Research: Solid Earth 99, 9373-9390.

Bastesen, E., Braathen, A., Nøttveit, H., Gabrielsen, R.H., Skar, T., 2009. Extensional fault cores in micritic carbonate – Case studies from the Gulf of Corinth, Greece. Journal of Structural Geology 31, 403-420.

Bastesen, E., Rotevatn, A., 2012. Evolution and structural style of relay zones in layered limestone–shale sequences: insights from the Hammam Faraun Fault Block, Suez rift, Egypt. Journal of the Geological Society 169, 477-488.

Beach, A., Welbon, A.I., Brockbank, P.J., McCallum, J.E., 1999. Reservoir damage around faults: outcrop examples from the Suez rift. Petroleum Geoscience 5, 109-116.

Bennett, S.M., 1979. Palaeoenvironmental studies in maltese mid-tertiary carbonates. PhD thesis. Royal Holloway, University of London.

Berg, S.S., Skar, T., 2005. Controls on damage zone asymmetry of a normal fault zone: outcrop analyses of a segment of the Moab fault, SE Utah. Journal of Structural Geology 27, 1803-1822.

Boccaletti, S., Latora, V., Moreno, Y., Chavez, M., Hwang, D.U., 2006. Complex networks: Structure and dynamics. Physics Reports 424, 175-308.

Bolander, J.E., Saito, S., 1998. Fracture analyses using spring networks with random geometry. Engineering Fracture Mechanics 61, 569-591.

Bonson, C.G., Childs, C., Walsh, J.J., Schöpfer, M.P.J., Carboni, V., 2007. Geometric and kinematic controls on the internal structure of a large normal fault in massive limestones: The Maghlaq Fault, Malta. Journal of Structural Geology 29, 336-354.

Bosence, D.W.J., Pedley, H.M., 1982. Sedimentology and palaeoecology of a Miocene coralline algal biostrome from the Maltese Islands. Palaeogeography, Palaeoclimatology, Palaeoecology 38, 9-43.

Burollet, P.F., 1991. Structures and tectonics of Tunisia. Tectonophysics 195, 359-369.

Caine, J.S., Evans, J.P., Forster, C.B., 1996. Fault zone architecture and permeability structure. Geology 24, 1025-1028.

Calanchi, N., Colantoni, P., Rossi, P.L., Saitta, M., Serri, G., 1989. The Strait of Sicily continental rift systems: Physiography and petrochemistry of the submarine volcanic centres. Marine Geology 87, 55-83.

Carminati, E., Lustrino, M., Doglioni, C., 2012. Geodynamic evolution of the central and western Mediterranean: Tectonics vs. igneous petrology constraints. Tectonophysics 579, 173-192.

Cartwright, J.A., Trudgill, B.D., Mansfield, C.S., 1995. Fault growth by segment linkage: an explanation for scatter in maximum displacement and trace length data from the Canyonlands Grabens of SE Utah. Journal of Structural Geology 17, 1319-1326.

Cavazza, W., Wezel, F.C., 2003. The Mediterranean region-a geological primer. Episodes 26, 160-168.

Cello, G., Crisci, G.M., Marabini, S., Tortorici, L., 1985. Transtensive tectonics in the Strait of Sicily: structural and volcanological evidence from the island of Pantelleria. Tectonics 4, 311–322.

Cello, G., Tondi, E., Micarelli, L., Invernizzi, C., 2001. Fault zone fabrics and geofluid properties as indicators of rock deformation modes. Journal of Geodynamics 32, 543-565.

Chester, F., Logan, J., 1986. Implications for mechanical properties of brittle faults from observations of the Punchbowl fault zone, California. Pure and Applied Geophysics 124, 79-106.

Chester, F., Logan, J., 1987. Composite planar fabric of gouge from the Punchbowl fault, California. Journal of Structural Geology 9, 621-634.

Childs, C., Watterson, J., Walsh, J., 1995. Fault overlap zones within developing normal fault systems. Journal of the Geological Society 152, 535-549.

Childs, C., Watterson, J., Walsh, J., 1996. A model for the structure and development of fault zones. Journal of the Geological Society 153, 337-340.

Childs, C., Walsh, J.J., Watterson, J., 1997. Complexity in fault zone structure and implications for fault seal prediction, in: Møller-Pedersen, P., Koestler, A.G. (Eds.), Norwegian Petroleum Society Special Publications. Elsevier, pp. 61-72.

Childs, C., Manzocchi, T., Walsh, J.J., Bonson, C.G., Nicol, A., Schöpfer, M.P., 2009. A geometric model of fault zone and fault rock thickness variations. Journal of Structural Geology 31, 117-127.

Chinnery, M.A., 1966. Secondary faulting: II. Geological aspects. Canadian Journal of Earth Sciences 3, 175-190.

Choi, J.-H., Edwards, P., Ko, K., Kim, Y.-S., 2016. Definition and classification of fault damage zones: a review and a new methodological approach. Earth-Science Reviews 152, 70-87.

Civile, D., Lodolo, E., Accettella, D., Geletti, R., Ben-Avraham, Z., Deponte, M., Facchin, L., Ramella, R., Romeo, R., 2010. The Pantelleria graben (Sicily Channel, Central Mediterranean): an example of intraplate 'passive' rift. Tectonophysics 490, 173-183.

Corti, G., Bonini, M., Conticelli, S., Innocenti, F., Manetti, P., Sokoutis, D., 2003. Analogue modelling of continental extension: a review focused on the relations between the patterns of deformation and the presence of magma. Earth-Science Reviews 63, 169-247.

Corti, G., Cuffaro, M., Doglioni, C., Innocenti, F., Manetti, P., 2006. Coexisting geodynamic processes in the Sicily Channel. Geological Society of America Special Papers 409, 83-96.

Cowie, P.A., Scholz, C.H., 1992a. Growth of faults by accumulation of seismic slip. Journal of Geophysical Research: Solid Earth 97, 11085-11095.

Cowie, P.A., Scholz, C.H., 1992b. Displacement-length scaling relationship for faults: data synthesis and discussion. Journal of Structural Geology 14, 1149-1156.

Cowie, P.A., Scholz, C.H., 1992c. Physical explanation for the displacement-length relationship of faults using a post-yield fracture mechanics model. Journal of Structural Geology 14, 1133-1148.

Cowie, P.A., Shipton, Z.K., 1998. Fault tip displacement gradients and process zone dimensions. Journal of Structural Geology 20, 983-997.

Cowie, P.A., Gupta, S., Dawers, N., 2000. Implications of fault array evolution for synrift depocentre development: insights from a numerical fault growth model. Basin Research 12, 241-261.

Curewitz, D., Karson, J.A., 1997. Structural settings of hydrothermal outflow: Fracture permeability maintained by fault propagation and interaction. Journal of Volcanology and Geothermal Research 79, 149-168.

Dart, C.J., 1991. Carbonate sedimentation and extensional tectonics in the Maltese graben systems. Unpub. PhD thesis. Royal Holloway, University of London.

Dart, C.J., Bosence, D.W.J., McClay, K.R., 1993. Stratigraphy and structure of the Maltese graben system. Journal of the Geological Society 150, 1153-1166.

Davidson, J.R.J., Fairley, J., Nicol, A., Gravley, D., Ring, U., 2016. The origin of radon anomalies along normal faults in an active rift and geothermal area. Geosphere 13, 1656-1669.

de Visser, J.P., 1992. Clay mineral stratigraphy of Miocene to recent marine sediments in the central Mediterranean. Geologica Ultraiectina 75, 1-243.

Dershowitz, W.S., Einstein, H.H., 1988. Characterizing rock joint geometry with joint system models. Rock Mechanics and Rock Engineering 21, 21-51.

Dockrill, B., Shipton, Z.K., 2010. Structural controls on leakage from a natural CO2 geologic storage site: Central Utah, U.S.A. Journal of Structural Geology 32, 1768-1782.

Duffy, O.B., Nixon, C.W., Bell, R.E., Jackson, C.A., Gawthorpe, R.L., Sanderson, D.J., Whipp, P.S., in review. The Topology of Evolving Rift Fault Networks: Single-Phase vs Multi-Phase Rifts. Journal of Structural Geology.

Engelder, T., 1987. Joints and shear fractures in rock, in: Atkinson, B.K. (Ed.), Fracture Mechanics of Rock. Academic Press, New York, pp. 27-69.

Evans, J.P., 1990. Thickness-displacement relationships for fault zones. Journal of Structural Geology 12, 1061-1065.

Faulkner, D.R., Lewis, A.C., Rutter, E.H., 2003. On the internal structure and mechanics of large strike-slip fault zones: field observations of the Carboneras fault in southeastern Spain. Tectonophysics 367, 235-251.

Faulkner, D.R., Jackson, C.A.L., Lunn, R.J., Schlische, R.W., Shipton, Z.K., Wibberley, C.A.J., Withjack, M.O., 2010. A review of recent developments concerning the structure, mechanics and fluid flow properties of fault zones. Journal of Structural Geology 32, 1557-1575.

Felix, R., 1973. Oligo-Miocene stratigraphy of Malta and Gozo, in: Veenman, H. (Ed.), Department of Soil Science and Geology. Agricultural University, Wageningen, The Netherlands.

Ferrill, D.A., Morris, A.P., Stamatakos, J.A., Sims, D.W., 2000. Crossing conjugate normal faults. AAPG bulletin 84, 1543-1559.

Ferrill, D.A., Morris, A.P., 2008. Fault zone deformation controlled by carbonate mechanical stratigraphy, Balcones fault system, Texas. AAPG Bulletin 92, 359-380.

Finetti, I., 1984. Geophysical study of the Sicily Channel rift zone. Bollettino di Geofisica Teorica ed Applicata 26, 3-28.

Finetti, I., 1985. Structure and evolution of the central Mediterranean (Pelagian and Ionian Seas), in: Stanley, D.J., Wezel, F.-C. (Eds.), Geological Evolution of the Mediterranean Basin. Springer, New York, pp. 215-230.

Fossen, H., Hesthammer, J., 1998. Structural geology of the Gullfaks field, northern North Sea. Geological Society, London, Special Publications 127, 231-261.

Fossen, H., Hesthammer, J., 2000. Possible absence of small faults in the Gullfaks Field, northern North Sea: implications for downscaling of faults in some porous sandstones. Journal of Structural Geology 22, 851-863.

Fossen, H., Johansen, T.E.S., Hesthammer, J., Rotevatn, A., 2005. Fault interaction in porous sandstone and implications for reservoir management; examples from southern Utah. AAPG Bulletin 89, 1593-1606.

Fossen, H., Schultz, R.A., Shipton, Z.K., Mair, K., 2007. Deformation bands in sandstone: a review. Journal of the Geological Society 164, 755-769.

Fossen, H., 2010. Structural Geology. Cambridge University Press, Cambridge, pp. 119-148.

Fossen, H., Rotevatn, A., 2016. Fault linkage and relay structures in extensional settings—A review. Earth-Science Reviews 154, 14-28.

Fossmark, H.S.S., 2015. Petrophysical properties of deformation bands and their influence on fluid flow in carbonate grainstones: insights from the Maghlaq Fault, Malta. MSc thesis. University of Bergen.

Gawthorpe, R., Leeder, M., 2000. Tectono-sedimentary evolution of active extensional basins. Basin Research 12, 195-218.

Goddard, J.V., Evans, J.P., 1995. Chemical changes and fluid-rock interaction in faults of crystalline thrust sheets, northwestern Wyoming, USA. Journal of Structural Geology 17, 533-547.

Granath, J.W., Casero, P., 2004. Tectonic setting of the petroleum systems of Sicily, in: Swennen, R., Roure, F., Granath, J.W. (Eds.), Deformation, fluid flow and reservoir appraisal in foreland fold-and-thrust belts. AAPG Hedberg Series, pp. 391-411.

Grasso, M., Reuther, C.-D., Baumann, H., Becker, A., 1986. Shallow crustal stress and neotectonic framework of the Malta Platform and the Southeastern Pantelleria Rift (Central Mediterranean). Geologica Romana 25, 191-212.

Grauls, D., Pascaud, F., Rives, T., 2002. Quantitative fault seal assessment in hydrocarbon-compartmentalised structures using fluid pressure data, in: Andreas, G.K., Robert, H. (Eds.), Norwegian Petroleum Society Special Publications. Elsevier, pp. 141-156.

Gudmundsson, A., Simmenes, T.H., Larsen, B., Philipp, S.L., 2010. Effects of internal structure and local stresses on fracture propagation, deflection, and arrest in fault zones. Journal of Structural Geology 32, 1643-1655.

Gueguen, E., Doglioni, C., Fernandez, M., 1998. On the post-25 Ma geodynamic evolution of the western Mediterranean. Tectonophysics 298, 259-269.

Gupta, A., Scholz, C.H., 2000. A model of normal fault interaction based on observations and theory. Journal of Structural Geology 22, 865-879.

Hill, K.C., Hayward, A.B., 1988. Structural constraints on the Tertiary plate tectonic evolution of Italy. Marine and Petroleum Geology 5, 2-16.

Huang, Q., Angelier, J., 1989. Fracture spacing and its relation to bed thickness. Geological Magazine 126, 355-362.

Huggins, P., Watterson, J., Walsh, J.J., Childs, C., 1995. Relay zone geometry and displacement transfer between normal faults recorded in coal-mine plans. Journal of Structural Geology 17, 1741-1755.

Hull, J., 1988. Thickness-displacement relationships for deformation zones. Journal of Structural Geology 10, 431-435.

Illies, J., 1980. Graben formation - the Maltese Islands. Tectonophysics 73, 151-168.

Imber, J., Tuckwell, G.W., Childs, C., Walsh, J.J., Manzocchi, T., Heath, A.E., Bonson, C.G., Strand, J., 2004. Three-dimensional distinct element modelling of relay growth and breaching along normal faults. Journal of Structural Geology 26, 1897-1911.

Jongsma, D., van Hinte, J.E., Woodside, J.M., 1985. Geologic structure and neotectonics of the North African Continental Margin south of Sicily. Marine and Petroleum Geology 2, 156-179.

Kattenhorn, S.A., Aydin, A., Pollard, D.D., 2000. Joints at high angles to normal fault strike: an explanation using 3-D numerical models of fault-perturbed stress fields. Journal of Structural Geology 22, 1-23.

Kim, Y.-S., Peacock, D.C.P., Sanderson, D.J., 2004. Fault damage zones. Journal of Structural Geology 26, 503-517.

Ladeira, F., Price, N., 1981. Relationship between fracture spacing and bed thickness. Journal of Structural Geology 3, 179-183.

Larsen, P.-H., 1988. Relay structures in a Lower Permian basement-involved extension system, East Greenland. Journal of Structural Geology 10, 3-8.

Latora, V., Marchiori, M., 2002. Is the Boston subway a small-world network? Physica A: Statistical Mechanics and its Applications 314, 109-113.

Laubach, S.E., 1988. Subsurface fractures and their relationship to stress history in East Texas basin sandstone. Tectonophysics 156, 37-49.

Laubach, S.E., 1992. Fracture networks in selected Cretaceous sandstones of the Green River and San Juan basins, Wyoming, New Mexico, and Colorado, in: J. W. Schntoker, E.B.C., C. A. Brown (Ed.), Geological studies relevant to horizontal drilling: Examples from Western North America: Rocky Mountain Association of Geologists, pp. 115-127.

Lewis, H., Olden, P., Couples, G.D., 2002. Geomechanical simulations of top seal integrity, in: Andreas, G.K., Robert, H. (Eds.), Norwegian Petroleum Society Special Publications. Elsevier, pp. 75-87.

Manzocchi, T., 2002. The connectivity of two-dimensional networks of spatially correlated fractures. Water Resources Research 38, 1-20.

Marciniak, Z., Kuczyński, K., 1967. Limit strains in the processes of stretch-forming sheet metal. International Journal of Mechanical Sciences 9, 609-620.

Martel, S.J., 1990. Formation of compound strike-slip fault zones, Mount Abbot quadrangle, California. Journal of Structural Geology 12, 869-882.

Mauldon, M., Dunne, W.M., Rohrbaugh, M.B., 2001. Circular scanlines and circular windows: new tools for characterizing the geometry of fracture traces. Journal of Structural Geology 23, 247-258.

Mazzei, R., 1985. The Miocene sequence of the Maltese Islands: biostratigraphic and chronostratigraphic references based on nannofossils. Atti della Societa Toscana di Scienze Naturali Residente in Pisa, Memorie, Processi Verbali, Serie A 92, 165-197.

McGrath, A.G., Davison, I., 1995. Damage zone geometry around fault tips. Journal of Structural Geology 17, 1011-1024.

McKinstry, H.E., 1953. Shears of the second order. American Journal of Science 251, 401-414.

Meyer, V., Nicol, A., Childs, C., Walsh, J.J., Watterson, J., 2002. Progressive localisation of strain during the evolution of a normal fault population. Journal of Structural Geology 24, 1215-1231.

Micallef, A., Foglini, F., Le Bas, T., Angeletti, L., Maselli, V., Pasuto, A., Taviani, M., 2013. The submerged paleolandscape of the Maltese Islands: morphology, evolution and relation to Quaternary environmental change. Marine Geology 335, 129-147.

Micarelli, L., Benedicto, A., Wibberley, C.A.J., 2006. Structural evolution and permeability of normal fault zones in highly porous carbonate rocks. Journal of Structural Geology 28, 1214-1227.

Michie, E.A.H., Haines, T.J., Healy, D., Neilson, J.E., Timms, N.E., Wibberley, C.A.J., 2014. Influence of carbonate facies on fault zone architecture. Journal of Structural Geology 65, 82-99.

Missenard, Y., Bertrand, A., Vergély, P., Benedicto, A., Cushing, M.-E., Rocher, M., 2014. Fracture-fluid relationships: implications for the sealing capacity of clay layers–Insights from field study of the Blue Clay formation, Maltese islands. Bulletin de la Societe Geologique de France 185, 51-63.

Mitchell, T.M., Faulkner, D.R., 2009. The nature and origin of off-fault damage surrounding strike-slip fault zones with a wide range of displacements: a field study from the Atacama fault system, northern Chile. Journal of Structural Geology 31, 802-816.

Morelli, C., Gantar, C., Pisani, M., 1975. Bathymetry, gravity and magnetism in the Strait of Sicily and in the Ionian Sea. Bollettino di Geofisica. Teorica ed Applicata 17, 39-58.

Morley, C.K., Nixon, C.W., 2016. Topological characteristics of simple and complex normal fault networks. Journal of Structural Geology 84, 68-84.

Morris, T.O., 1952. The water resources of Malta. Valletta, Malta: Government Printing Office, 1-125.

Murray, J., 1890. The Maltese Islands, with special reference to their geological structure: with geological map, two lithographic plates, and woodcuts. The Scottish Geographical Magazine 6, 449-488.

Nicol, A., Walsh, J., Watterson, J., Underhill, J., 1997. Displacement rates of normal faults. Nature 390, 157-159.

Nixon, C.W., Sanderson, D.J., Bull, J.M., 2012. Analysis of a strike-slip fault network using high resolution multibeam bathymetry, offshore NW Devon U.K. Tectonophysics 541–543, 69-80.

Nixon, C.W., 2013. Analysis of fault networks and conjugate systems. PhD thesis. University of Southampton.

Ogata, K., Senger, K., Braathen, A., Tveranger, J., 2014. Fracture corridors as seal-bypass systems in siliciclastic reservoir-cap rock successions: Field-based insights from the Jurassic Entrada Formation (SE Utah, USA). Journal of Structural Geology 66, 162-187.

Ortega, O., Marrett, R., 2000. Prediction of macrofracture properties using microfracture information, Mesaverde Group sandstones, San Juan basin, New Mexico. Journal of Structural Geology 22, 571-588.

Peacock, D.C.P., Sanderson, D.J., 1991. Displacements, segment linkage and relay ramps in normal fault zones. Journal of Structural Geology 13, 721-733.

Peacock, D.C.P., Sanderson, D.J., 1994. Geometry and development of relay ramps in normal fault system. AAPG Bulletin 78, 147-165.

Peacock, D.C.P., Nixon, C.W., Rotevatn, A., Sanderson, D.J., Zuluaga, L.F., 2016. Glossary of fault and other fracture networks. Journal of Structural Geology 92, 12-29.

Pedley, H.M., House, M.R., Waugh, B., 1976. The geology of Malta and Gozo. Proceedings of the Geologists' Association 87, 325-341.

Pedley, H.M., 1987a. The Ghar Lapsi limestones: sedimentology of a Miocene intra-shelf graben. Centro 1, 1-14.

Pedley, H.M., 1987b. Controls on Cenozoic carbonate deposition in the Maltese Islands: review and reinterpretation. Memorie della Societa Geologica Italiana 38, 81-94.

Pedley, H.M., 1990. Syndepositional tectonics affecting Cenozoic and Mesozoic deposition in the Malta and SE Sicily areas (Central Mediterranean) and their bearing on Mesozoic reservoir development in the N Malta offshore region. Marine and Petroleum Geology 7, 171-180.

Perrin, C., Manighetti, I., Gaudemer, Y., 2016. Off-fault tip splay networks: A genetic and generic property of faults indicative of their long-term propagation. Comptes Rendus Geoscience 348, 52-60.

Petit, J.P., Barquins, M., 1988. Can natural faults propagate under mode II conditions? Tectonics 7, 1243-1256.

Priest, S., Hudson, J., 1976. Discontinuity spacings in rock. International Journal of Rock Mechanics and Mining Sciences & Geomechanics Abstracts 13, 135-148.

Randolph, L., Johnson, B., 1989. Influence of faults of moderate displacement on groundwater flow in the Hickory sandstone aquifer in central Texas, Geological Society of America Abstracts with Programs, p. 242.

Ravasz, E., Barabási, A.-L., 2003. Hierarchical organization in complex networks. Physical Review E 67, 026112.

Rawnsley, K.D., Rives, T., Petti, J.P., Hencher, S.R., Lumsden, A.C., 1992. Joint development in perturbed stress fields near faults. Journal of Structural Geology 14, 939-951.

Rehault, J., Mascle, J., Boillot, G., 1984. Evolution géodynamique de la Méditerranée depuis l'Oligocene. Memorie della Società Geoligica Italiana 27, 85-96.

Reuther, C.-D., Eisbacher, G.H., 1985. Pantelleria Rift — crustal extension in a convergent intraplate setting. Geologische Rundschau 74, 585-597.

Richeson, D.S., 2012. Euler's gem: the polyhedron formula and the birth of topology. Princeton University Press.

Rives, T., Razack, M., Petit, J.-P., Rawnsley, K., 1992. Joint spacing: analogue and numerical simulations. Journal of Structural Geology 14, 925-937.

Robertson, A.H.F., Dixon, J.E., 1984. Introduction: aspects of the geological evolution of the Eastern Mediterranean. Geological Society, London, Special Publications 17, 1-74.

Robertson, A.H.F., Grasso, M., 1995. Overview of the Late Tertiary–Recent tectonic and palaeo-environmental development of the Mediterranean region. Terra Nova 7, 114-127.

Rosenbaum, G., Lister, G.S., Duboz, C., 2002. Reconstruction of the tectonic evolution of the western Mediterranean since the Oligocene. Journal of the Virtual Explorer 8, 107-130.

Rotevatn, A., Fossen, H., Hesthammer, J., Aas, T.E., Howell, J.A., 2007. Are relay ramps conduits for fluid flow? Structural analysis of a relay ramp in Arches National Park, Utah. Geological Society, London, Special Publications 270, 55-71.

Rotevatn, A., Bastesen, E., 2014. Fault linkage and damage zone architecture in tight carbonate rocks in the Suez Rift (Egypt): implications for permeability structure along segmented normal faults. Geological Society, London, Special Publications 374, 79-95.

Sanderson, D.J., Nixon, C.W., 2015. The use of topology in fracture network characterization. Journal of Structural Geology 72, 55-66.

Scholz, C., Anders, M., 1994. The permeability of faults, in: S. Hickman, R.S., and R. Bruhn (Ed.), The Mechanical Involvement of Fluids in Faulting, U.S. Geological Survey Open-File Report, pp. 94-228.

Segall, P., Pollard, D., 1980. Mechanics of discontinuous faults. Journal of Geophysical Research: Solid Earth 85, 4337-4350.

Sibson, R., 1977. Fault rocks and fault mechanisms. Journal of the Geological Society, London 133, 191-213.

Sibson, R.H., 1996. Structural permeability of fluid-driven fault-fracture meshes. Journal of Structural Geology 18, 1031-1042.

Smith, L., Forster, C., Evans, J.P., 1990. Interaction between fault zones, fluid flow and heat transfer at the basin scale, in: Newman, S.P., Neretnieks, I. (Eds.), Hydrogeology of Low Permeability Environments. International Association of Hydrological Sciences, pp. 41-67.

Tamagawa, T., Pollard, D.D., 2008. Fracture permeability created by perturbed stress fields around active faults in a fractured basement reservoir. AAPG bulletin 92, 743-764.

Trechmann, C., 1938. Quaternary conditions in Malta. Geological Magazine 75, 1-26.

Vermilye, J.M., Scholz, C.H., 1998. A microstructural view of fault growth. Journal of Geophysical Research 103, 12223-12237.

Walsh, J.J., Watterson, J., 1988. Analysis of the relationship between displacements and dimensions of faults. Journal of Structural Geology 10, 239-247.

Walsh, J.J., Watterson, J., 1991. Geometric and kinematic coherence and scale effects in normal fault systems. Geological Society, London, Special Publications 56, 193-203.

Walsh, J.J., Watterson, J., Bailey, W., Childs, C., 1999. Fault relays, bends and branch-lines. Journal of Structural Geology 21, 1019-1026.

Walsh, J.J., Childs, C., Meyer, V., Manzocchi, T., Imber, J., Nicol, A., Tuckwell, G., Bailey, W.R., Bonson, C.G., Watterson, J., 2001. Geometric controls on the evolution of normal fault systems. Geological Society, London, Special Publications 186, 157-170.

Walsh, J.J., Bailey, W.R., Childs, C., Nicol, A., Bonson, C.G., 2003. Formation of segmented normal faults: a 3-D perspective. Journal of Structural Geology 25, 1251-1262.

Willemse, E.J.M., Pollard, D.D., Aydin, A., 1996. Three-dimensional analyses of slip distributions on normal fault arrays with consequences for fault scaling. Journal of Structural Geology 18, 295-309.

Willemse, E.J.M., Pollard, D.D., 1998. On the orientation and patterns of wing cracks and solution surfaces at the tips of a sliding flaw or fault. Journal of Geophysical Research: Solid Earth 103, 2427-2438.

Woods, E., 1992. Vulcan Sub-basin fault styles-implications for hydrocarbon migration and entrapment. Australian Petroleum Production and Exploration Assosciation Journal 32, 138-138.

Wu, H., Pollard, D.D., 1995. An experimental study of the relationship between joint spacing and layer thickness. Journal of Structural Geology 17, 887-905.

Appendix I – Workflow in ArcGIS 10.3.1 and Excel

This section will go through the workflow in ArcGIS and Excel of one locality (i.e. one fault damage zone):

1. Go to ArcCatalog and create a folder, within the folder create a new geodatabase (.gdb). This folder is used for layers (.lyr) and maps (.mxd) and the geodatabase is used for saving and organising of feature classes.
2. Create a new map in ArcMap, right click on the map and select your "data frame properties", here the preferred coordinate system is selected.
3. Use the "add data" tab to add a photograph of the locality, make sure north is directed upwards. A warning box "Unknown Spatial Reference" box will appear, click OK. Thereafter, use Customize > Toolbars > Georeferencing. Then "Add Control Points" from the georeferencing toolbar. Add control points to give the photograph the right scale, "Save" the links to a text file from the "View Link Table" and click Georeferencing > Rectify… and save the photograph as a .tif-file in the folder. Finally, use the "Add data" and add you georectified photo (.tif).
4. Go to ArcToolbox > Data Management Tools > Feature Class > Create Feature Class. Here the I-, Y-, X-, and E-nodes are created as POINTs, II-, IC, CC- and U-branches are created as POLYLINESs, and the sample area as POLYGON. The feature classes are saved separately in the geoldatabase (.gdb). Make sure to ENABLE M and Z and select the same coordinate system as your map.

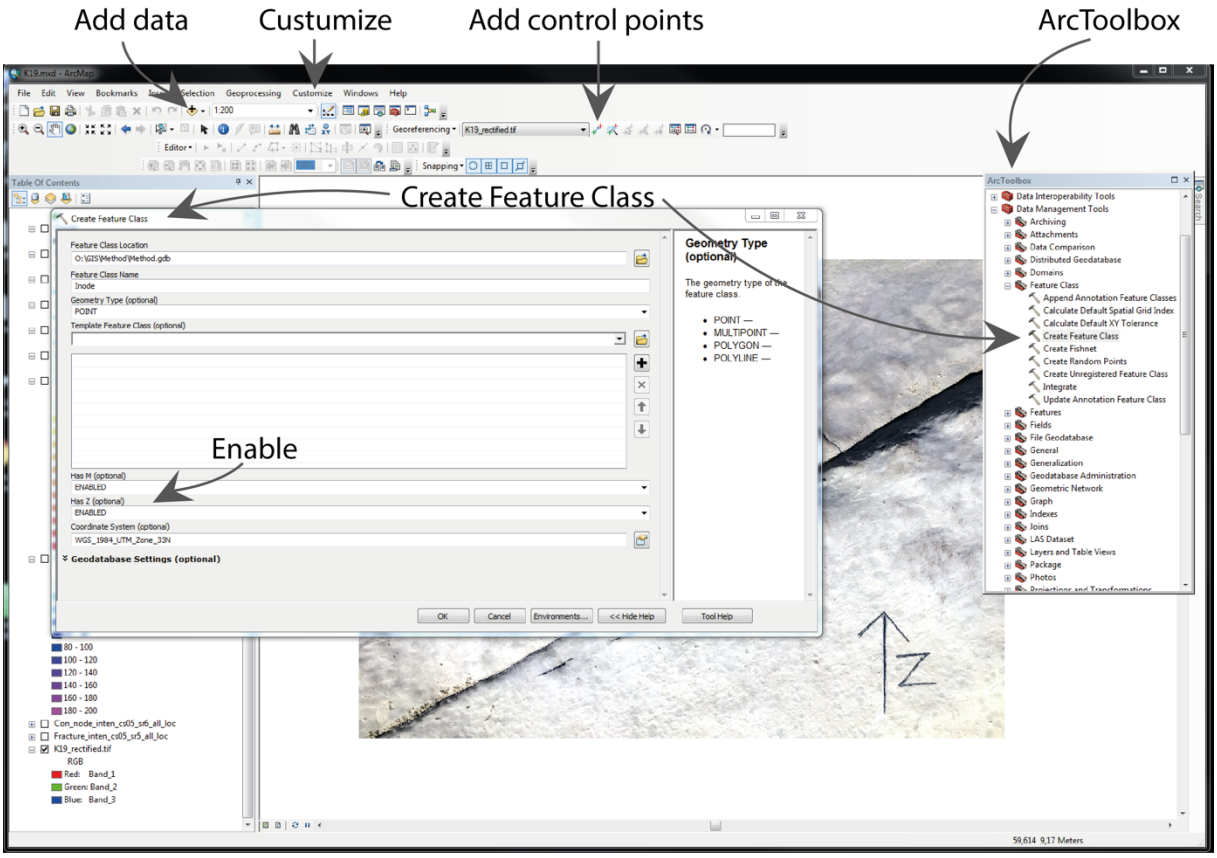

5. Double click on the feature classes in the "Table of Content" to change their "symbology"
    - I-node = green circle, Y-node = red triangle, X = blue square
    - II-branch = grey line, IC-branch = green line, CC-branch = blue line
6. Click editor>start editing and draw all nodes and branches based on the photograph, make sure the "Snapping" tool is used to get exact start- and end-points to the branches relative to nodes and other brancjes. If the branches stretching outside the photograph is unknown, it is important to draw it as a U-node, as it needs to be included in the total trace length for further calculations.
7. Right click on the branches in "Table of Contents" and open the attribute table. The "shape length" of branches is already present. Use the Table Option > Add Field. Field for Xstart, Xend, Ystart and Yend are created as the type "Double". The coordinates are calculated by right clicking the field and "Calculate Geometry". The coordinate for the braches are extracted and later used to create length weighted rose-diagrams. X- and Y-coordinates are also calculated for all node types.

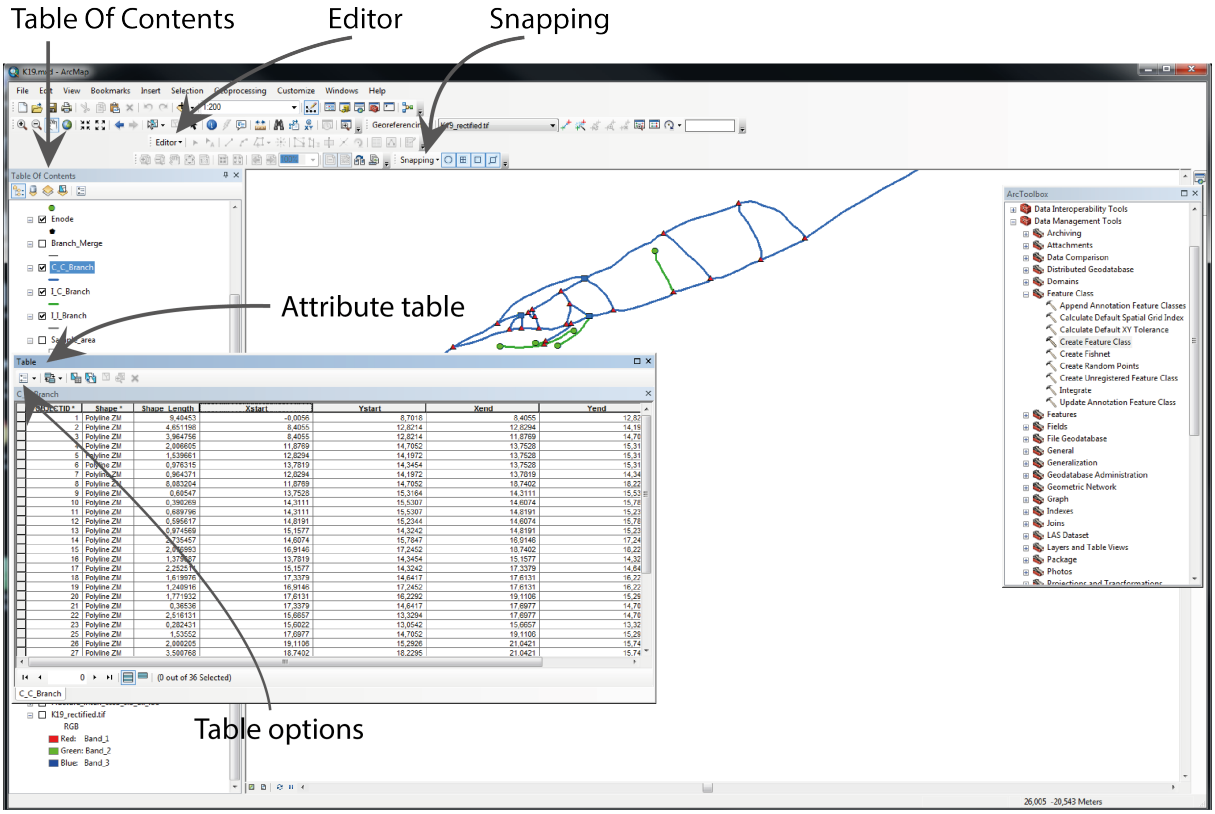

8. "Select" all the created features drawn on the photo and use the attribute table (for each node-and branch type) to extract the number of nodes and branches to the Excel spreadsheet. Additionally, the trace lengths for all branches is summarised in Excel by the use of the "Statistics" tool in the Attribute Table for each branch type. Finally, the sample are (m^2) gained from the sample area feature class attribute table are added into the Excel spreadsheet.

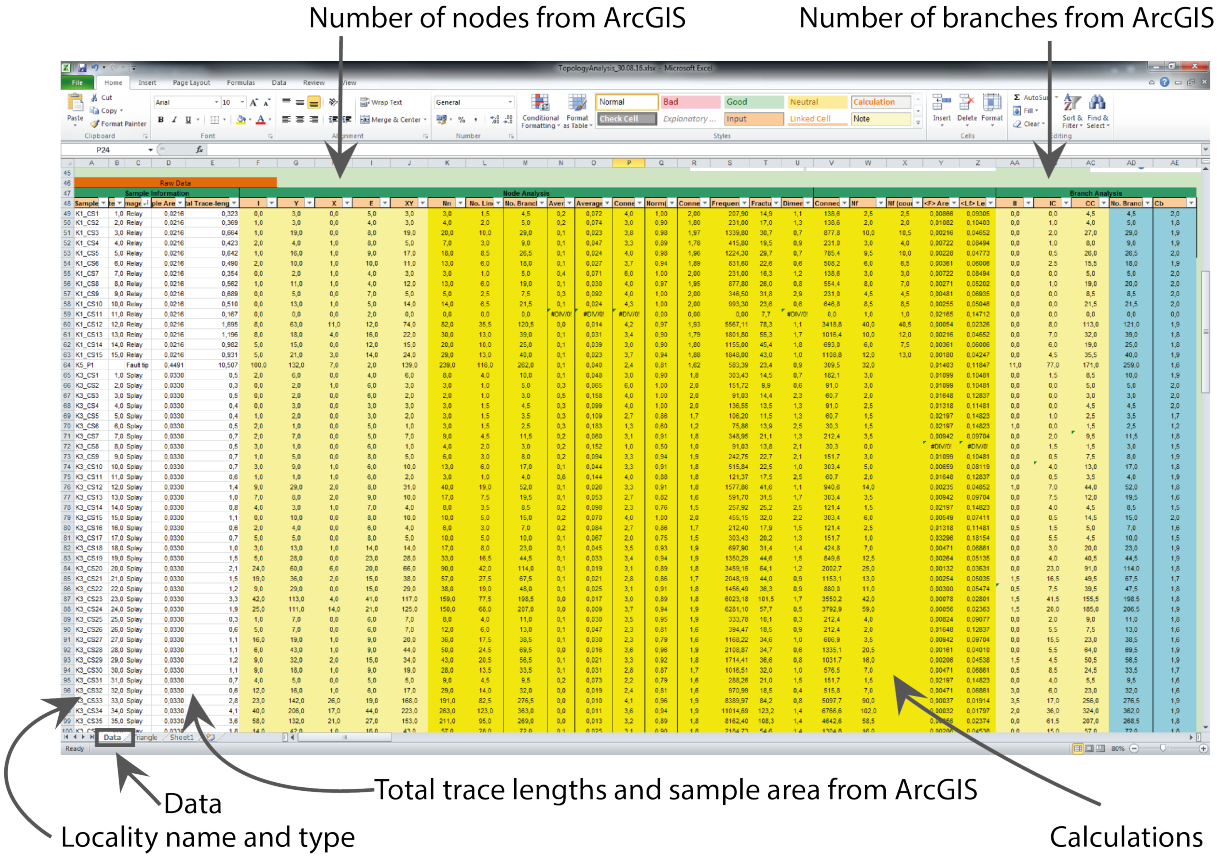

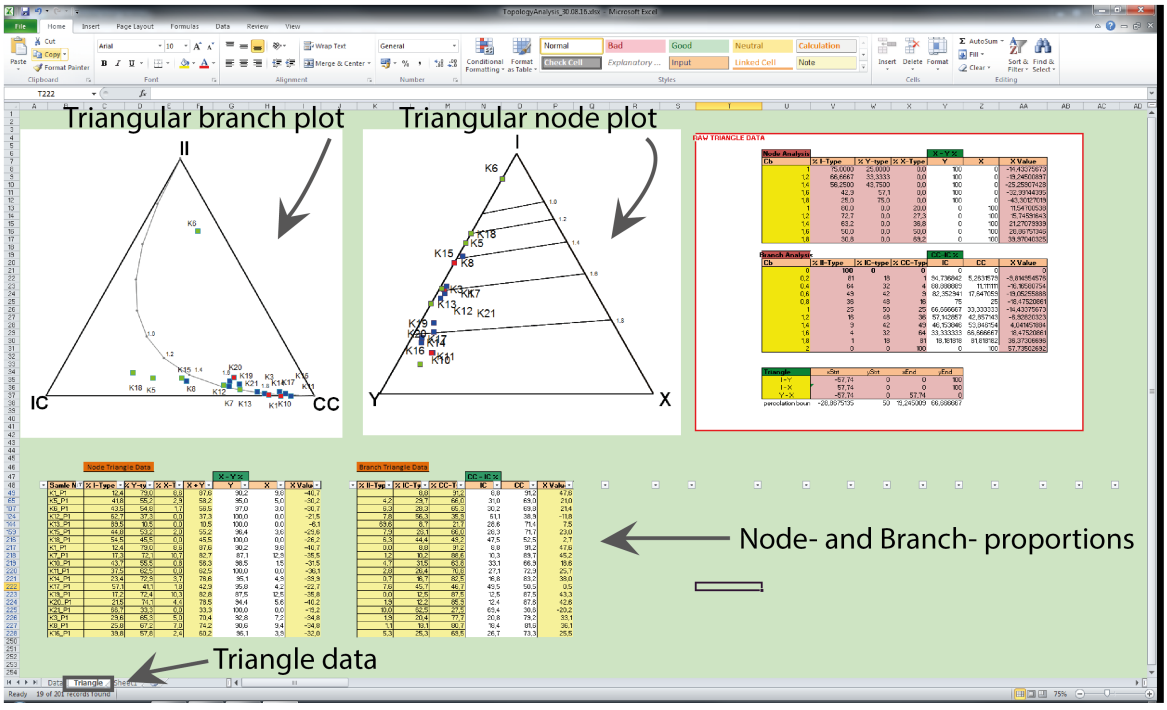

9. Go to ArcToolbox > Data Management Tools > General > Merge. Use Y- and X-node feature classes as input and merge them to a new feature class. This is the connecting nodes which is used to create connecting node frequency map (step 10). Use all branches as input and merge them for a new feature class. This is all the branches, and are used to create fracture intensity maps.

10. Go to ArcToolbox > Spatial Analyst Tools > Density > Kernel Density. Use the merged connecting nodes feature class as input. In “output raster”, navigate to the geodatabase and name the raster with the selected cell size and search radius. Area units = SQUARE_METERS, output value = DENSITIES and the Method = PLANAR. The output raster will be the connecting node frequency map. The same procedure is used for the fracture intensity map, where the merged braches are used as input.

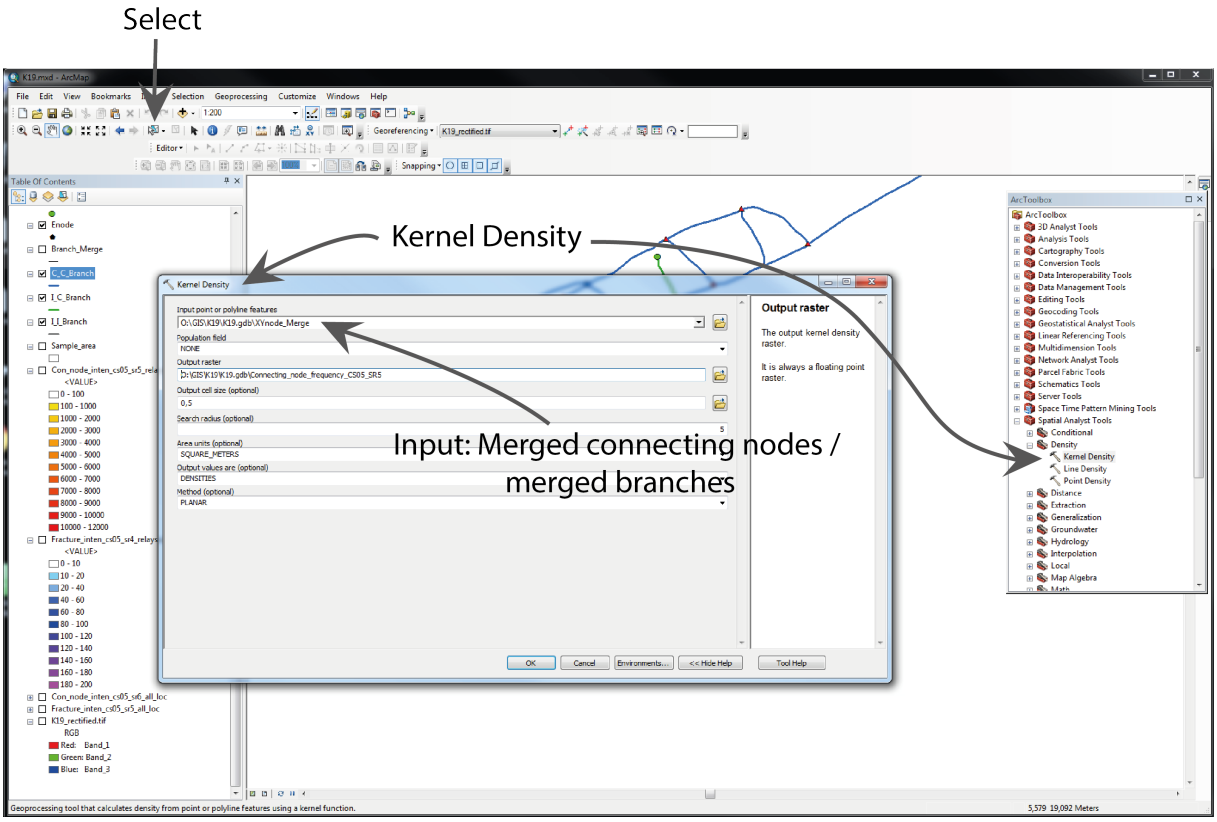

11. The scale is changed to create similar scale for all localities. This is done by double-clicking the raster in the “Table Of Contents” and the “Layer Properties” box will appear. Here, the “Symbology” is changed and the number of classes and the range of the classes are selected by use of the “classify” tab.

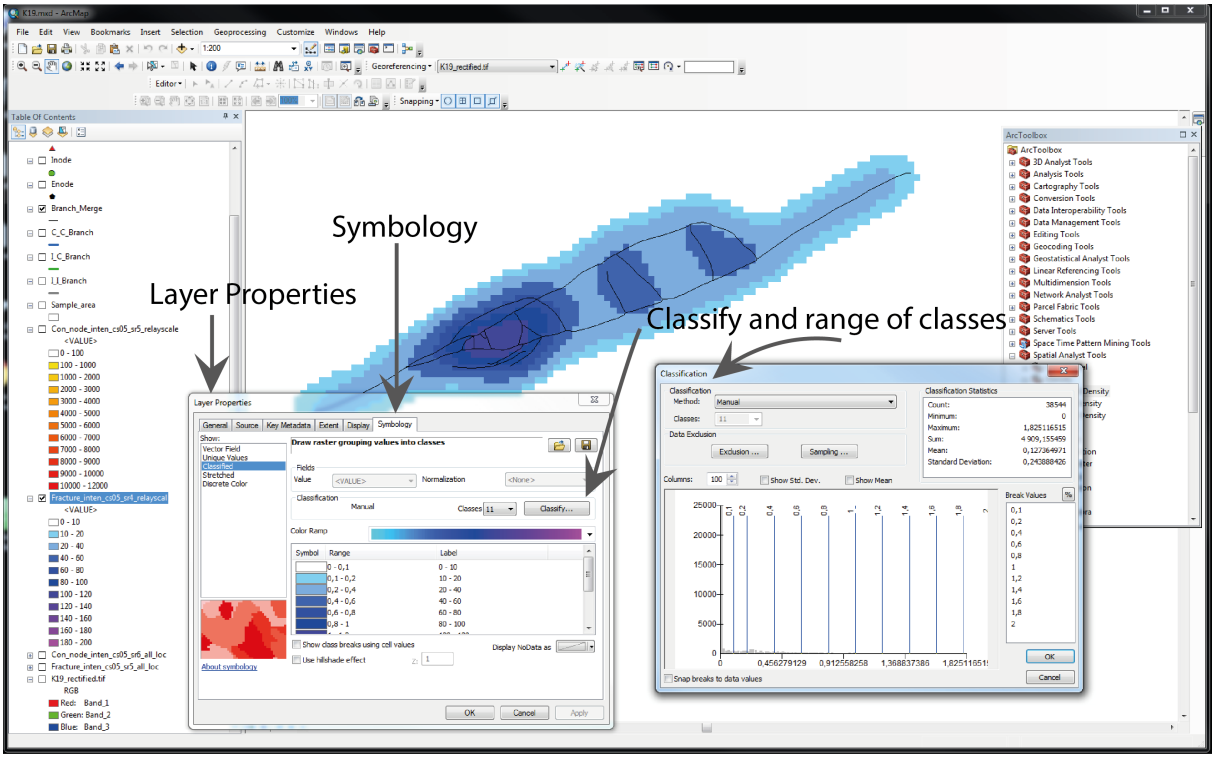

Circle samples

12. Create a new Geodatabase (.gdb) in ArcCatalog and copy all the node- and branch-feature classes into the new circle_sample.gdb. Create a new map and add all the feature classes into the map.
13. Create a new sample area feature class (step 4, polygon) for the circle samples. “Start Editing” and draw a circular polygon. Copy this circle and place them along strike/dip of the fault. Thereafter, name the circles with numbers in the attribute table.

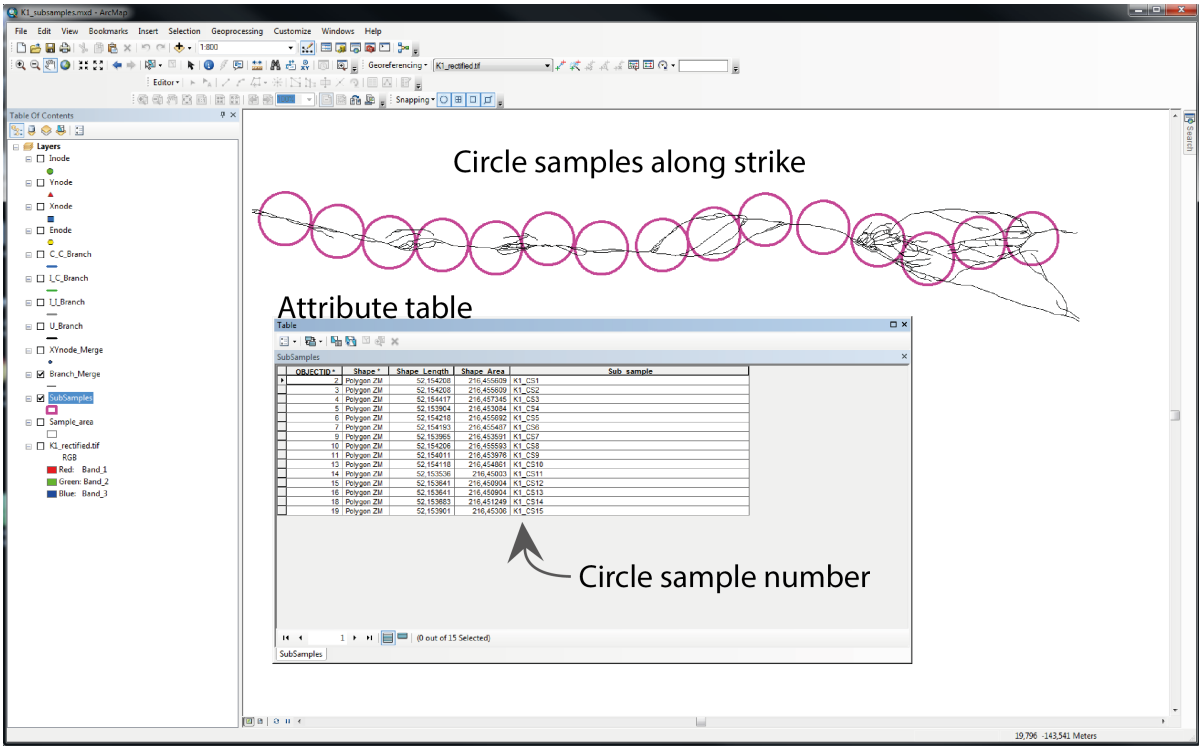

14. “Start Editing” and draw E-nodes where the braches intersect the circle. Delete the braches and redraw them to stop at the circle sample, use the merged branches to navigate the redrawn branches.
15. Summarise nodes, branches, sample area and total trace length (step 8) for each circle. Remember to subtract a half branch of each branch limited by an E-node at the circle sample, for each branch type when extracting data to Excel.

Appendix II – Localities and maps

This section includes an overview of the localities not included in the results chapter (Section 5). The last two figures are important A3 fold-out figures. Fold-out figure 1) showing the fracture intensity maps in similar scale for all studied damage zones and the associated topology of the localities. Fold-out figure 2) showing the connecting node frequency maps in similar scale for all studied damage zones and the associated topology of the localities.

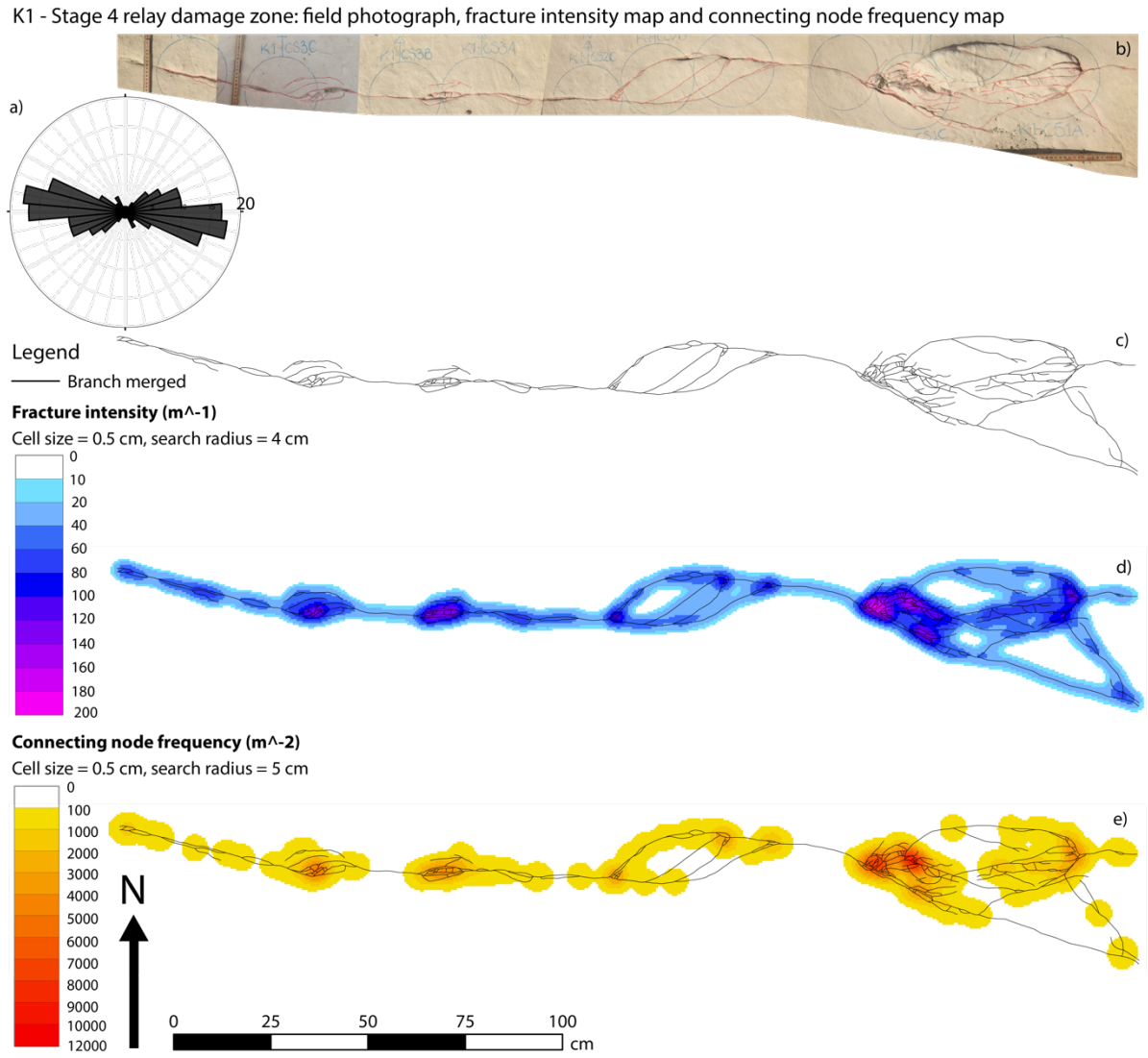

Figure AII.1: a) Rose diagram, including length-weighted strikes of all branches within the locality. b) Field photograph, c) branches, d) fracture intensity map and e) connecting node frequency map of K1. K1 is a small-scale normal fault including 4 relays along strike. It is exposed in the Middle Globigerina Limestone Member (MGLM).

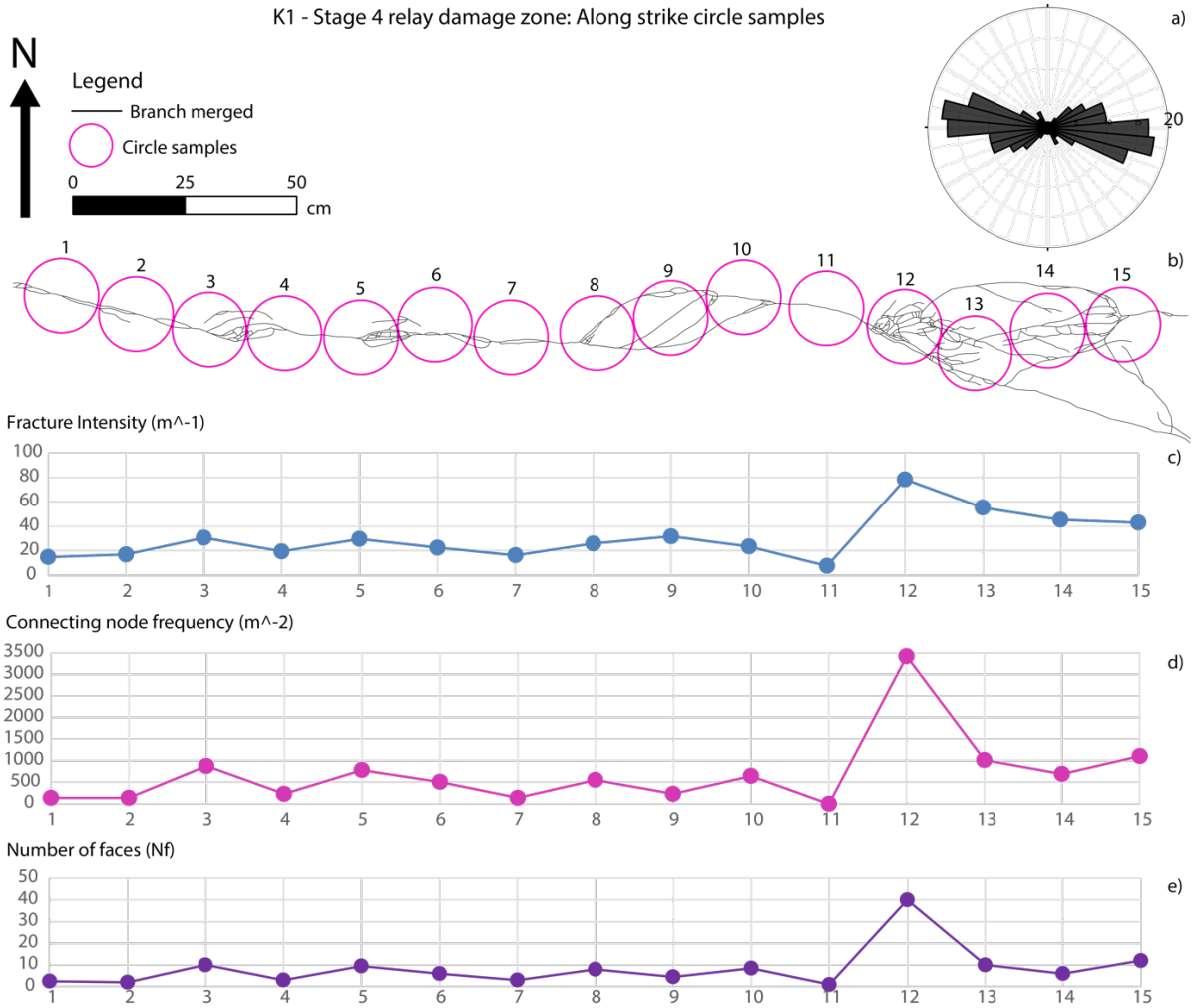

Figure AII.2: a) Rose diagram, including length-weighted strikes of all branches within the locality. b) Mapped branches of K1 with circle samples along strike of the normal fault. c) Graph of fracture intensities. d) Graph of connecting node frequency. e) Graph of number of faces within the circles.

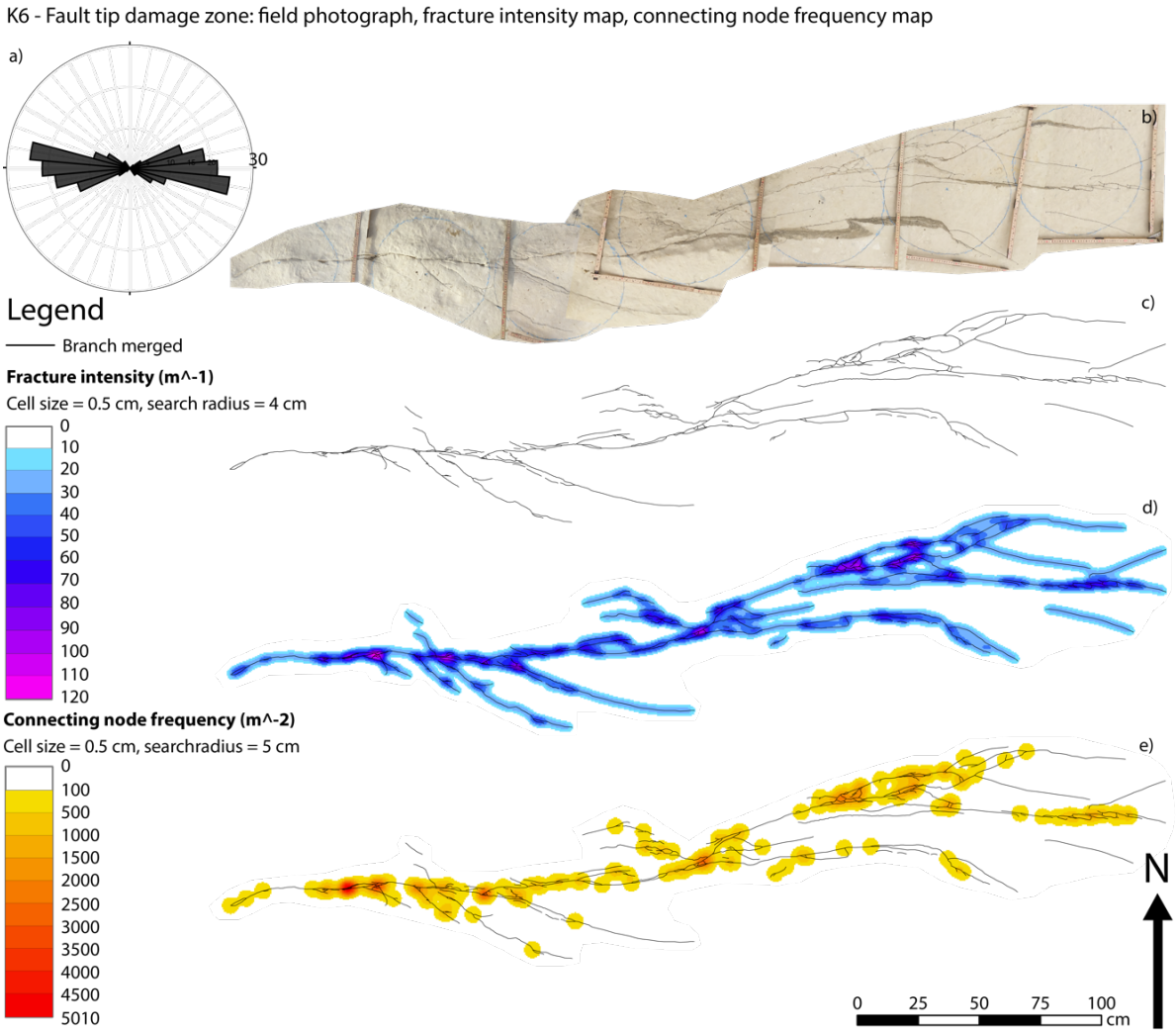

Figure AII.3: a) Rose diagram, including length-weighted strikes of all branches within the locality. b) Field photograph, c) branches, d) fracture intensity map and e) connecting node frequency map of K6. K6 is a normal fault tip damage zone exposed in the MGLM.

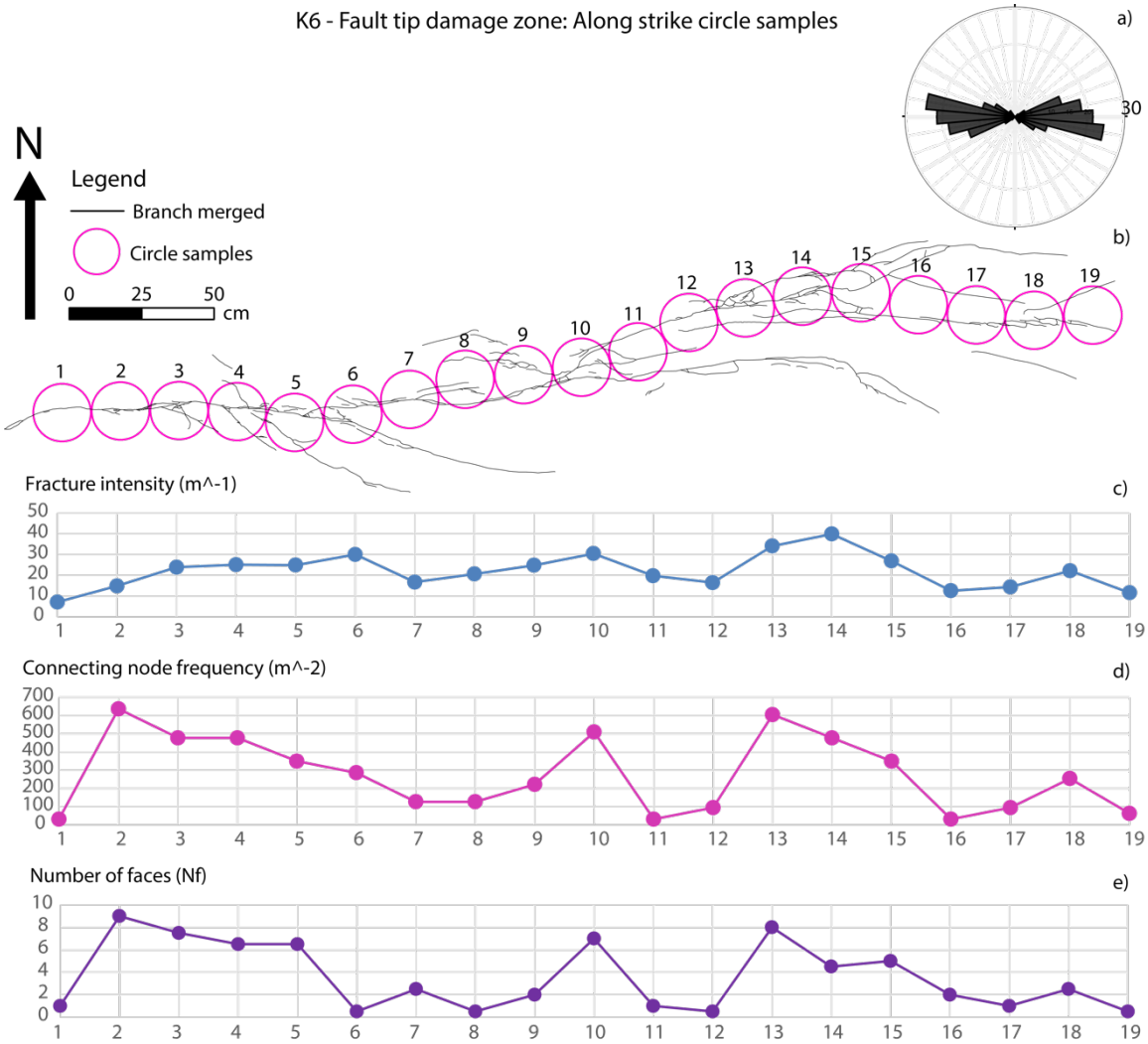

Figure AII.4: a) Rose diagram, including length-weighted strikes of all branches within the locality. b) Mapped branches of K6 with circle samples along strike of the normal fault. c) Graph of fracture intensities. d) Graph of connecting node frequency. e) Graph of number of faces within the circles.

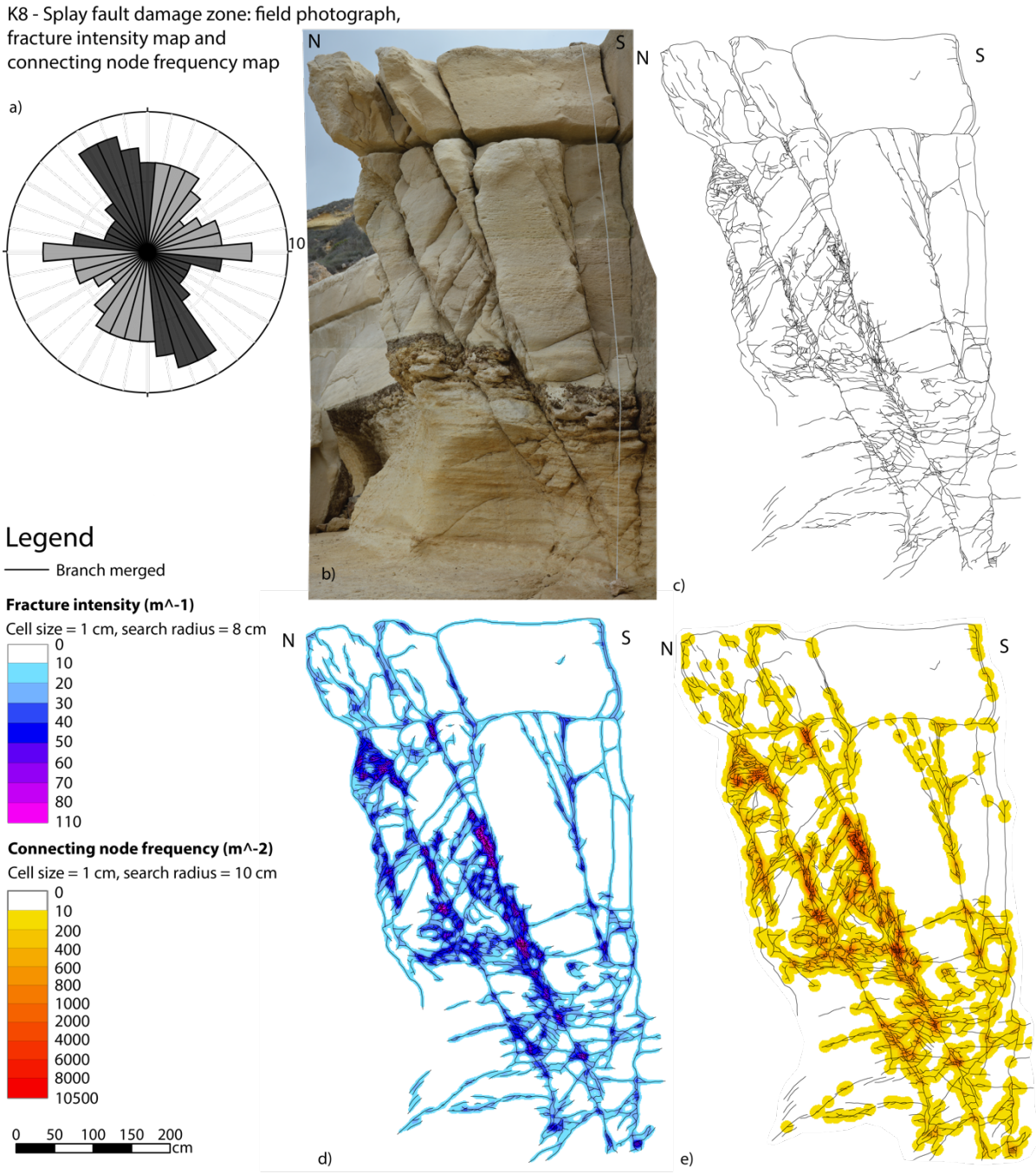

Figure AII.5: a) Rose diagram, including length-weighted dips of all branches within the locality. b) Field photograph, c) branches, d) fracture intensity map and e) connecting node frequency map of K8. K8 is a normal fault splay damage zone exposed in the LGLM and MGLM.

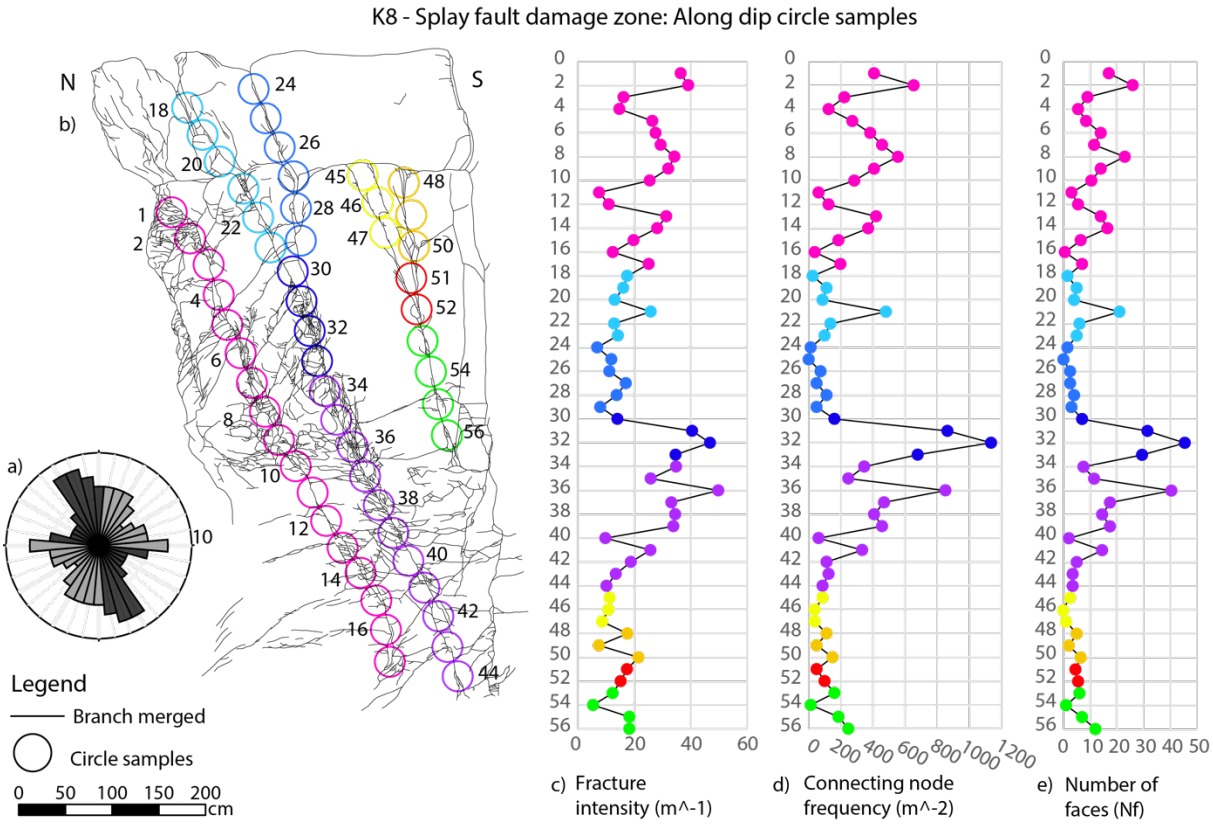

Figure AII.6: a) Rose diagram, including length-weighted dips of all branches within the locality. b) Mapped branches of K8 with circle samples along dip of the normal fault. c) Fracture intensities, d) connecting node frequency and e) number of faces within the circle is presented in graphs.

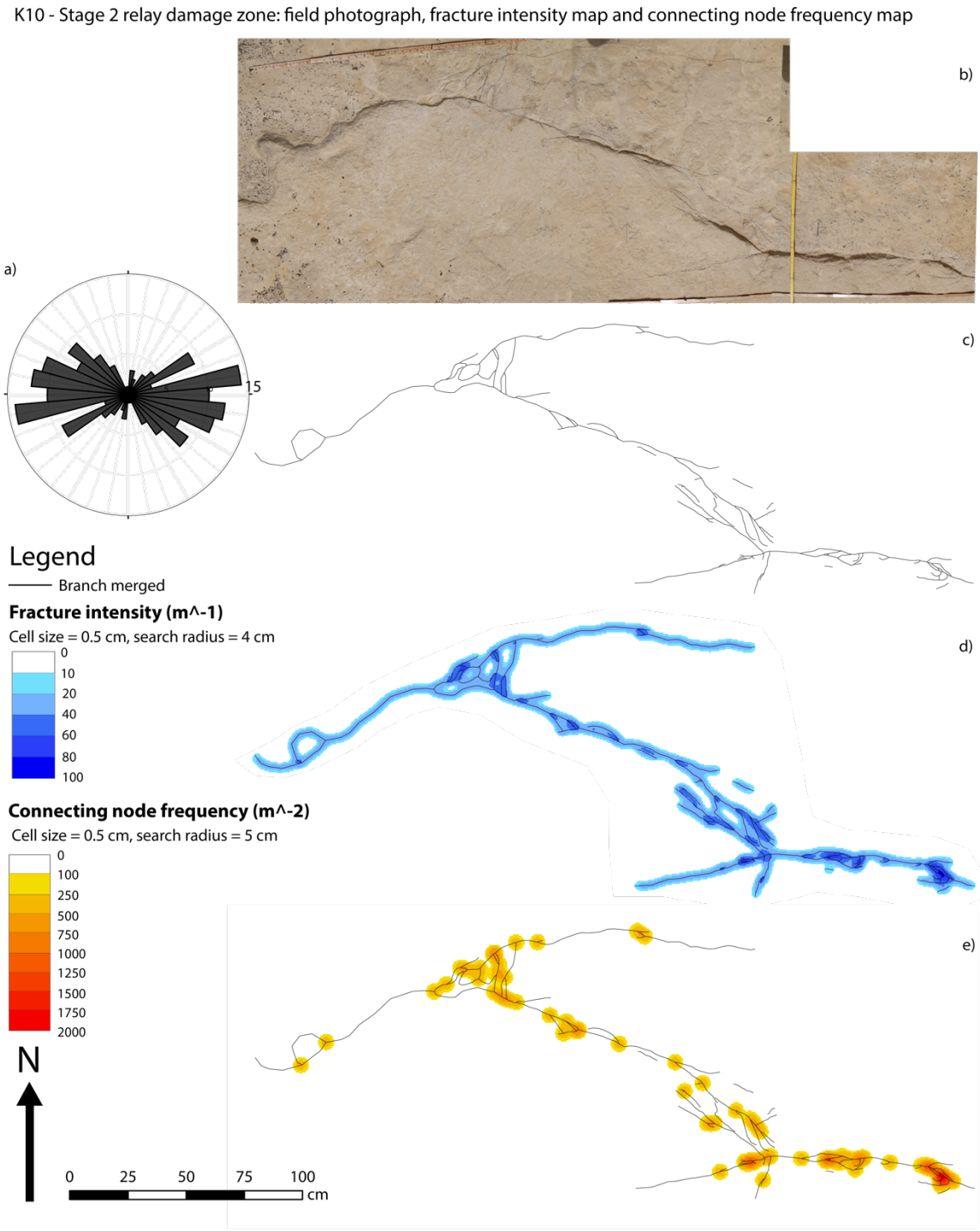

Figure AII.7: a) Rose diagram, including length-weighted strikes of all branches within the locality. b) Field photograph, c) branches, d) fracture intensity map and e) connecting node frequency map of K10. K10 is a stage 2 relay damage zone exposed in the MGLM.

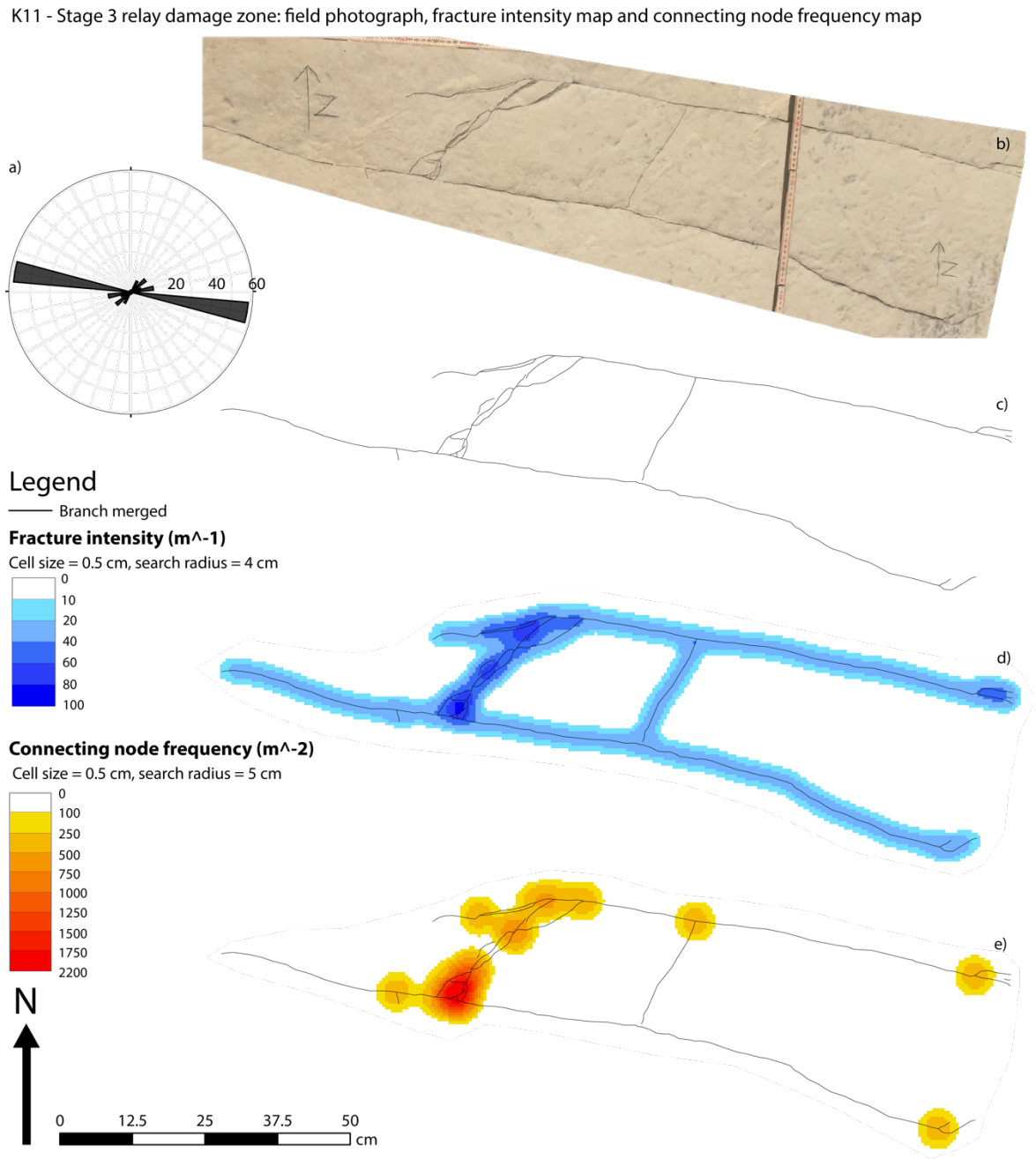

Figure AII.8: a) Rose diagram, including length-weighted strikes of all branches within the locality. b) Field photograph, c) branches, d) fracture intensity map and e) connecting node frequency map of K11. K11 is a stage 3 relay damage zone exposed in the MGLM.

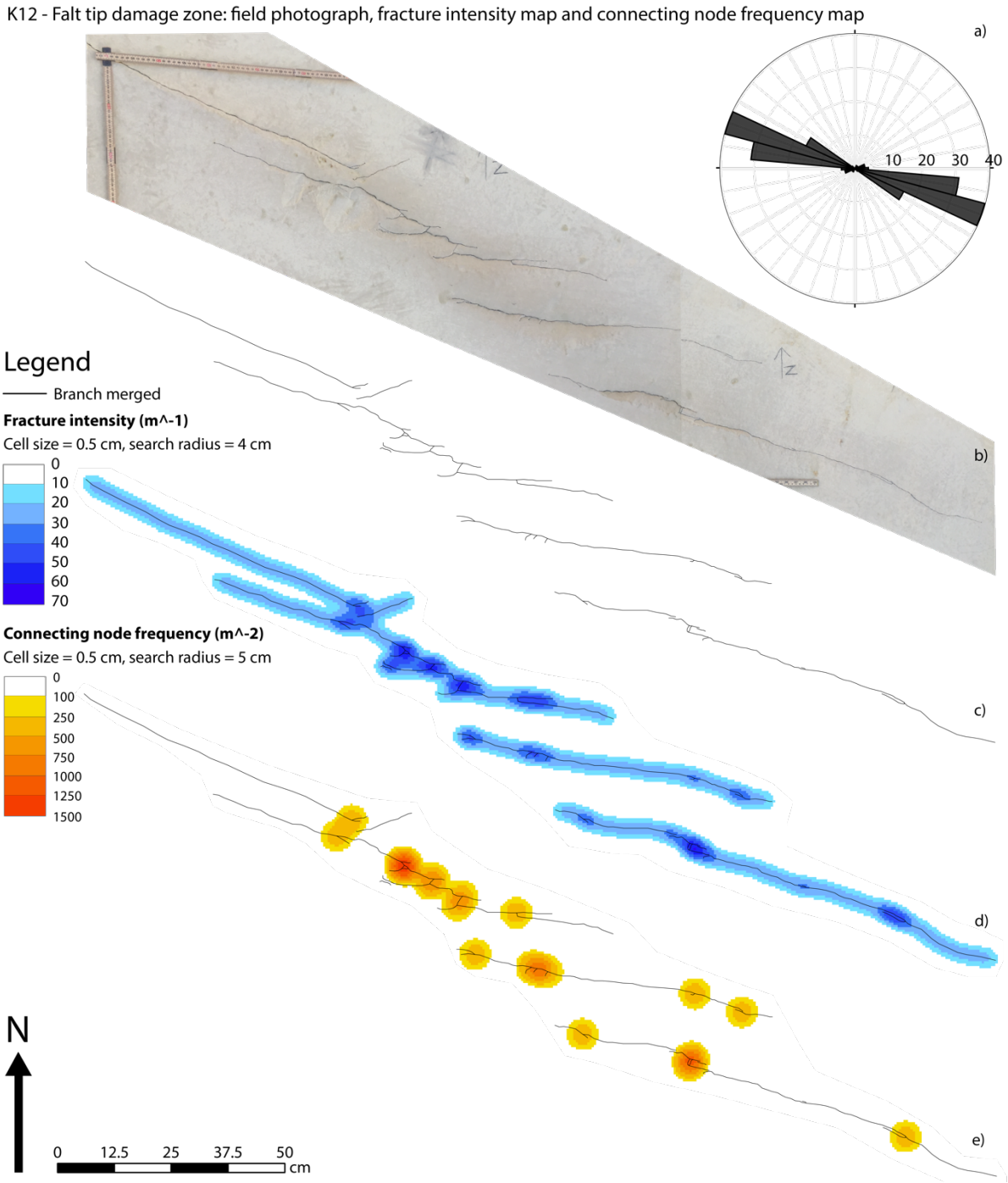

Figure AII.9: a) Rose diagram, including length-weighted strikes of all branches within the locality. b) Field photograph, c) branches, d) fracture intensity map and e) connecting node frequency map of K12. K12 is a normal fault tip damage zone exposed in the MGLM.

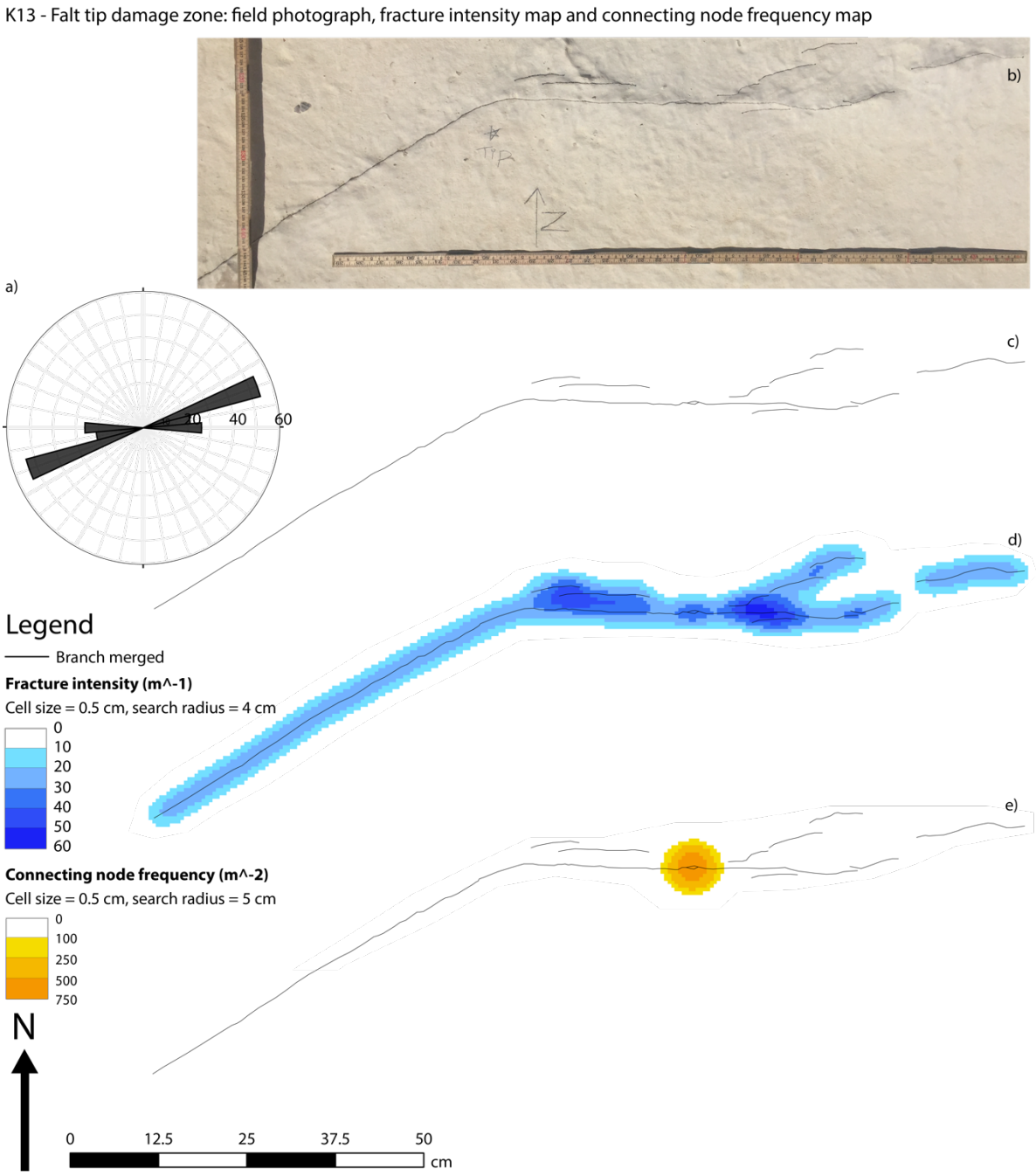

Figure AII.10: a) Rose diagram, including length-weighted strikes of all branches within the locality. b) Field photograph, c) branches, d) fracture intensity map and e) connecting node frequency map of K13. K13 is a normal fault tip damage zone exposed in the MGLM.

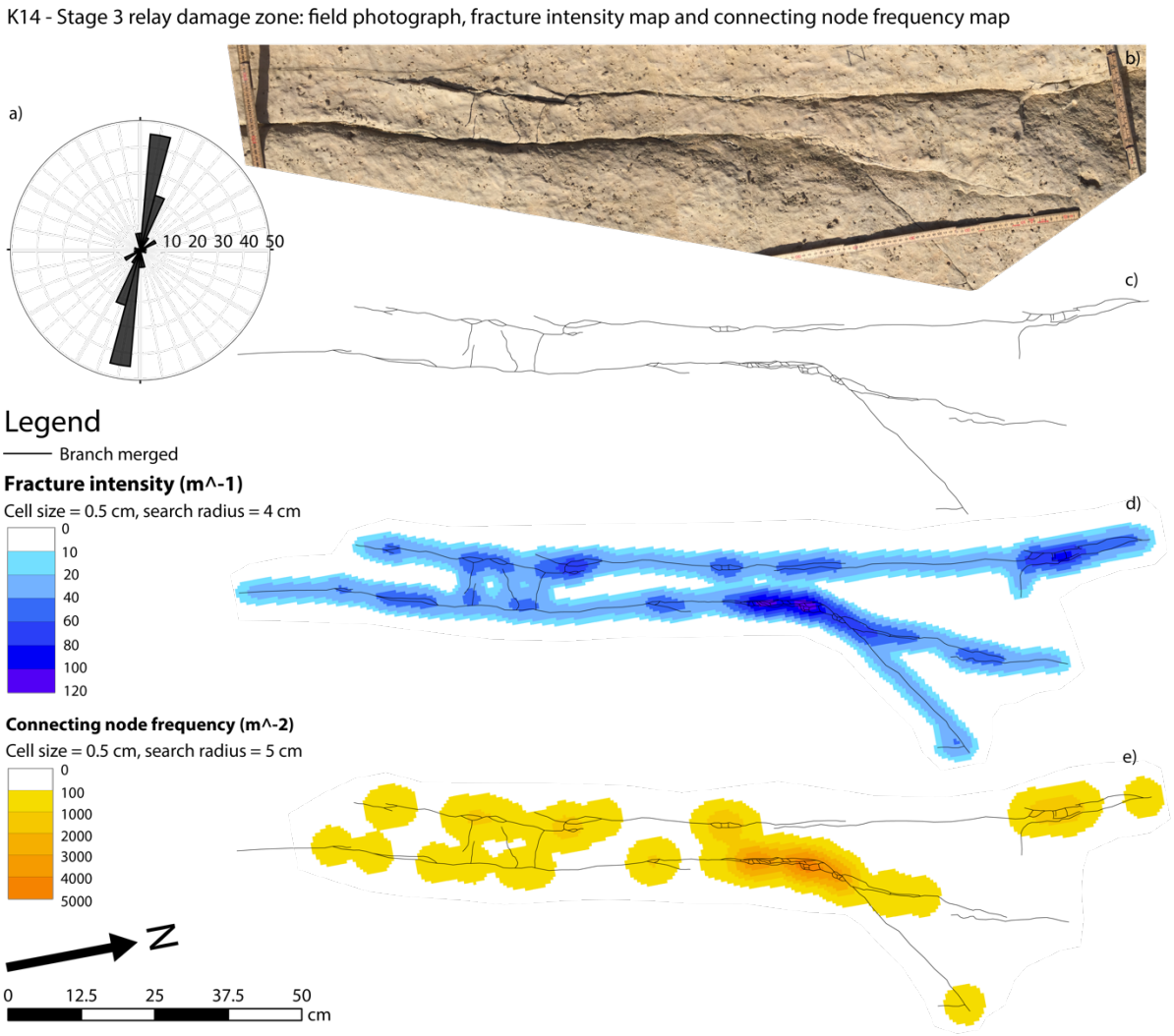

Figure AII.11: a) Rose diagram, including length-weighted strikes of all branches within the locality. b) Field photograph, c) branches, d) fracture intensity map and e) connecting node frequency map of K14. K14 is a stage 3 relay damage zone exposed in the MGLM.

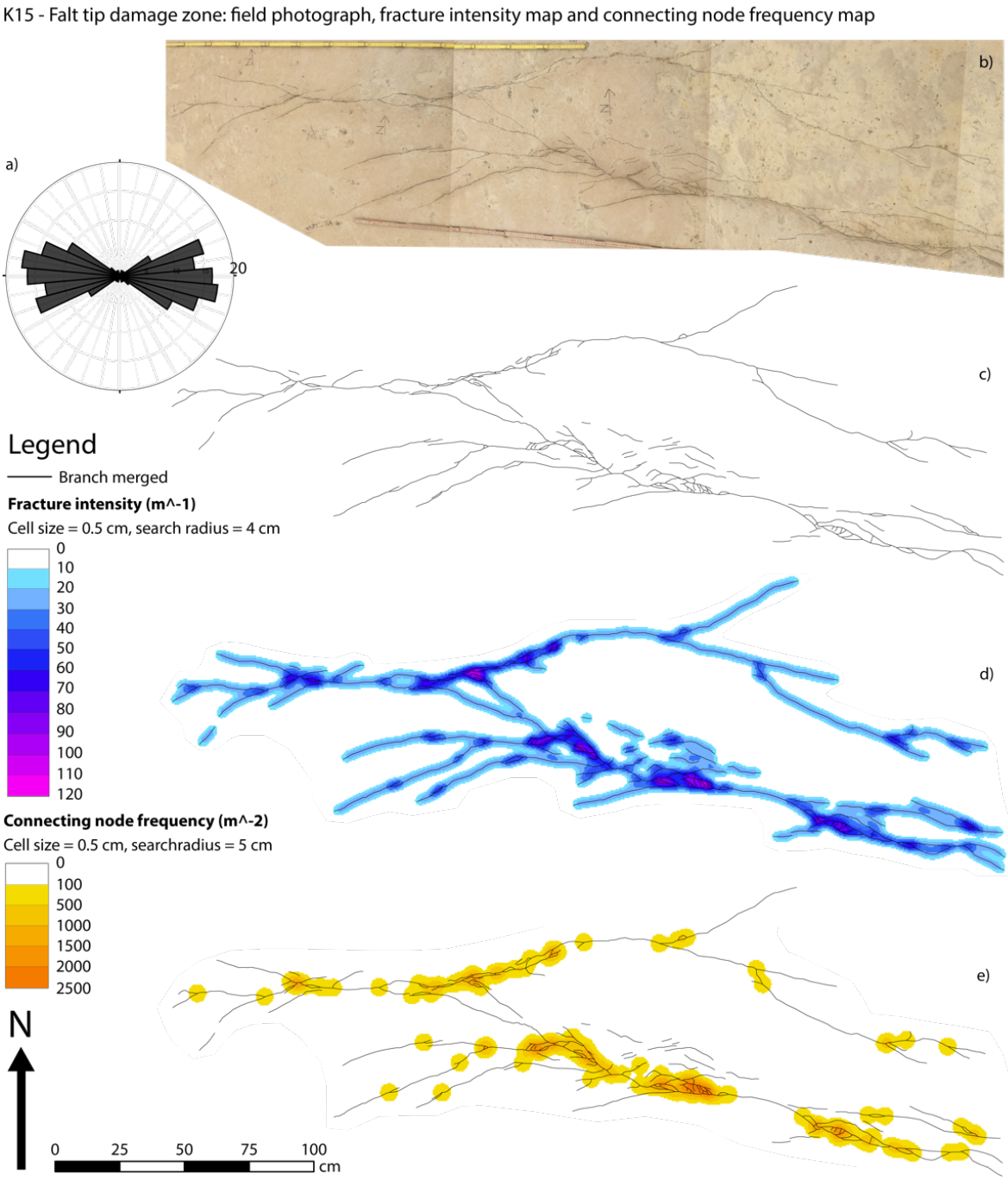

Figure AII.12: a) Rose diagram, including length-weighted strikes of all branches within the locality. b) Field photograph, c) branches, d) fracture intensity map and e) connecting node frequency map of K15. K15 is a normal fault tip damage zone exposed in the MGLM.

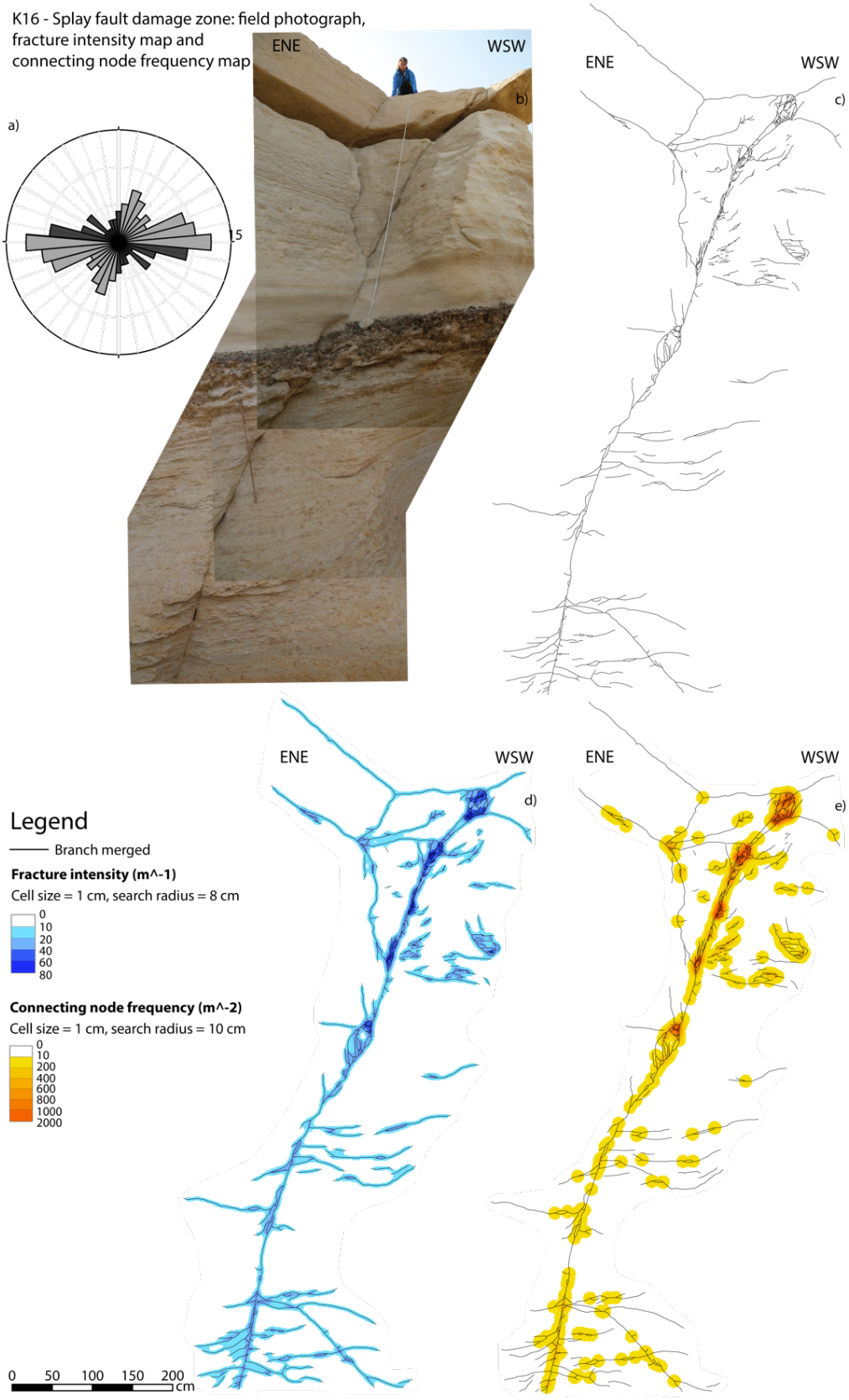

Figure AII.13: a) Rose diagram, including length-weighted dips of all branches within the locality. b) Field photograph, c) branches, d) fracture intensity map and e) connecting node frequency map of K16. K16 is a normal fault splay damage zone exposed in LGLM and MGLM.

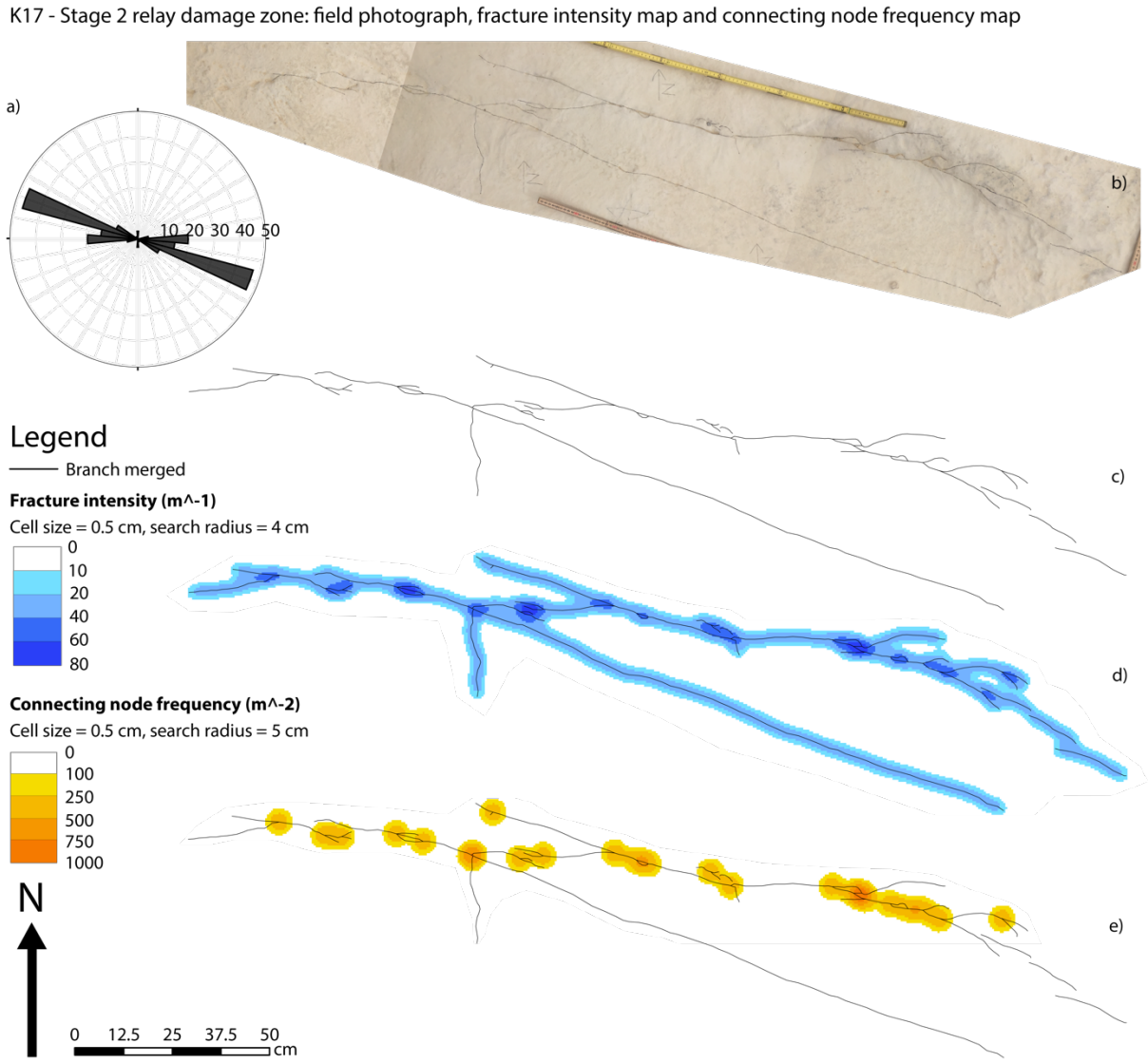

Figure AII.14: a) Rose diagram, including length-weighted strikes of all branches within the locality. b) Field photograph, c) branches, d) fracture intensity map and e) connecting node frequency map of K17. K17 is a stage 2 relay damage zone exposed in the MGLM.

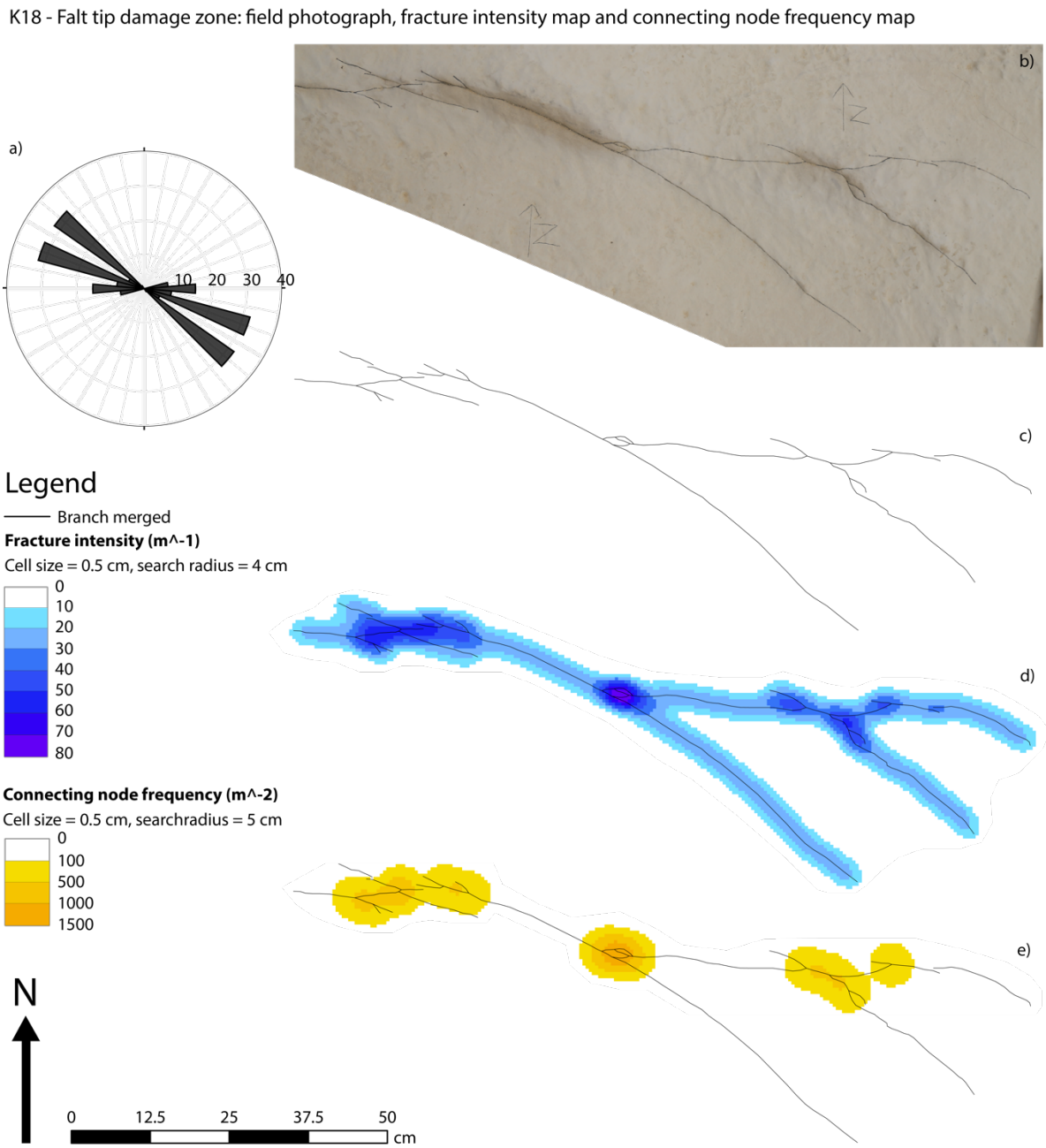

Figure AII.15: a) Rose diagram, including length-weighted strikes of all branches within the locality. b) Field photograph, c) branches, d) fracture intensity map and e) connecting node frequency map of K18. K18 is normal fault tip damage zone exposed in the MGLM.

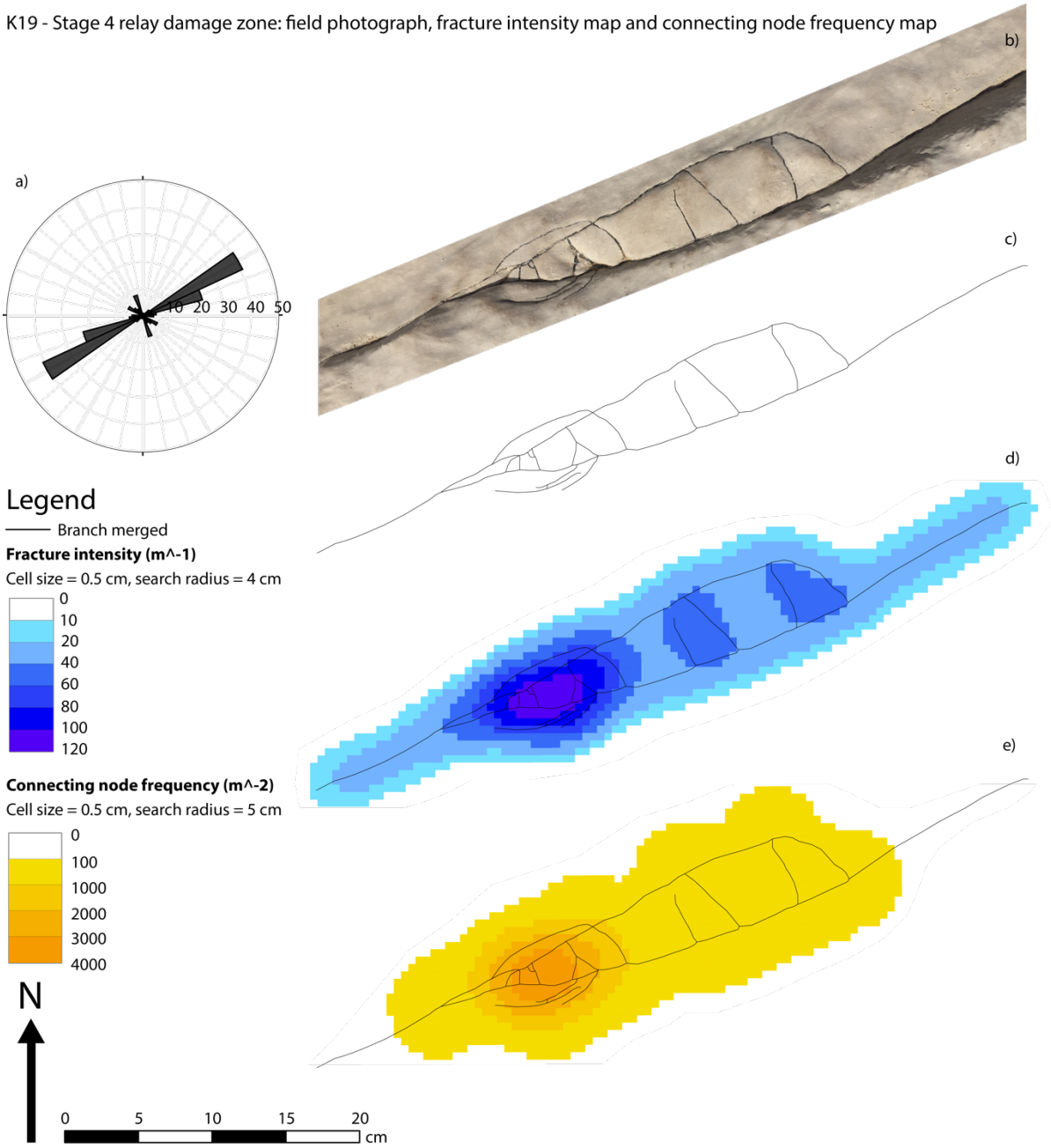

Figure AII.16: a) Rose diagram, including length-weighted strikes of all branches within the locality. b) Field photograph, c) branches, d) fracture intensity map and e) connecting node frequency map of K19. K19 is a stage 4 relay damage zone exposed in the MGLM.

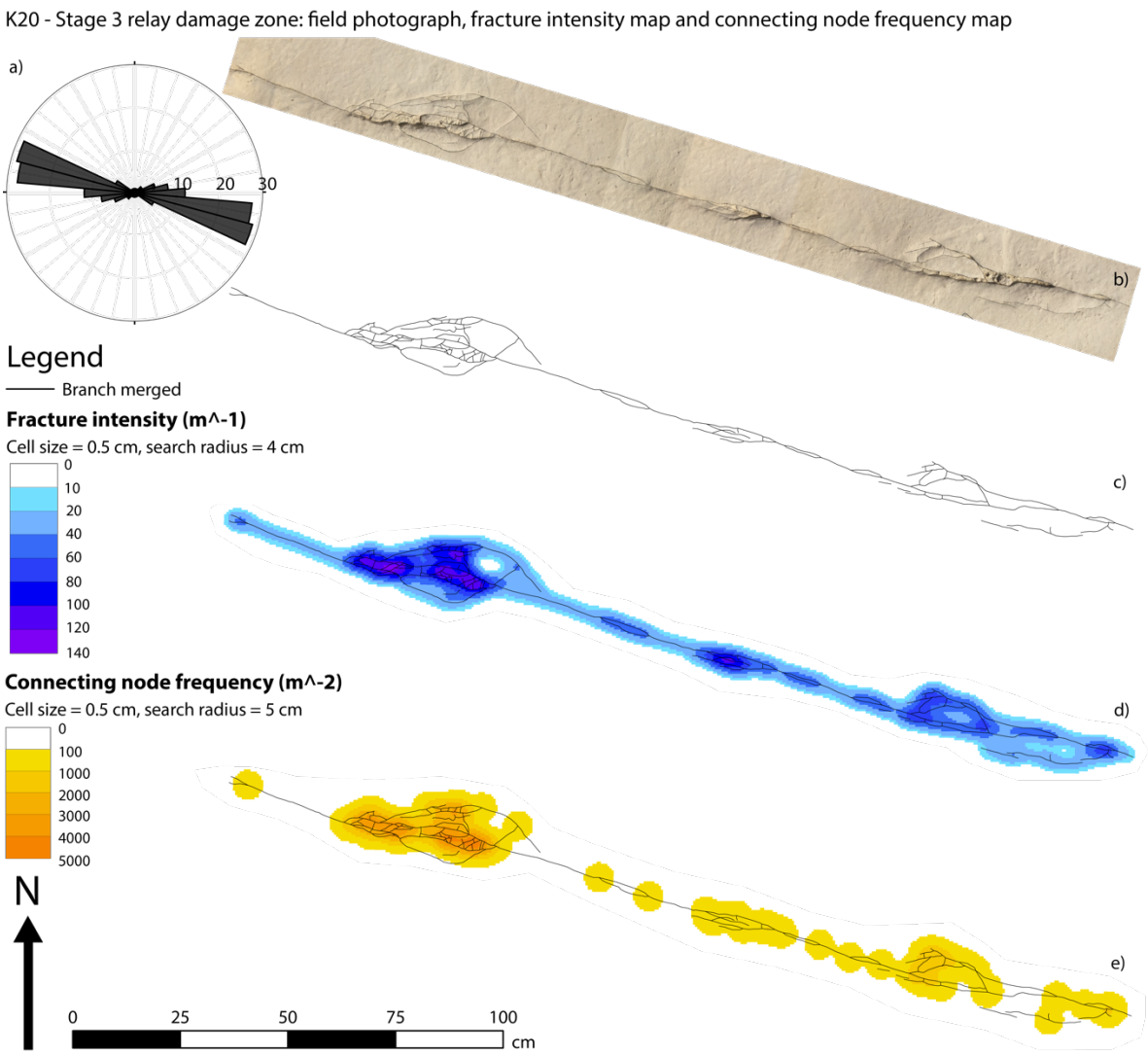

Figure AII.17: a) Rose diagram, including length-weighted strikes of all branches within the locality. b) Field photograph, c) branches, d) fracture intensity map and e) connecting node frequency map of K20. K20 is a stage 3 relay damage zone exposed in the MGLM.

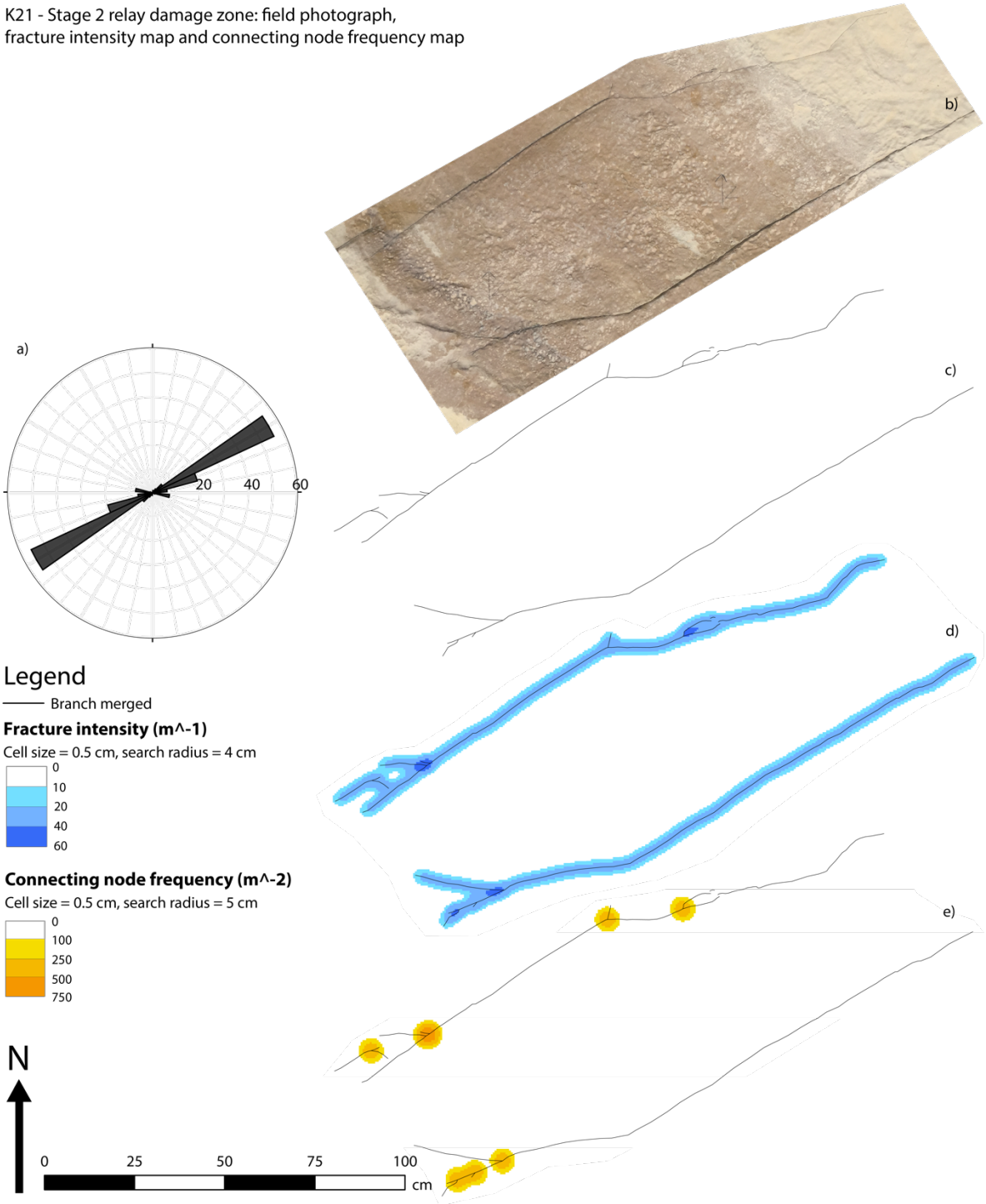

Figure AII.18: a) Rose diagram, including length-weighted strikes of all branches within the locality. b) Field photograph, c) branches, d) fracture intensity map and e) connecting node frequency map of K21. K21 is a stage 2 relay damage zone exposed in the MGLM.

Fold out figure 1: **See the next A3 figure**: Fracture intensity map of all documented damage zones. a-f) Fault tip damage zones, g-i) the splay fault damage zones. j-r) Relay damage zones are arranged from high percentages of I-node to low percentages of I-nodes. s) The topology of each locality is shown in the triangular node plot, reflecting the proportions of I-, Y- and X-nodes and indicated connectivity.

Fold out figure 2: See the last A3 figure: Connecting node frequency map of all documented damage zones, arranged from high proportions of I-node to low proportions of I-nodes. a-f) Fault tip damage zones. g-i) Splay fault damage zones. j-r) Relay damage zones. s) The topology of each locality is shown in the triangular node plot, reflecting the percentages of I-, Y- and X-nodes and indicated connectivity

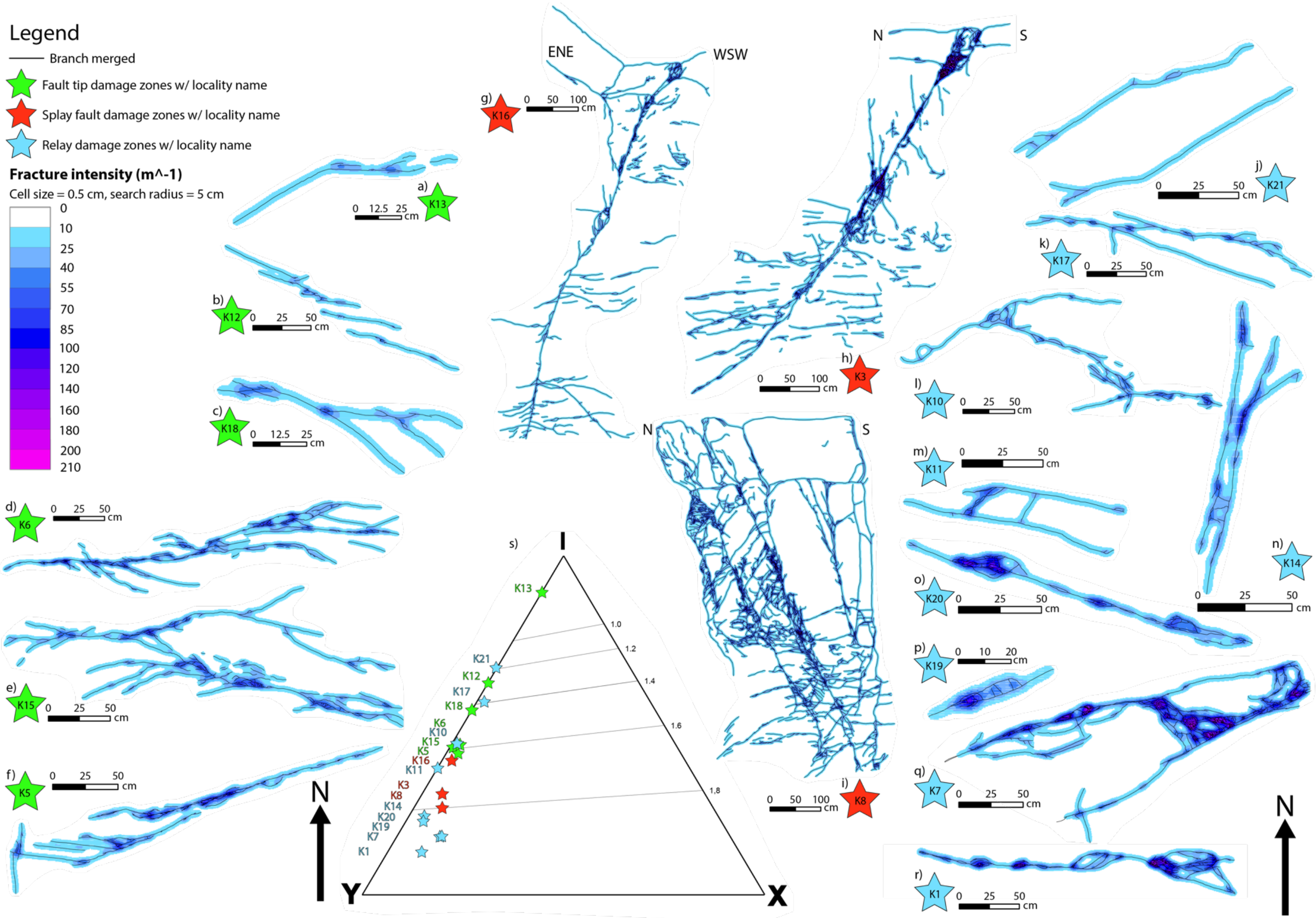
Legend
Branch merged
Fault tip damage zones w/ locality name
Splay fault damage zones w/ locality name
Relay damage zones w/ locality name
Fracture intensity (m^-1)
Cell size = 0.5 cm, search radius = 5 cm
0
10
25
40
55
70
85
100
120
140
160
180
200
210
a) K13 0 12.5 25 cm
b) K12 0 25 50 cm
c) K18 0 12.5 25 cm
d) K6 0 25 50 cm
e) K15 0 25 50 cm
f) K5 0 25 50 cm
g) K16 0 50 100 cm
ENE
WSW
h) K3 0 50 100 cm
N
S
i) K8 0 50 100 cm
N
S
j) K21 0 25 50 cm
k) K17 0 25 50 cm
l) K10 0 25 50 cm
m) K11 0 25 50 cm
n) K14 0 25 50 cm
o) K20 0 25 50 cm
p) K19 0 10 20 cm
q) K7 0 25 50 cm
r) K1 0 25 50 cm
s)
I
Y
X
1.0
1.2
1.4
1.6
1.8
K13
K21
K12
K17
K18
K6
K10
K15
K5
K16
K11
K3
K8
K14
K20
K19
K7
K1
N
N

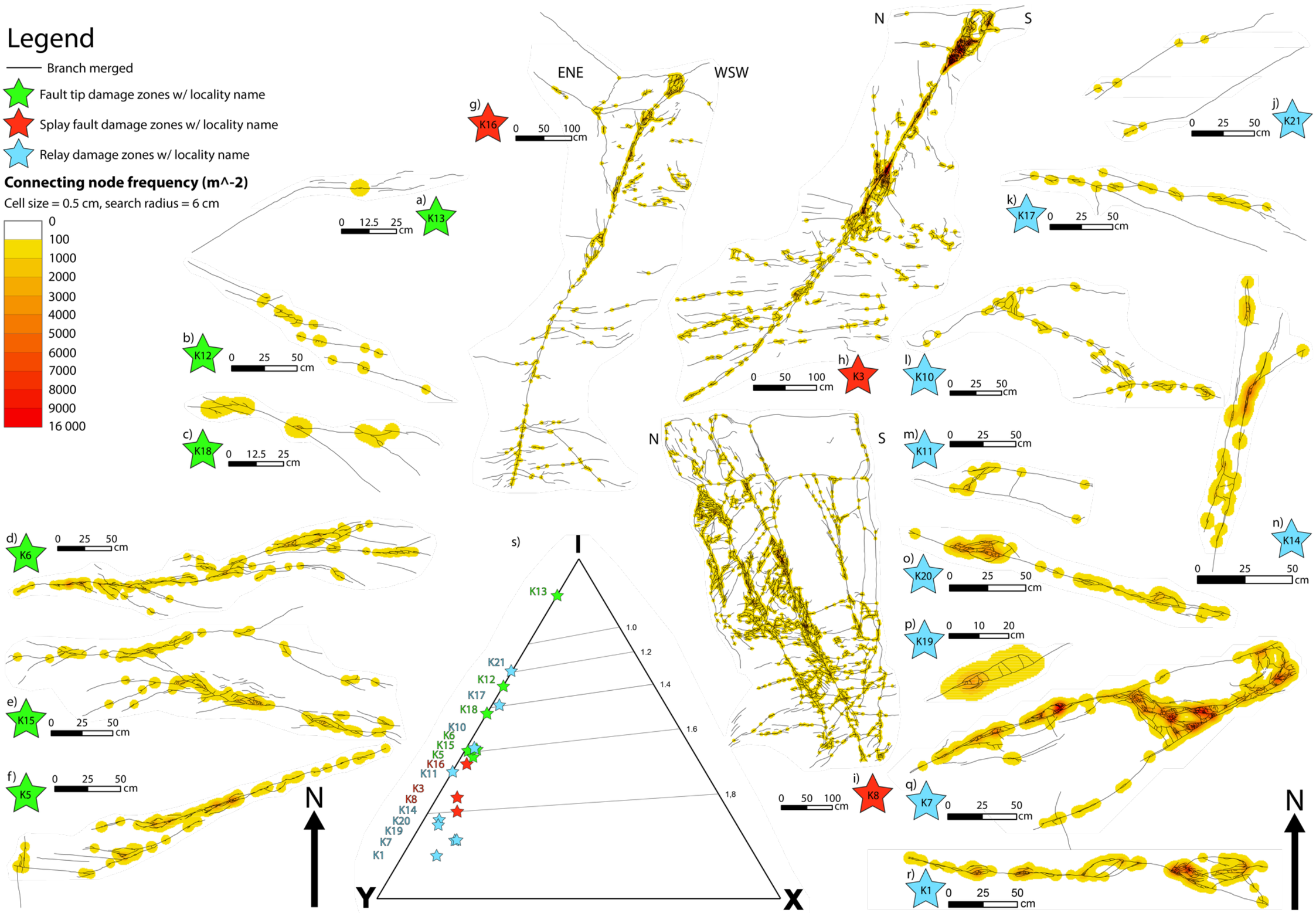
Legend
Branch merged
Fault tip damage zones w/ locality name
Splay fault damage zones w/ locality name
Relay damage zones w/ locality name
Connecting node frequency (m^-2)
Cell size = 0.5 cm, search radius = 6 cm
0
100
1000
2000
3000
4000
5000
6000
7000
8000
9000
16 000
a) K13
b) K12
c) K18
d) K6
e) K15
f) K5
g) K16
h) K3
i) K8
j) K21
k) K17
l) K10
m) K11
n) K14
o) K20
p) K19
q) K7
r) K1
ENE
WSW
N
S
0 12.5 25 cm
0 25 50 cm
0 50 100 cm
0 10 20 cm
s)
K13
K21
K12
K17
K18
K10
K6
K15
K5
K16
K11
K3
K8
K14
K20
K19
K7
K1
1.0
1.2
1.4
1.6
1,8
Y
X